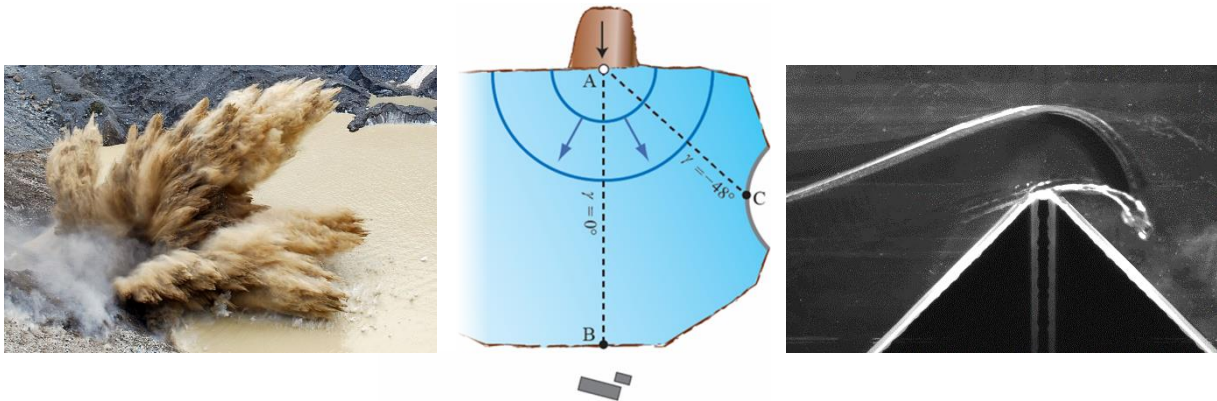




Landslide-generated Impulse Waves in Reservoirs

Basics and Computation



2nd Edition, 2019



Version history	Notes
V 1.0 (February 2009)	First edition
V 2.0 (November 2019)	Second edition (revised and updated)
V 2.1 (June 2023)	Second edition incl. addendum on shallow impact angles

Imprint

Date:

12. June 2023

Commissioning institution:

Swiss Federal Office of Energy SFOE, CH-3003 Bern, Switzerland

Research institution:

Laboratory of Hydraulics, Hydrology and Glaciology VAW, ETH Zurich, 8093 Zurich

Authors:

Dr. Frederic M. Evers
Asst. Prof. Dr. Valentin Heller
Dr. Helge Fuchs
Em. Prof. Dr. Willi H. Hager
Prof. Dr. Robert M. Boes

SFOE project coordinators:

Dr. Philipp Oberender
Dr. Georges R. Darbre

Cover images:

Left: Rock avalanche impact at Lower Grindelwald Glacier Lake, May 22, 2009 (H. & M. Burgener)
Centre: Top view of a generalised 3D impulse wave event.
Right: Impulse wave overtopping experiment in the hydraulic laboratory at VAW.

This study was performed for the Swiss Federal Office of Energy within the scope of the Dam Research Program. The author(s) of the study is/are responsible for its content.

Preface (2nd edition)

Ten years have passed since the first edition of ‘Landslide-generated Impulse Waves in Reservoirs – Basics and Computation’ was published. During this period, this so-called *impulse wave manual* has been widely applied by dam operators, engineering companies, dam safety agencies and research institutes around the world. In addition to an improved emergency planning for existing reservoirs, the manual’s computational procedure proved to be an inexpensive method to obtain a first indication of an impulse wave event’s magnitude during the preliminary design phase of new reservoir projects. If a potential impulse wave risk is identified at an early stage of the design process, more extensive and prototype-specific methods including physical hydraulic modelling and numerical simulations can be conducted to develop mitigation measures. Moreover, in imminent emergency situations, the complementary spreadsheet-based computational tool allowed for ad-hoc wave height and run-up estimations in quasi no time.

Besides the presentation of a coherent computational procedure, one of the first edition’s main objectives was to provide practitioners with an overview of the state-of-the-art in impulse wave research. As a result, also research gaps existing at that time had been identified. In combination with the authors’ own experiences in applying the manual for hazard assessment studies, these gaps led to the initiation of further research efforts. The main results of these studies have been included in the present new edition. Revised and new topics include, amongst others: slide velocity estimation, 3D impulse wave generation and propagation, overland flow, water body geometries between 2D and 3D and edge waves. Furthermore, additional examples were included and the computational tool has been revised.

The Dam Safety Section of the Swiss Federal Office of Energy SFOE, which commissioned this work, is acknowledged for co-funding the preparation of this second edition. Especially the continuous interest and support of Dr. Georges R. Darbre for putting impulse wave research into practice is to be emphasised.

Zurich, November 2019

Frederic M. Evers, Valentin Heller, Helge Fuchs,
Willi H. Hager and Robert M. Boes

Preface (1st edition)

Impulse waves generated in natural lakes and reservoirs by the impact of landslides may cause damages during run-up shores or against dams. Particular attention has, in this context, to be given to dams and in particular to embankments dams which, if overtopped, may suffer serious damages or even fail completely. It is, therefore, of great importance that the size of such waves and their run-up height on the shore or dam face are known.

Over the past thirty years the VAW has carried out a number of research projects on impulse waves, and this manual presents the results of this research together with available international literature on the topic. In addition, it gives an explanation of a computation procedure that enables forecast values for all relevant parameters to be determined. This makes possible emergency planning and allows preventive action, for instance precautionary lowering of the lake or reservoir, to be taken in good time.

The objective of this manual is to make the research results available to practising engineers in appropriate form. The results of these computations may still result in estimations to certain extent so it is necessary, as so often in engineering design, to include safety factors in the computations. In many cases the possible errors are so large that a hydraulic model test or a numerical simulation has to be resorted to. Nonetheless, the order of magnitude of the characteristics of the impulse waves can be estimated.

We wish to express our thanks to the Dam Safety Section of the Swiss Federal Office of Energy SFOE, which commissioned this work, for all their cooperation, and to Dr. Andreas Huber for his critical comments. Thanks also to Mr. Ian David Clarke for the translation of the German to this English version.

This manual, as well as the spread sheets, are available in electronic form on the VAW-Website www.vaw.ethz.ch under “News & Events”, “Latest VAW Reports”. We hope that this manual finds a wide readership.

Zurich, February 2009

Valentin Heller, Willi H. Hager and Hans-Erwin Minor

Table of contents

Preface.....	I
Table of contents.....	III
Summary	VII
<hr/>	
1 Introduction.....	1
1.1 Overview	1
1.2 Methods for predicting landslide generated impulse waves.....	3
2 Water wave theory.....	11
2.1 Introduction	11
2.2 Theoretical wave types	14
3 Computational procedure and Step 1	17
3.1 Introduction	17
3.2 Wave generation and propagation	19
3.2.1 Introduction	19
3.2.2 Governing parameters.....	20
3.2.3 Slide velocity at the point of impact.....	22
3.2.4 Reservoir shape	26
3.2.4.1 Values independent of 2D or 3D.....	26
3.2.4.2 Extreme case (a) (2D).....	27
3.2.4.3 Extreme case (b) (3D).....	31
3.3 Wave run-up and dam overtopping	35
3.3.1 Introduction	35
3.3.2 Governing parameters.....	35
3.3.3 Wave run-up	36
3.3.4 Wave overtopping at rigid dams.....	37
3.4 Overland flow	39
3.4.1 Introduction	39
3.4.2 Governing parameters.....	39
3.4.3 Overland flow front propagation	41
3.4.4 Overland flow depth	41
3.4.5 Overland flow velocity	42
3.5 Wave force on dams	45
3.5.1 Introduction	45
3.5.2 Hydrostatic pressure	45

3.5.3	Wave run-up and overtopping	47
3.6	Final comments	50
4	Step 2, sensitivity analysis and safety allowance	51
4.1	Introduction	51
4.2	Effects of the reservoir shape	51
4.2.1	Water body geometries between 2D and 3D	54
4.2.2	Constriction at dam flanks	59
4.2.3	Ice cover	60
4.3	Edge waves	60
4.4	Mass movement types	64
4.5	Underwater slide deposits	68
4.6	Sensitivity analysis	70
4.7	Safety allowance	72
5	Computational examples	75
5.1	Example 1	75
5.1.1	Problem description and governing parameters	75
5.1.2	Step 1	77
5.1.3	Step 2	90
5.1.4	Conclusions	92
5.2	Example 2	93
5.2.1	Problem description and governing parameters	93
5.2.2	Step 1	95
5.2.3	Step 2	102
5.2.4	Conclusions	103
5.3	Example 3	105
5.4	Example 4	108
5.5	Computational tool	114
5.5.1	Introduction	114
5.5.2	Structure	114
5.5.3	Application	116
5.5.4	Troubleshooting	117
6	Conclusions	119
References		121
Notation		127
Glossary		135

A Wave overtopping at granular dams..... A-1

B Extended bibliography B-1

B.1 Impulse wave generation and propagation B-1

B.2 Wave-shore and wave-structure interaction B-2

Summary

Landslide-generated impulse waves are typically caused by landslides, rockfalls, shore instabilities, snow avalanches or glacier calvings in oceans, bays, lakes or reservoirs. They are particularly relevant for the Alpine environment because of steep valley sides, possible large slide masses and impact velocities and the great number of reservoirs. In this *manual*, a state-of-the-art on the impulse wave generation and its effects on dams are presented including a computational procedure. Based on this method, engineers or natural scientists may predict the hazards originating from impulse waves efficiently and economically. The 1st edition of this manual was published in 2009. This 2nd edition includes both updates of existing and new computational approaches for additional hydraulic processes.

The introduction in Chapter 1 contains background information on the topic and compares the available methods dealing with landslide-generated impulse waves. The method presented in this manual is based on *generally applicable equations* derived from hydraulic model tests. Chapter 2 introduces basic principles of the water wave theory. The computational procedure is presented in Chapter 3 and shown in Figure 3-1. It is based on the findings of impulse wave generation and its effects on dams. The computational procedure (Figure 3-1) includes two steps: in *Step 1* the generally applicable equations are applied according to Chapter 3, whereas in *Step 2* the effects not contained in Step 1 such as the effective instead of the idealised reservoir geometry are considered according to Chapter 4.

In Step 1, the mass movement is modelled as a granular slide. To analyse the effect of impulse waves on dams, the wave height, amplitude, period and length are important. These are computed with the equations of Heller and Hager (2010) and Evers *et al.* (2019) as a function of the slide parameters. Two extreme cases for estimating the wave parameters are considered: (a) laterally constricted (2D) and (b) free radial propagation of the impulse waves (3D). The wave generation in both (a) and (b) depend on the identical parameters, whereas these for the wave propagation are not identical. Once the necessary wave parameters in front of the dam are determined, the *run-up height* and the *overtopping volume* may be computed according to Evers and Boes (2019) and Kobel *et al.* (2017), respectively. Potential overland flow on horizontal shorelines is covered by the equations of Fuchs and Hager (2015). The *force effects* on dams are computed using the method of Ramsden (1996). This method is first applied as if the dam would be vertical since the horizontal force component is independent from the dam inclination. The additional vertical force component for inclined dams is then computed assuming static wave pressure. If an impulse wave partially overtops a dam, only a partial water pressure has to be considered resulting in a reduction method.

Once the results from Step 1 are available, the effects of the geometrical differences to the idealised extreme cases (a) and (b) have to be quantified in Step 2 according to Chapter 4. These differences may result from the prototype reservoir geometry differing

from the idealised 2D or 3D geometries, or by the non-granular mass characteristics. The impulse wave parameters may considerably differ due to these effects. The present method of Ruffini *et al.* (2019) allows for impulse wave height estimation in intermediate reservoir geometries between 2D and 3D. Approaches for the assessment of edge wave propagation along the shoreline perpendicular to the slide impact direction include equations of Heller and Spinneken (2015) and McFall and Fritz (2017). Moreover, the extent of underwater landslide deposits is covered by the equations of Fuchs *et al.* (2013). Step 2 is also required if the computational tool is applied, because these include only the generally applicable equations from Step 1. Finally, Sections 4.6 and 4.7 contain a sensitivity analysis and some reservoir safety aspects.

Chapter 5 includes four computation examples and the application instructions for the computational tool. In Chapter 6 the conclusions are presented.

Although the computational results, such as the run-up height, seem to be exact, it should be kept in mind that the present method results in estimations. Safety allowances for all planned actions have to be considered. Predictions that are more exact may emerge from a prototype-specific model test or numerical simulations.

1 Introduction

1.1 Overview

Impulse waves typically occur in open oceans, bays, lakes and reservoirs as the result of landslides, rockfalls, shore instabilities, avalanches or glacier calvings. They are classed as gravity waves and can, in extreme cases, result in the overtopping of dams, with catastrophic consequences. Alpine regions face a high risk of such events in view of their steep valley flanks, their potentially large slide volumes, with high impact velocities, and their large number of reservoirs (Heller 2007).

One extreme event was the Vaiont reservoir catastrophe which occurred in 1963. After the reservoir had been impounded for the first time behind the 261.60 m high double-curved arch dam, the left valley flank became unstable. About 300 million m³ of earth and rock, twice the active reservoir capacity, slid into the reservoir. Displaced reservoir water overtopped the dam crest, to a depth of at least 70 m, and swept through the village of Longarone. About 2,000 people lost their lives. The dam itself withstood this extreme event with almost no damage (Schnitter 1964).

Impulse waves have also occurred in Switzerland or, as a precaution, have been analysed numerically or investigated in hydraulic models. Examples are Walensee (Huber 1975) and Urnersee (Müller and Schurter 1993). Huber (1982) summarised about fifty documented events in Switzerland over the past 600 years. On 20 June 2007, a rockfall into Lake Lucerne, near Obermatt, created an impulse wave, which caused slight damage when it flowed up into the village of Weggis, on the opposite shore of the lake (Fuchs and Boes 2010).

Schuster and Wiczorek (2002) presented several possible causes of mass movements. In addition to classic scenarios such as earthquake and intense rainfall, they described 46 cases of slides which followed rapid changes in the water level of reservoirs, for instance during first impounding. Only in rare cases has it been possible to arrest the mass movement; one example is Clyde reservoir in New Zealand (MacFarlane and Jenks 1996). In most cases only passive measures to minimise damage are possible and include evacuation of the population, reservoir drawdown, controlled blasting and, when designing the dam, provision of adequate freeboard. For early risk assessment of a threatening slide, empirical equations can help to determine the potential danger.

Generally applicable equations are quickly and easily used in practice. They can provide an initial estimate of the most important wave properties, such as wave height and run-up height at the dam, and this information on the effects of the impulse waves can help when taking decisions on any further preventive measures which may be needed. However, such equations provide only a first estimate, of the wave height for instance, as they largely neglect the geometry of the reservoir (Section 4.2). But impulse waves may be greatly affected by water depth variations or by the shape of the reservoir

basin. More extensive methods are available for more precise analysis, as discussed in Section 1.2.

The aim of this manual is to formulate a practical computational procedure using the generally applicable equations that are in current use. Computational examples and a computational tool support this procedure.

The equations described in this manual are based principally on granular slide material. The parameters of the mass movement are uniformly referred to as slide, for example slide thickness, although other mass movement types such as fall or topple exist. The mass movement types and their influence on wave parameters are discussed in Section 4.4.

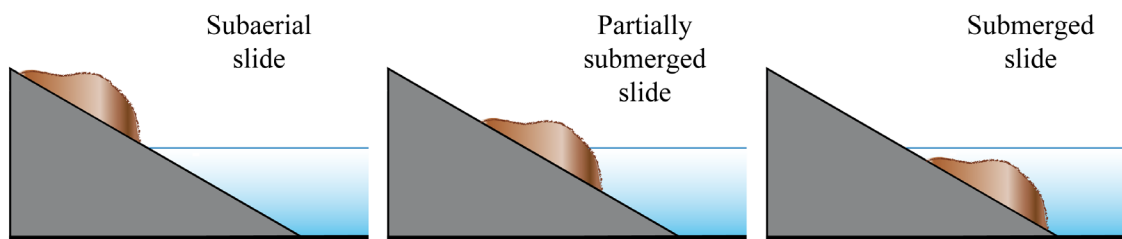


Figure 1-1 Three initial positions of slides before impulse wave generation.

Figure 1-1 shows three initial slide positions before impulse wave generation. Slides can be activated subaerial, partially submerged or fully submerged. In this manual, only slide masses located above the water level are considered, as these represent most cases encountered in Switzerland. Slides activated partially or fully submerged are less common in Switzerland and, as most develop unnoticed, no time is available for their observation or predictive analysis.

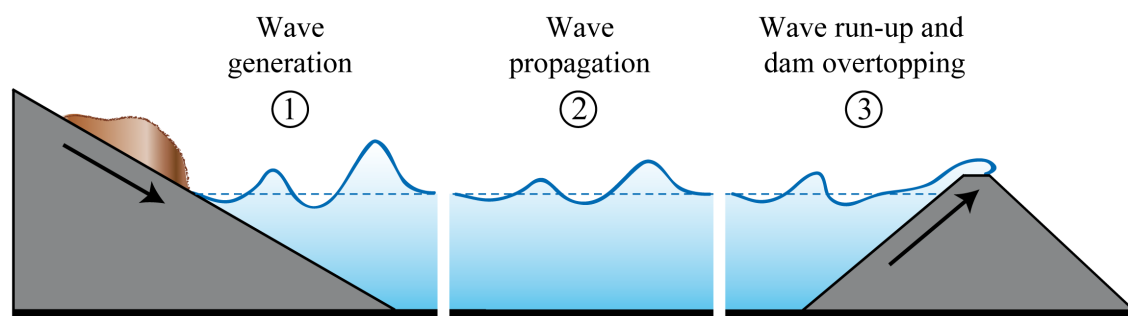


Figure 1-2 The three phases of an impulse wave above a horizontal reservoir bed: (1) slide impact with wave generation, (2) wave propagation with wave transformation and (3) impact and run-up of the impulse wave with load transfer to the dam and, in some cases, overtopping of the dam (after Heller 2007).

Figure 1-2 shows the three phases of impulse wave development above a horizontal reservoir bed: (1) slide impact with wave generation, (2) wave propagation with wave transformation and (3) impact and run-up of the impulse wave with load transfer to a dam and in some cases overtopping of the dam. In narrow reservoirs, phase (2) may not

occur. The mechanisms of phases (1) and (2) are both covered by the same equations, which are discussed in Section 3.2. Phase (3) is described in Sections 3.3 to 3.5.

1.2 Methods for predicting landslide-generated impulse waves

In this manual, a computational procedure, based on generally applicable equations, is developed for the assessment of landslide-generated impulse waves. Firstly, for a better appraisal of the advantages and disadvantages of this procedure, the available methods relating to landslide-generated impulse waves are discussed. Basically the following five methods exist:

- (i) Generally applicable equations developed from physical model tests
- (ii) Prototype-specific model tests
- (iii) Numerical simulations
- (iv) Empirical equations derived from field data
- (v) Analytical investigations

Table 1-1 Comparison of the five methods for the prediction of landslide-generated impulse waves.

Criterion	Method (i)	Method (ii)	Method (iii)	Method (iv)	Method (v)
Quality of results	Estimation	Exact	Estimation - exact	Rough estimate	Rough estimate
Time requirement	Low	Very high	High - very high	Low	Low
Cost	Low	Very high	High - very high	Low	Low
User	Engineer	Engineer	Expert	Engineer	Engineer
Clarity	Medium	High	Low	Medium	Low
Effort for governing parameters	Medium	High	High	Medium	Medium

Table 1-1 compares the five methods, based on the following criteria: the quality of the results, time requirements, costs, the user of each method, the clarity of the results and the efforts needed to determine the governing parameters required for each procedure. These include the parameters describing the topography of the reservoir and the slide geometry as well as the slide characteristics. Table 1-1 shows that, in general, the more precise the results the greater the time expended and cost. Likewise, the effort needed to determine the governing parameters increases accordingly; this is because more data are needed about the geometry of the reservoir and the slide, as well as about the slide characteristics. As explained in Section 1.2, the two last methods, (iv) and (v), are still not fully developed, and this means that methods (i) to (iii) are the most suitable for use in practice. The quality of the results and the time and cost of numerical simulations depend above all on the equations applied and the simplifications made. Table 1-1 shows *where* the strengths of the generally applicable equations lie: an engineer may make an assessment of, for example, the run-up height R at a dam at little cost and in a short time, and only moderate effort is needed to determine the governing parameters. Particular points relating to each method, not mentioned in Table 1-1, will now be discussed individually and illustrated with examples taken from the technical literature.

- (i) Generally applicable equations developed from physical model tests

Figure 1-3 shows two generally applicable physical model tests in (a) a wave basin and (b) a wave channel. In addition to the points indicated in Table 1-1, the following advantage and disadvantages of this method need to be mentioned:

- + The results aid in deciding whether more precise investigations with a prototype-specific model or numerical simulations are necessary.
- Scale effects in too small models cannot be ignored and model effects (reflection, refraction, diffraction etc.) occur with geometrical variations from the prototype.
- Special cases are often not investigated, since the available equations are limited on simple geometries.

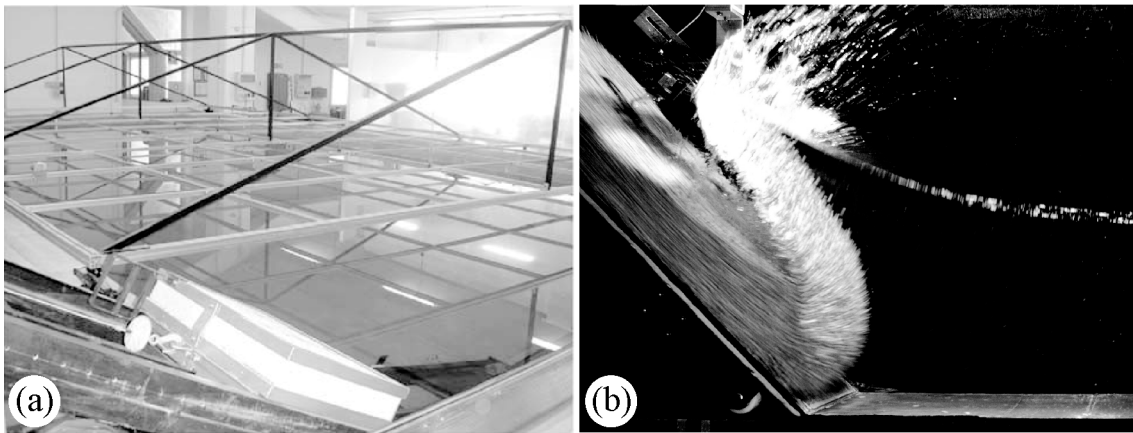


Figure 1-3 Generally applicable model tests: (a) rigid body prior to impact into a wave basin (Panizzo *et al.* 2005) and (b) granular slide material during impact into a wave channel (Heller *et al.* 2008).

This method is often the only possibility when calculations have to be done quickly, for instance when a landslide already shows signs of slow movement. In order to be able to neglect scale effects, the following rules of thumb may be followed: the still water depth in the slide impact zone should be $h \geq 0.200$ m (Heller *et al.* 2008) and in addition the wave period should be $T > 0.35$ s (Hughes 1993), such that the waves (as gravity waves) are dominated by gravity and not by surface tension forces (as capillary waves). For a prototype in which $h = 50$ m, the first rule leads to a minimum scale of 1:250. An associated reservoir surface area of one million m^2 would correspond to a modelled area of $1,000,000/250^2 = 16$ m^2 . More precise data on scale effects related to impulse waves were defined by Heller *et al.* (2008). Model effects, i.e. effects arising mainly from differences between the geometry of the reservoir basin to the model may be taken into account qualitatively by employing the methods described in Sections 4.2 to 4.4.

(ii) Prototype-specific model tests

Prototype-specific model tests were carried out for example by Müller and Schurter (1993) for planned rock blasting on Urnersee, as shown in Figure 1-4(a), as well as by the Western Canada Hydraulic Laboratories (WCHL 1970) for a potential slide above Mica reservoir as shown in Figure 1-4(b). In addition to the points shown in Table 1-1, the following disadvantages of this method should be noted:

- Scale effects cannot be neglected in too small models.
- Model effects may occur with geometric simplifications.

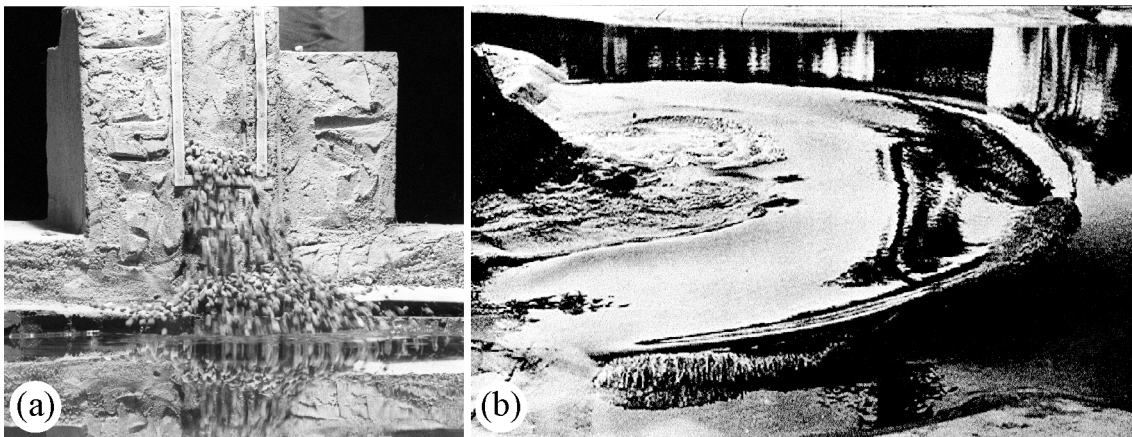


Figure 1-4 Prototype-specific model tests: (a) for planned rock blasting on Urnersee (Müller and Schurter 1993) and (b) for Mica reservoir (Western Canada Hydraulic Laboratories 1970).

To allow scale effects to be neglected, the same rules of thumb apply as for method (i): $h \geq 0.200$ m in the impact zone and $T > 0.35$ s. For a prototype with $h = 50$ m, the first of these criteria gives a minimum scale of 1:250, which means that the corresponding reservoir area of 1,000,000 m², according to (i), will be represented by 16 m² in the model. Therefore, it is often impossible to model the entire reservoir with negligible scale effects, because of space limitations and the corresponding cost. An alternative method is to model only the impact zone and the wave run-up zone and then attempt to estimate the wave transformation between them. Knowledge of the reservoir geometry is essential for the precise determination of the wave characteristics, especially when shallow-water or intermediate-water waves are expected. This is because waves of these types are affected by the reservoir bed (Section 2.1). For deep-water waves, which are not affected by the reservoir bed, the reservoir geometry must be known above all in the slide impact and wave run-up zones.

(iii) Numerical simulations

A comprehensive review about numerical modelling of landslide-generated impulse waves has been presented by Yavari-Ramshe and Ataie-Ashtiani (2016). The landslide is commonly modelled rigid or as a deformable mass with different rheologies. Discrete Element Method modelling is now also possible where each individual grain and grain interactions in a granular landslide are resolved (Kessler *et al.* 2018). Several numerical approaches are available to predict the generation of landslide-generated impulse waves, involving both open source codes (e.g. DualSPHysics (Heller *et al.* 2016, Vacondio *et al.* 2013), OpenFOAM (Chen *et al.* 2018), THETIS (Abadie *et al.* 2012)) and commercial codes such as ANSYS Fluent or Flow-3D (Gabl *et al.* 2015). These computationally expensive approaches are also suitable for wave propagation and inundation if the water body is sufficiently small. An accurate simulation of the wave propagation and inundation in larger water bodies is commonly based on the multi-layer non-linear shallow-water equations (e.g. SWASH (Ruffini *et al.* 2019)), the Boussinesq equations (e.g. FUNWAVE-TVD (Abadie *et al.* 2012)) or even the full Navier-Stokes equations (e.g. NHWAVE (Ma *et al.* 2012)). Whichever approach is chosen, it needs to be carefully calibrated and validated to avoid misleading predictions.

The most accurate results for large water bodies with reasonable computer resources may be achieved by coupling a more comprehensive (and also more computationally expensive) numerical approach for the violent wave generation process (e.g. Direct Numerical Simulations (Abadie *et al.* 2010), Reynolds Averaged Navier-Stokes Equations (Bascarini 2010), Large Eddy Simulations (Liu *et al.* 2005), Smoothed Particle Hydrodynamics SPH (Tan and Chen 2017, Heller *et al.* 2016, Vacondio *et al.* 2013)) with a less computationally expensive wave propagation and inundation approach (e.g. multi-layer non-linear shallow-water models (Ruffini *et al.* 2019), Boussinesq models (Fuhrman and Madsen 2009), two-phase finite volume approaches (Viroulet *et al.* 2013)). The selected wave propagation and inundation model should be able to model the key physical processes such as wave non-linearity, frequency dispersion, diffraction, refraction, shoaling and wave breaking (Gylfadóttir *et al.* 2017, Harbitz *et al.* 2014). Energy dissipation due to bottom friction is generally less relevant, but may still result in non-negligible wave decay for waves close to or in the shallow-water regime. Such coupled approaches have been presented for subaerial landslide-generated impulse waves by Abadie *et al.* (2012) who used the Navier-Stokes model THETIS coupled with the Boussinesq model FUNWAVE-TVD in 3D, Tan *et al.* (2018) where DualSPHysics, based on SPH, was coupled with the multi-layer non-linear shallow-water equation model SWASH in 3D (Figure 1-5) and Viroulet *et al.* (2013) who used SPHysics coupled with Geris, a two-phase finite volume approach, for wave propagation in 2D.

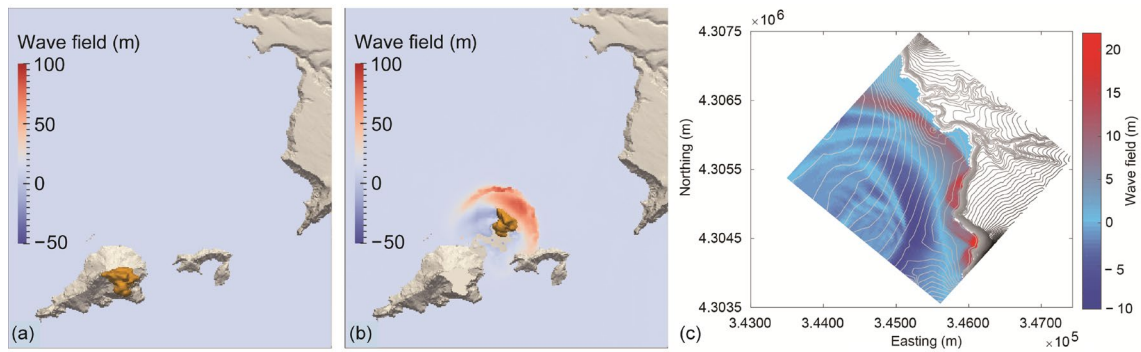


Figure 1-5 Numerical simulation of subaerial landslide-generated impulse waves at Es Vedrà; (a) initial slide position and (b) slide impact with wave propagation modelled with DualSPHysics, based on SPH, and (c) wave propagation and inundation modelled with SWASH (based on the two-layer non-linear shallow-water equations, Tan *et al.* 2018).

For smaller water bodies, one of the computationally expensive wave generation models may be applied for the entire process, and a wave propagation model is not necessary. In the past, the shallow-water equations (Saint-Venant equations) were sometimes applied even for wave generation (e.g. Zweifel *et al.* 2007), given that more complex models were computationally too expensive ten years ago. Whilst the shallow-water equations may sometimes result in acceptable results for engineering applications, they exclude important physical processes (frequency dispersion, accurate vertical velocity distribution) which may result in inaccurate predictions, particularly for larger water bodies. However, models based on the *non-hydrostatic* non-linear shallow water equations, such as SWASH, can consider frequency dispersion and accurately model wave propagation. The increasing computer capacity and the access of Graphics Processing Units GPUs allow nowadays for the simulation of real-world scenarios, including the site-specific topography and bathymetry, within reasonable time scales on a desktop PC equipped with a powerful GPU card. For example, the SPH simulation shown in Figure 1-5 took 80 minutes on a desktop PC equipped with a Titan Xp GPU. Limited computer resources will therefore be a weaker argument to exclude key physical processes in landslide-generated impulse wave simulations in the future, given that the computer power is exponentially growing (Moore’s law).

In addition to the points shown in Table 1-1, the following advantage and disadvantages of this method should be noted:

- + This method can predict subaerial landslide-generated impulse waves well by considering complex site-specific topographic and bathymetric conditions.
- + This method delivers the wave parameters at any desired location and excludes scale effects.
- Calibration and validation of this method is key; for landslide-generated impulse waves this is usually based on hydraulic model tests.

- Some experience on the implementation of the problem and interpretation of the results is required to avoid inaccurate results or misinterpretations.

(iv) Empirical equations derived from field data

Ataie-Ashtiani and Malek Mohammadi (2007) and Oppikofer *et al.* (2016) have derived equations from field data. In addition to the points shown in Table 1-1, the following advantage and disadvantages of this method need to be stated:

- + This method involves no scale effects.
- It is based on field data, which are mostly estimates rather than measurements (for instance wave heights indirectly calculated using run-up heights).
- The governing parameters are also only estimates (for example based on underwater deposits of slide material).
- The equations of Ataie-Ashtiani and Malek Mohammadi (2007) allow only the wave amplitude to be calculated; there is no known work on the determination of other wave parameters.

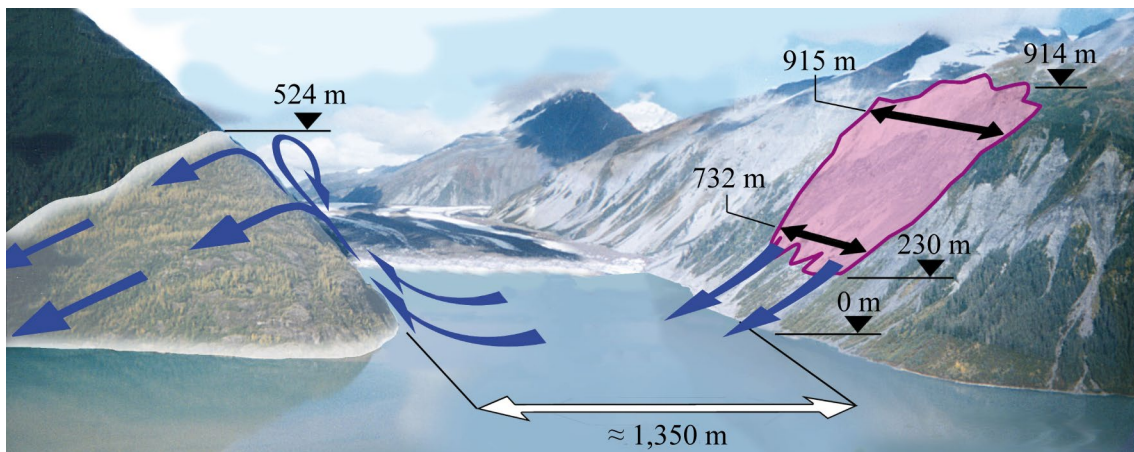


Figure 1-6 Field data: photomontage of the 1958 Lituya Bay case showing the boundaries of the slide area and the maximum wave run-up height of 524 m on the opposite shore of the bay (after Fritz 2002).

The Lituya Bay case of 1958 shown in Figure 1-6 is a rare but fortunate event for researchers because knowing the run-up height on the opposite shore yields information on an impulse wave close to the slide impact location. Only few additional reliable field data exist, including Chehalis Lake 2007 (Roberts *et al.* 2013) and Equip Sermia Glacier 2014 (Lüthi and Vieli 2016). However, for none of these examples actual wave heights were measured during the event. Estimated wave heights are a result of backcalculation from observed run-up heights after the event. As a result, equations derived from field measurements feature a high degree of uncertainty and are hardly valid for general practice.

(v) Analytical investigations

Analytical equations were derived for example by Noda (1970) and Di Risio and Sammarco (2008). A comparison of these two methods with an impulse wave generated in a hydraulic model by a solid mass (Di Risio 2005) is shown in Figure 1-7. In addition to the points shown in Table 1-1, analytical investigations have the following advantage and disadvantages:

- + This method involves no scale effects.
- As the impact mechanism is too complex to be described analytically, predictions for the far field can only be based on simplified initial conditions.
- The deduction of the results can be quite difficult.
- Simplifications are necessary, e.g. using linear-wave theory, potential theory etc., which allows consideration of only relatively small and symmetrical waves.

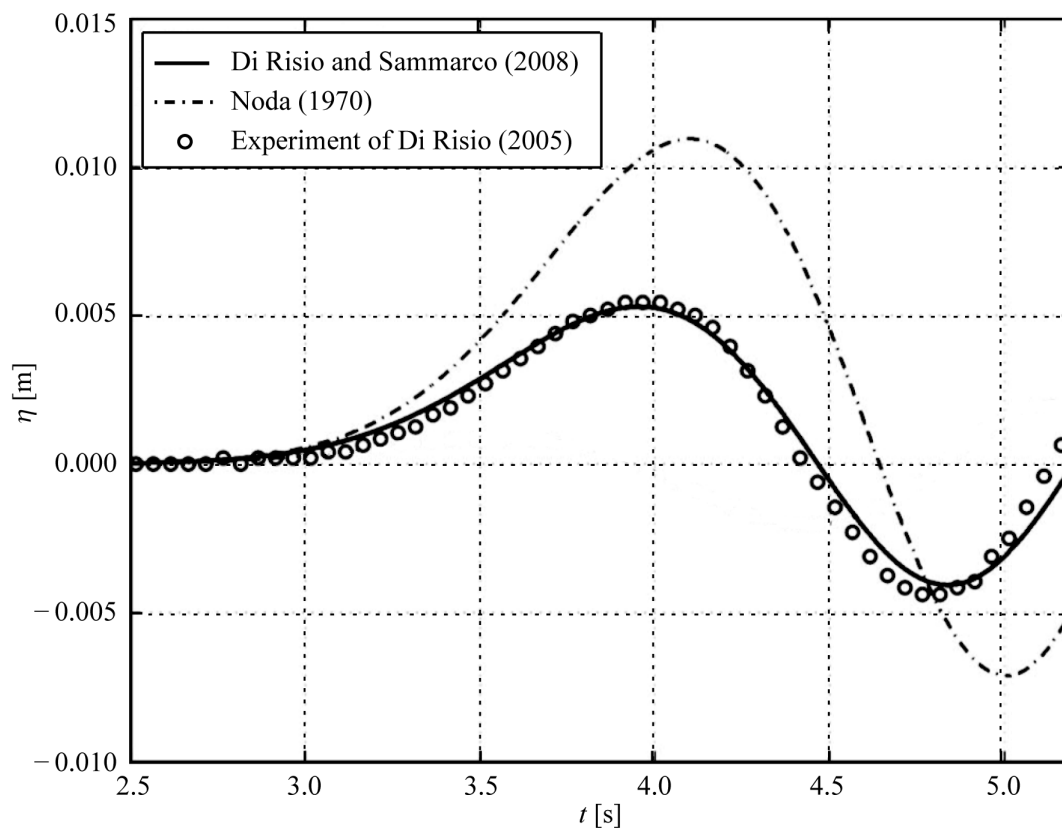


Figure 1-7 Comparison of the analytical computation of a landslide-generated impulse wave profile at a distance $x = 5.30$ m from the impact location with an experiment (Di Risio and Sammarco 2008).

As this method may provide predictions only for very idealised slides and then only in the far field, it is of limited use for practical application.

The first three methods, (i) to (iii), are of practical relevance for the assessment of landslide-generated impulse waves and their effects. Sometimes it may be better to use *hybrid modelling*, i.e. to combine model testing with numerical analysis. This may be done, for example, when the criteria for negligible scale effects in the hydraulic model allow only the investigation of the generation of the waves; the wave propagation will therefore be derived numerically, or if a part of the reservoir is studied using a hydraulic model and the results obtained are then used to calibrate a numerical model. Naturally, the time required and the cost increase by applying a hybrid.

2 Water wave theory

2.1 Introduction

In this chapter the most important properties of water waves are explained. Landslide-generated impulse waves belong to the category of gravity waves, i.e. they are principally influenced by the gravitational force in contrast to capillary waves.

The relevant wave parameters are shown in Figure 2-1 in the (x, z) plane, on a defined *sine wave* whose profile describes a sine curve. If the sine wave is small ($H/h < 0.03$) and flat ($H/L < 0.006$) it is also referred to as a linear wave. The original water depth is defined as the still water depth h . The wave height H is measured from the trough, i.e. from the lowest point on the wave surface to the crest, the highest point. The wave amplitude is the height from the undisturbed water surface to the wave crest. For the sine wave shown in Figure 2-1, $a = H/2$. This no longer applies for impulse waves, which are generally non-linear and vary from the perfect sine wave (Figure 2-1). Furthermore the wave length L extends from wave node to node, crest to crest or trough to trough. The wave period T is the time it takes for the crests, nodes or troughs, respectively, of two successive waves, to pass a fixed point. For the sine wave, the period can be calculated as $T = L/c$, in which c is the wave celerity. The square of the celerity for a linear *sine wave* is given by

$$c^2 = \frac{gL}{2\pi} \tanh\left(\frac{2\pi h}{L}\right). \quad (2.1)$$

c [m/s]	=	Wave celerity (Figure 2-1)
g [m/s ²]	=	Gravitational acceleration; $g = 9.81$ m/s ²
h [m]	=	Still water depth
L [m]	=	Wave length (Figure 2-1)
π [-]	=	Circular constant; $\pi = 3.14$

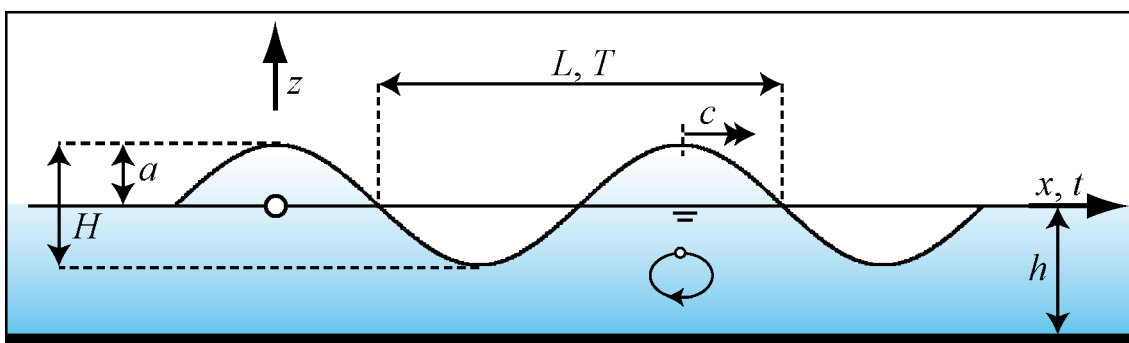


Figure 2-1 Principal wave parameters presented on an idealised sine wave (in addition, the wave is linear if $H/h < 0.03$ and $H/L < 0.006$).

The following terms can be used to differentiate between various water wave types:

- a) Oscillatory or translatory waves
- b) Shallow, intermediate or deep-water waves
- c) Periodic or non-periodic waves
- d) Linear or non-linear waves

- a) Oscillatory or translatory waves

In water waves, the individual particles of water do not move in the same way as the water surface or the wave celerity c . This may be seen in Figure 2-1, where the orbital motion of a water particle is shown for an *oscillatory wave*. Whilst the water surface seems to advance at the wave celerity, the water particle moves elliptically and, over the period considered, remains at the same position. Oscillatory waves do not therefore transport fluid mass, but only energy, which sets the surrounding water particles in motion. *Translatory waves* are the opposite, as the water particles move horizontally in the direction of wave propagation and there is transport of fluid mass as well as energy (Figure 2-5).

- b) Shallow, intermediate or deep-water waves

The criterion for the definition of *shallow*, *intermediate* or *deep-water waves* is the ratio of wave length to still water depth L/h . Figure 2-2 shows, for an oscillatory wave, the water particle movement of these three wave types. Figure 2-2(a) shows a *shallow-water wave*, corresponding to $L/h > 20$, in which the water particles move in elliptical orbits. The orbits become flatter and smaller further down in the water column, until their movement close to the bed is eventually parallel to the bed. A tsunami, caused by tectonic plate movement, is normally a shallow-water wave. Because the ratio L/h for small, sinusoidal shallow-water waves is large, the wave celerity may be calculated using Eq. (2.1) reducing for large L/h to $c = (gh)^{1/2}$.

The opposite case is shown in Figure 2-2(c), a *deep-water wave* commensurate with $L/h < 2$. In this case the water particles move in circular orbits, which decrease further down in the water column until no more movement can be detected on the bed. In other words, deep-water waves are not affected by the lake or sea bed. Wind waves on open water are typically deep-water waves. Applying Eq. (2.1) for a small sinusoidal wave a wave celerity of $c = [gL/(2\pi)]^{1/2}$ is obtained because the ratio L/h is small. Between deep and shallow-water waves is the zone of *intermediate-water waves*, for which $2 < L/h < 20$ (Figure 2-2b). Such waves are partly influenced by the lake or sea bed and their wave celerity may be calculated, for linear waves, using the full expression in Eq. (2.1).

c) Periodic or non-periodic waves

Periodic waves are formed by a group of several waves as shown, for example, in Figure 2-1. A non-periodic wave occurs as a single wave (Figure 2-5).

d) Linear or non-linear waves

The term non-linearity originates from the mathematical definition of waves. Linear waves have the form of a sine curve and their relative height $H/h < 0.03$; in addition, the wave steepness must be $H/L < 0.006$ (Dean and Dalrymple 2004; Figure 2-1). Hence, in the mathematical analysis, the terms H/h and H/L are only considered linearly, with higher order terms being neglected. In contrast, terms of higher order are considered in non-linear wave theories. The greater the degree of non-linearity, the more the wave profile deviates from the ideal sinusoidal profile, i.e. the ratios H/h and/or H/L increase and the linear wave condition for sinusoidal waves $H = 2a$ no longer applies. Normally, the greater the degree of non-linearity, the more complex and time consuming is the mathematical description of the wave profile.

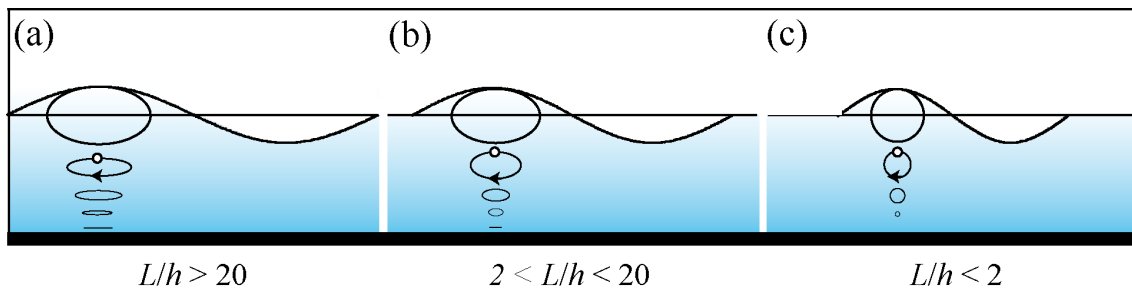


Figure 2-2 Water particle movement of an oscillatory wave in (a) shallow ($L/h > 20$), (b) intermediate ($2 < L/h < 20$) and (c) deep water ($L/h < 2$).

Water waves naturally exhibit a combination of the properties described in a) to d). *Landslide-generated impulse waves* are non-periodic waves and normally strongly non-linear; as a result they are difficult to analyse mathematically. Furthermore, fluid mass transport by such waves may vary from little to considerable and the waves may show both translatory and oscillatory characteristics. Depending on the characteristics of the slide, shallow or deep-water waves may be formed, but mostly intermediate-water waves result. Further, landslide-generated impulse waves commonly consist of several superimposed waves of different lengths travelling at different wave celerity (Eq. 2.1). In other words, an impulse wave consisting of one big wave at the slide impact location typically separates into smaller individual waves far offshore. This process is known as *frequency dispersion*, with the affected waves being called dispersive. In rare cases, an impulse wave train consists of shorter followed by longer waves superimposing further offshore to larger impulse waves because the faster longer waves overtake the slower shorter ones. This mixture of wave characteristics of landslide-generated waves as well as frequency dispersion are reasons why their accurate prediction is challenging.

2.2 Theoretical wave types

Water waves differ to a greater or lesser extent from the ideal sinusoidal profile shown in Figure 2-1, which may be described for small dimensions ($H/h < 0.03$ and $H/L < 0.006$) by the linear wave theory (Dean and Dalrymple 2004). Here a few special non-linear water waves are discussed (Section 2.1), which have been relatively well studied, both theoretically and experimentally. The four wave types presented below are relevant, as all landslide-generated impulse waves may be allocated to one of the following groups: a) Stokes wave, b) cnoidal wave, c) solitary wave and d) bore.

a) Stokes wave

Figure 2-3 shows the profile of a Stokes wave, which is a deep-water to intermediate-water wave and may therefore be applied, for example, for wind generated waves. The Stokes wave is steeper than the sinusoidal wave in Figure 2-1, and the wave trough is somewhat flatter and longer than the wave peak. The water particles do not move in a closed orbital fashion and, in consequence, slight transport of fluid mass takes place.

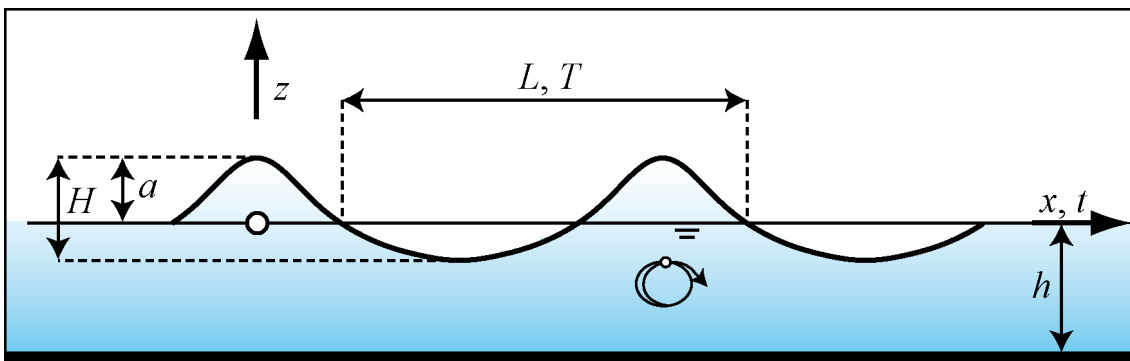


Figure 2-3 Stokes wave profile showing the most important wave parameters; slight fluid mass transport.

b) Cnoidal wave

Figure 2-4 shows a cnoidal wave, which is a periodic wave in intermediate or shallow-water. Wind generated waves in shallow-water, for example, may be described with this theory. The cnoidal wave has mainly an oscillatory character, but also exhibits open water particle orbits and hence transport of fluid mass. Using the equation for cnoidal waves, both linear waves (sinus waves) and solitary waves are included as limiting cases.

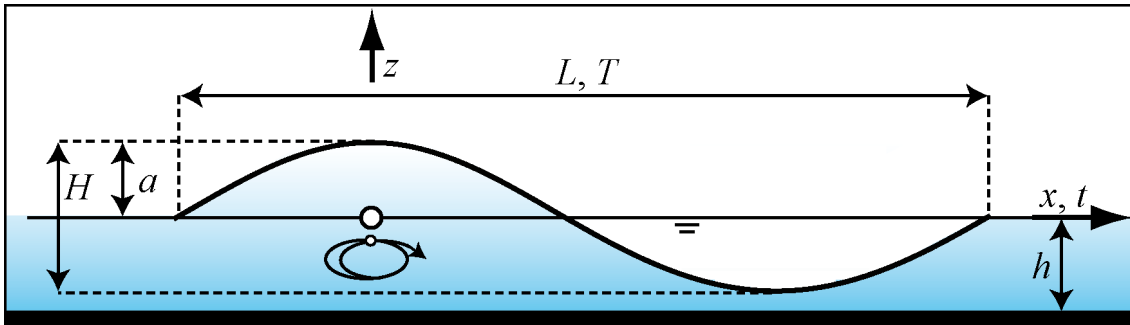


Figure 2-4 Cnoidal wave profile showing the most important wave parameters; slight fluid mass transport.

c) Solitary wave

A solitary wave is shown in Figure 2-5. Classic tsunamis, which are caused by the movement of tectonic plates, have often been approximated with the solitary wave theory (Madsen *et al.* 2008 show that this is not always the best approximation). This is the non-linear water wave which has been most researched, both by numerical simulations and laboratory experiments. It consists only of a wave peak but no trough. The wave amplitude is thus equal to the wave height $a = H$. In addition, the wave length $L = \infty$ and the wave is classed as a shallow-water wave ($L/h > 20$).

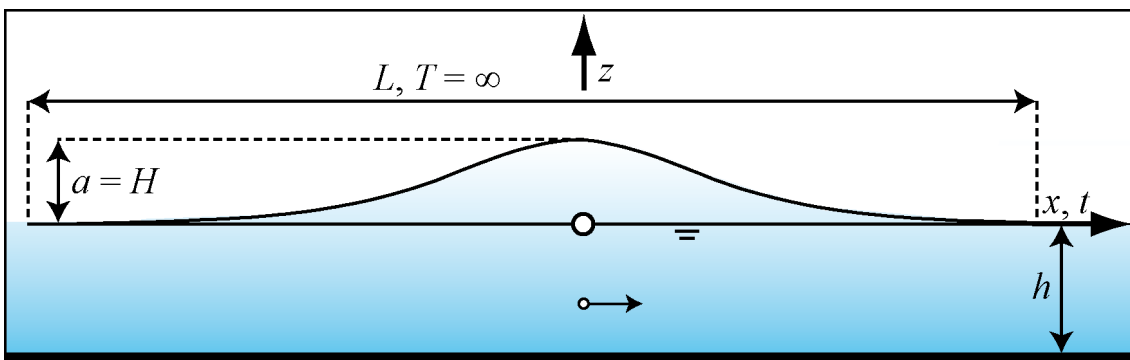


Figure 2-5 Solitary wave profile showing the most important wave parameters; major fluid mass transport.

Movement of the water particles is horizontal and as a consequence there is large fluid mass transport. In a rectangular channel on a horizontal bed, the height of this type of wave in theory does not decrease and the wave may propagate over unlimited distances without any change of shape. In reality, turbulence, created mainly on the bed of the ocean or lake, results in some reduction of wave height, but this is still less than occurs with other wave types. If the reservoir geometry deviates from rectangular then a pure solitary wave is not observed and the leading wave crest is followed by a trough. The solitary wave theory can be developed from the cnoidal wave theory for the wave period $T \rightarrow \infty$. The wave celerity of solitary waves is given by

$$c = [g(h + a)]^{1/2}. \quad (2.2)$$

a [m]	=	Wave amplitude (Figure 2-1)
c [m/s]	=	Wave celerity
g [m/s ²]	=	Gravitational acceleration; $g = 9.81$ m/s ²
h [m]	=	Still water depth

If the wave amplitude a of a solitary wave above a horizontal bed exceeds $0.78h$, the wave breaks and moves on as a bore. However, this process cannot realistically be described analytically.

d) Bore

Figure 2-6 shows a bore, which is created e.g. by a very violent slide impact in the slide impact zone or during wave breaking near the shore when air is entrained at the crest or when the top of the crest curls over. A bore is a shallow-water wave with horizontal particle movement which thus transports large fluid masses. Its profile is characterised by a steep front and a gently sloped back.

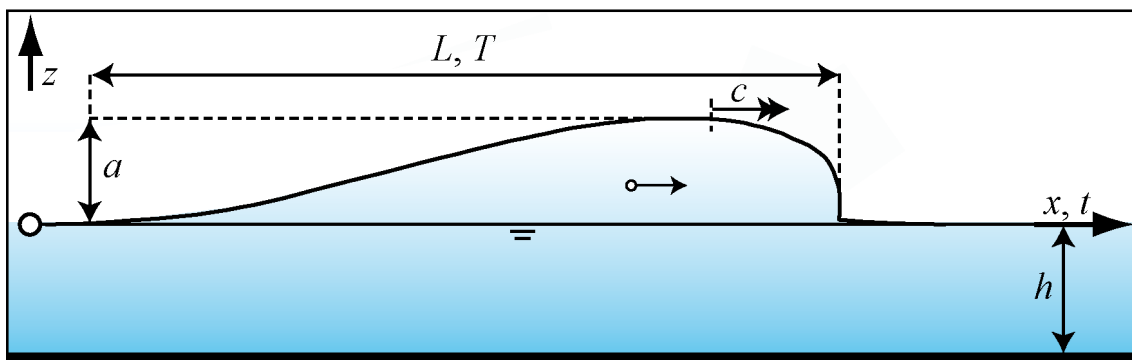


Figure 2-6 Wave profile of a bore with the most important wave parameters; large fluid mass transport.

The four wave types Stokes, cnoidal and solitary waves, as well as bore, described above, will sometimes be used in this manual for classifying impulse waves.

3 Computational procedure and Step 1

3.1 Introduction

Chapter 3 presents the procedure to determine the effects of landslide-generated impulse waves on dams, valid for slide masses originally located above the water surface (Figure 1-1). Figure 3-1 summarises the computational procedure with the corresponding literature references and the section references to this manual. Some of the original methods have been further developed or supplemented, or the corresponding equations were adjusted. The approach involves two steps (Figure 3-1).

Step 1 applies generally applicable equations. With regard to the wave generation, a distinction between studies based on a prismatic wave channel (2D) and those in a rectangular wave basin (3D) is made (Figure 3-3). Both methods are justified in practice and cover the extreme cases of restricted lateral and completely free radial propagation of the impulse waves above a horizontal sea or reservoir bed (Figure 3-2). The 2D equations were developed by Heller (2007) and Heller and Hager (2010), based on Zweifel (2004) and Fritz (2002). For 3D conditions, the equations were developed by Evers (2017) and Evers *et al.* (2019).

In contrast to those covering the wave generation, the generally applicable equations governing the effects of impulse waves on dams are based only on 2D models. In other words, 3D effects such as a curved dam shape are not taken into account. The run-up height on constantly inclined slopes is computed using the equation of Evers and Boes (2019), including the experiments by Müller (1995), as shown in Figure 3-1. Overland flow on horizontal foreshores is covered by the equations of Fuchs (2013) and Fuchs and Hager (2015). Wave overtopping at dams is considered for rigid dam structures including vertical walls (Kobel *et al.* 2017). For the computation of the wave force on dams two scenarios are relevant: wave force solely due to wave run-up and wave force due to wave run-up combined with overtopping. For the former scenario, the method by Ramsden (1996) is applied assuming that the upstream dam face is vertical ($\beta = 90^\circ$) with full force effect but no overtopping. For the latter scenario, a corresponding force reduction method is applied. To analyse dams with sloping upstream faces ($\beta < 90^\circ$), the forces must be decomposed into their horizontal and vertical components. To simplify the procedures for this resolution, the total loading is assumed to be static as for the moment of the maximum run-up height, practically all kinetic energy is converted into potential wave energy.

In Step 2, once the results of the generally applicable equations are available, the effects of deviations from the idealised reservoir geometry (prismatic, channel form geometry, rectangular basin shape; Section 4.2) are considered, as well as those of the mass movement type (granular slide; Section 4.4). These variations may lead to significant differences in the results obtained. Moreover, edge waves (Section 4.3) and the run-out distance of underwater landslide deposits (Section 4.5) are discussed. Only the

generally applicable equations of Step 1 are taken into account in the computational tool; Step 2 in Figure 3-1 is also needed and must be carried out independently after the computational tool has been applied.

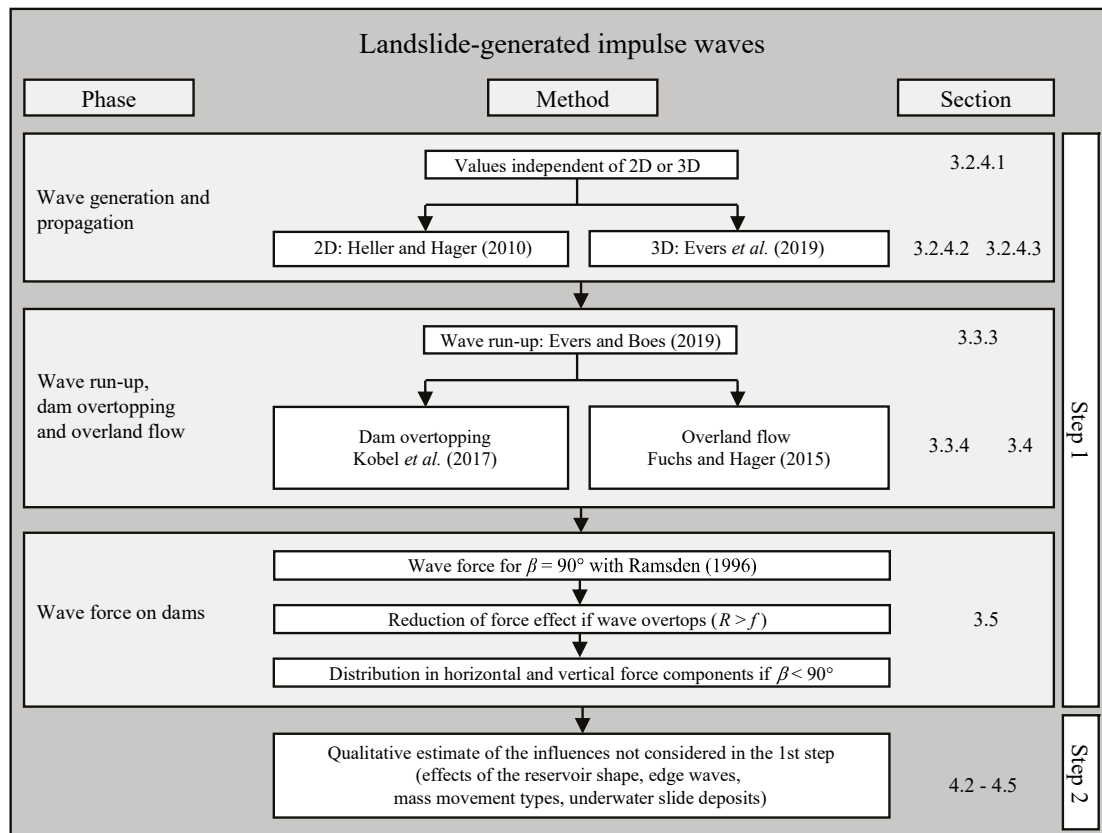


Figure 3-1 Computational procedure for landslide-generated impulse waves with the impulse wave phases, computation methods and references to the sections.

Chapter 3 is set out to follow the procedure shown in Figure 3-1. Section 3.2 addresses the wave generation and propagation. The individual equations are presented, after an introduction and the definition and explanation of the relevant governing parameters. The slide velocity at the point of impact is the most important governing parameter and is discussed in more detail. Distinctions are made between equations that are valid for both 2D and 3D, equations for a channel-form reservoir geometry (2D) and those for a basin-form geometry (3D). This differentiation covers the extreme cases of restricted lateral (2D) and completely free radial (3D) wave propagation in reservoirs (Figure 3-2). The results from Section 3.2 serve as governing parameters for the computation of the effects of impulse waves on dams as well as on the shore (Sections 3.3 to 3.5). Equations for the computation of wave run-up and wave overtopping are presented in Section 3.3. Section 3.4 addresses the relevant governing parameters for overland flow. The forces acting on the dam can then be computed by using the procedure outlined in Section 3.5. Assuming hydrostatic pressure in Subsection 3.5.2, methods for both wave run-up and overtopping are discussed in Subsection 3.5.3.

3.2 Wave generation and propagation

3.2.1 Introduction

The procedure is based on generally applicable equations. For wave generation, these were developed by laboratory tests either (a) in a prismatic wave channel (2D) or (b) in a rectangular wave basin (3D) (Section 3.1). The two extreme cases (a) and (b) are shown in Figure 3-2 and can be described as follows:

- Extreme case (a): the slide mass impacts longitudinally into a long reservoir, the slide width being either the same as or greater than the reservoir width. The impulse waves are confined as they move along the reservoir and are not able to propagate laterally (Figure 3-2a).
- Extreme case (b): the slide mass impacts at any possible location into the reservoir, and the slide width is less than that of the reservoir. The reservoir geometry is such that impulse waves can propagate radially and completely free from the slide impact zone (Figure 3-2b).

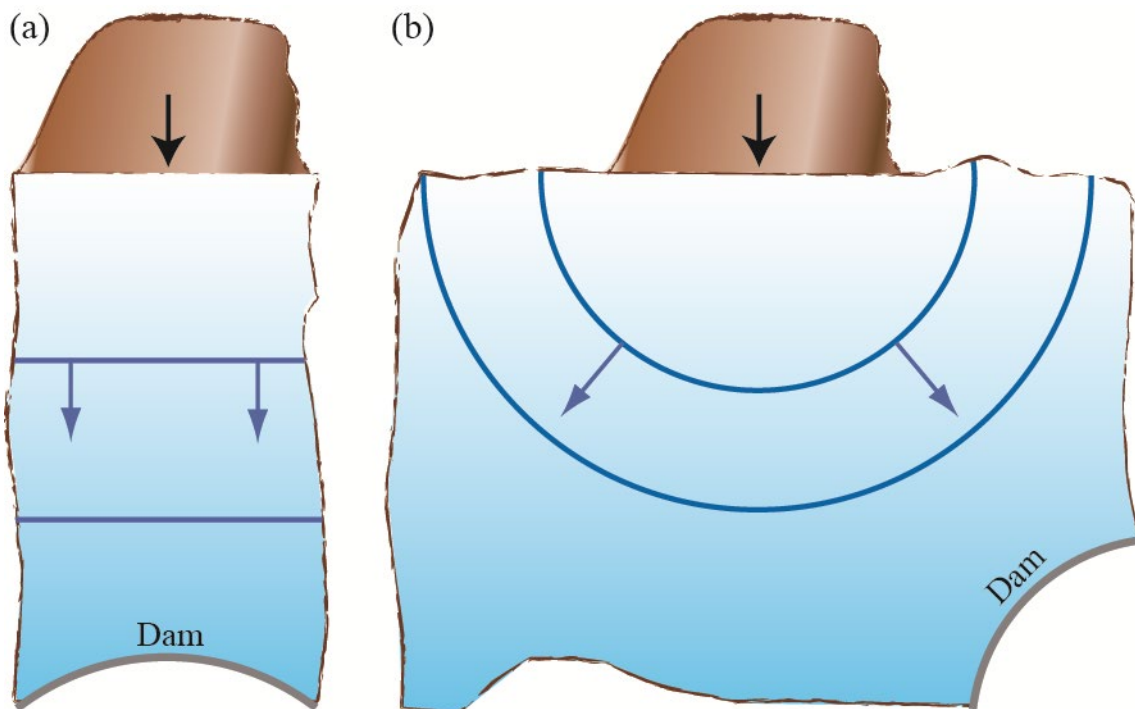


Figure 3-2 Reservoir geometries for two idealised cases described directly with generally applicable equations: extreme case (a) (2D) with longitudinal impacting slide and confined lateral wave propagation, extreme case (b) (3D) with the slide impacting across the reservoir and completely free radial wave propagation.

The same governing parameters are relevant for the computation of the wave generation for both extreme cases (a) and (b) (Subsection 3.2.2). Because impulse waves (and thus

their energy) propagate over a larger area in extreme case (b), the wave height decreases more rapidly than in case (a), i.e. the attenuation rates differ for the two cases (Subsection 4.2.1).

To extrapolate the results of model tests to prototypes, geometrical similarity must exist between them. Deviations of the geometry may result in model effects, for example, the relative wave heights do not correspond between model and prototype. The more the actual shape of the reservoir deviates from the two idealised geometries 2D and 3D, the more dominant will be effects such as wave reflection, shoaling or constriction. In this case, the limiting values for extreme cases (a) and (b) may even be exceeded. As a result, greater insecurity in the determination of the wave parameters has to be expected for geometries significantly deviating from 2D and 3D. The procedures in Sections 4.2 and 4.3 then become important. Alternatively, more precise predictions may be possible with a prototype-specific model test or a numerical simulation (Section 1.2).

3.2.2 Governing parameters

Figure 3-3 shows sketches defining the relevant parameters for the impulse wave generation in (a) channel-shape (2D) as well as for (b) basin-shape (3D) reservoirs. The following parameters have an effect on the computations of the key wave characteristics including wave heights and amplitudes in both 2D and 3D cases:

- Slide impact velocity V_s
- Bulk slide volume V_s
- Slide thickness s
- Slide width or reservoir width b
- Bulk slide density ρ_s
- Bulk slide porosity n
- Slide impact angle α
- Still water depth h

The origin of the coordinate system (x, z) is the intersection of the still water level and the slide slope (Figure 3-3a). The governing slide parameters are related to the impact location and not to the original slide position. All seven slide parameters given above may vary between the original position of the slide and its impact location. The bulk slide volume V_s and the bulk slide density ρ_s comprise the bulk slide porosity n . This is neither introduced as an independent parameter in the computational procedure, nor is the slide mass $m_s = V_s \rho_s$. The bulk slide volume V_s and the bulk slide density ρ_s , which consider the bulk slide porosity n , must be distinguished from the slide grain volume V_g and grain density ρ_g . The equations for conversion between grain and bulk slide properties are given in Table 3-1.

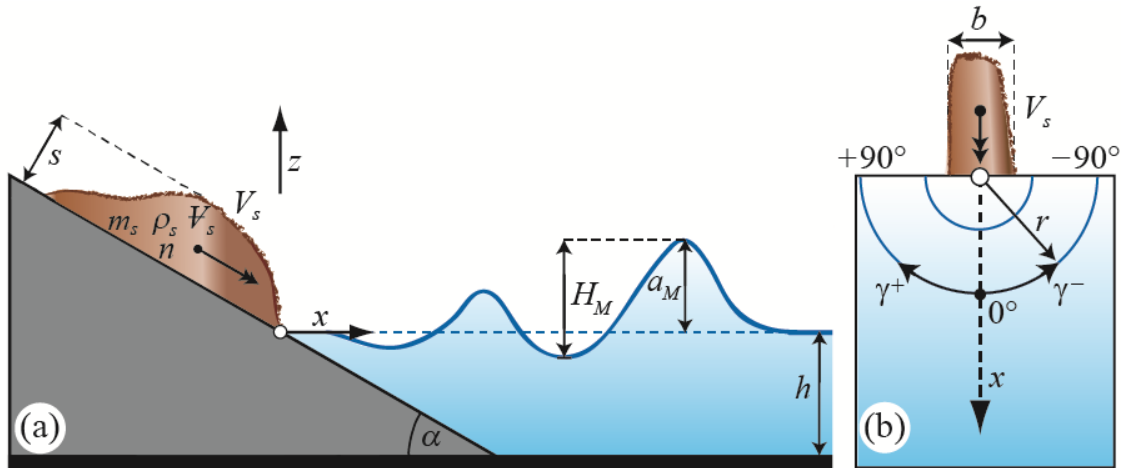


Figure 3-3 Sketches defining the governing parameters on impulse wave generation, the most important wave parameters (for extreme case 2D) and the coordinate systems for (a) 2D and (b) 3D.

Table 3-1 Conversion of grain to bulk slide parameters, and vice versa, using the bulk slide porosity n .

	Granulate properties	Slide properties
Density	$\rho_g = \rho_s / (1 - n)$	$\rho_s = (1 - n) \rho_g$
Volume	$V_g = (1 - n) V_s$	$V_s = V_g / (1 - n)$

The slide thickness s is the maximum thickness of the slide measured perpendicular to the slide slope at the moment of impact. The slide width b should be selected as the average width during impact. If the slide width is greater than that of the reservoir in the 2D case, then the reservoir width should be taken for b . The slide impact angle α is the hill slope angle at the impact location, measured as the angle from the horizontal (Figure 3-3a). This defines the momentum transmission angle of the slide on the water body. The still water depth h is taken as the average depth in the slide impact zone, along the slide axis ($\gamma = 0^\circ$; Figure 3-3). If an average depth may not be clearly determined, a sensitivity analysis covering a representative depth range is recommended (Section 4.6).

Changes of a generated impulse wave when propagating in reservoirs of horizontal, channel-shape or basin-shape geometry are described by the parameters (Figure 3-3):

- Distance x (2D)
- Radial distance r (3D)
- Wave propagation angle γ (3D)

In a channel-shape reservoir (2D; Figure 3-3a), the impulse wave changes only with regard to distance x . In a basin-shape reservoir (3D; Figure 3-3b), both the radial distance r and the wave propagation angle γ are involved.

3.2.3 Slide velocity at the point of impact

As one important governing parameter, the derivation of the slide velocity at the point of impact is discussed in this section. Note that the acceleration of the slide and the subsequent movement depends on the inclination of the slope along which the slide accelerates, whilst the generation of the impulse wave depends among other factors on the slide impact angle α . For most of the derivations in this section, it is assumed that α is the same as the inclination angle of the slope and will be used interchangeably. The final subsection gives some indications on how to account for slope changes along the traveling path of the slide. Examples 1, 2 and 4 in Chapter 5 provide details on the application of the equations presented in this section.

Slides in soil material

The slide impact velocity V_s is that of the centre of gravity of the slide mass during impact and can be expressed via the energy equation:

$$\frac{1}{2} m_s V_s^2 = m_s a_s \Delta_{sc} . \quad (3.1)$$

Equation (3.1) can be solved for V_s at the point of entry:

$$V_s = \sqrt{2a_s \Delta_{sc}} = \sqrt{2a_s \frac{\Delta z_{sc}}{\sin \alpha}} . \quad (3.2)$$

a_s [m/s ²]	=	Slide acceleration
m_s [kg]	=	Slide mass
V_s [m/s]	=	Slide impact velocity (Figure 3-4)
α [°]	=	Slide impact angle (Figure 3-4)
Δ_{sc} [m]	=	Travel distance of the centre of gravity before entering the water body
Δz_{sc} [m]	=	Drop height of centre of gravity of the slide (Figure 3-4)

The acceleration of the landslide a_s is the result of unbalanced driving and resisting forces acting on the sliding mass. Without additional external stimulus this means for slides composed of granular, purely frictional material:

$$G_s \sin \alpha > G'_s \cos \alpha \tan \delta \quad \rightarrow \quad m_s a_s = G_s \sin \alpha - G'_s \cos \alpha \tan \delta \quad (3.3)$$

and thus

$$a_s = \frac{G_s \sin \alpha - G'_s \cos \alpha \tan \delta}{m_s} \text{ with } G'_s = f(u). \quad (3.4)$$

a_s [m/s ²]	= Slide acceleration
G_s [N]	= Total weight of the slide
G'_s [N]	= Effective slide weight in function of the pore pressure u
m_s [kg]	= Slide mass
u [kPa]	= Pore water pressure
α [°]	= Slide impact angle (Figure 3-4)
δ [°]	= Dynamic bed friction angle (Figure 3-4)

If there is no pore water pressure influencing the shear resistance (e.g. dry soil or rock slides), then Eqs. (3.2) and (3.4) can be combined and simplified (Körner 1976) to

$$V_s = \sqrt{2g\Delta z_{sc} (1 - \tan \delta \cot \alpha)}. \quad (3.5)$$

g [m/s ²]	= Gravitational acceleration; $g = 9.81$ m/s ²
V_s [m/s]	= Slide impact velocity (Figure 3-4)
α [°]	= Slide impact angle (Figure 3-4)
δ [°]	= Dynamic bed friction angle (Figure 3-4)
Δz_{sc} [m]	= Drop height of centre of gravity of the slide (Figure 3-4)

In other cases, e.g. if the landslide contains water and thus the influence of pore water pressure has to be accounted for, Eq. (3.4) has to be solved to obtain the slide acceleration.

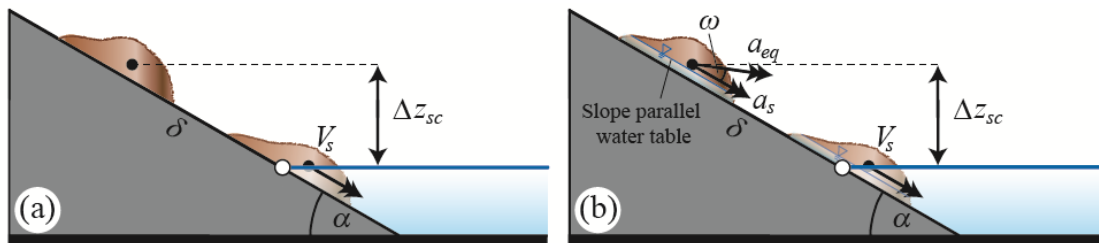


Figure 3-4 Sketches defining the parameters to determine the slide impact velocity V_s on slopes of constant slide impact angle α for (a) dry soil or rock slides and (b) the effect of external stimulus.

The parameters in Eq. (3.5) are shown in Figure 3-4(a) for a slope of constant inclination. The drop height of the centre of gravity of the slide Δz_{sc} is the vertical distance

between the centre of gravity of the slide mass in its original position and the still water level. The dynamic bed friction angle δ represents the friction at the contact between the slide mass and the underlying stable slope. The greater this friction, the greater is the value of δ which is typically in the range $15^\circ \leq \delta \leq 35^\circ$. The value for α is equal to the average slope angle in this example.

For potentially undrained or partly undrained slide failure (i.e. at the interface between the sliding mass and the stable ground) soil softening due to development of excess pore pressures has to be accounted for.

Using total stress analysis the acceleration of the slide may be computed as

$$a_s = \frac{G_s \sin \alpha - A_s s_u}{m_s} \quad (3.6)$$

Alternatively, when the computation is based on effective stresses, the development of excess pore pressures has to be accounted for and Eq. (3.4) becomes

$$a_s = \frac{G_s \sin \alpha - G'_s \cos \alpha \tan \delta}{m_s} \quad \text{with } G'_s = f(u, \Delta u). \quad (3.7)$$

A_s [m ²]	=	Area of the slip surface i.e. contact area between slide and stable ground
G_s [N]	=	Total weight of the slide
G'_s [N]	=	Effective weight of the slide as function of - the pore pressure u and - the excess pore pressure Δu
m_s [kg]	=	Slide mass
s_u [kPa]	=	Undrained shear strength of the slip surface
u [kPa]	=	Pore water pressure
α [°]	=	Slide impact angle (Figure 3-4)
Δu [kPa]	=	Excess pore pressure

Additional external stimulus

An external stimulus due to seismic loading has also to be accounted for (Figure 3-4b). As a conservative first estimate the acceleration of the slide can be determined by introducing an external driving force $F_{ext} = m_s a_{eq}$ for the duration of an earthquake:

$$a_s = \frac{G_s \sin \alpha - G'_s \cos \alpha \tan \delta + m_s a_{eq} \cos \omega + m_s a_{eq} \sin \omega \tan \delta}{m_s} \quad (3.8)$$

a_{eq} [m/s ²]	=	Earthquake induced acceleration
a_s [m/s ²]	=	Acceleration of the slide
G_s [N]	=	Total weight of the slide
G'_s [N]	=	Effective weight of the slide
m_s [kg]	=	Slide mass
α [°]	=	Slide impact angle (Figure 3-4)
δ [°]	=	Dynamic bed friction angle (Figure 3-4)
ω [°]	=	Angle between the direction of the earthquake induced acceleration and the slope

Alternatively, more sophisticated methods, such as Newmark's sliding block method (Newmark 1965) or dynamic finite element analyses, in combination with acceleration time histories, can be applied to compute the slide displacement and velocity.

Other types of slides

For other types of slides such as snow avalanches, flow avalanches or rock falls, adequate models to derive the slide thickness s and slide impact velocity V_s have to be used. E.g. Salm *et al.* (1990) address the derivation of the slide thickness s and the slide impact velocity V_s for flow avalanches.

Slides with slope inclination changes

If at any point the gradient of the slope changes significantly, as shown in Figure 3-5, the slide velocity at this point V_{sNK} may be computed with Eq. (3.5) by introducing values for the relevant parameters Δz_{scN} , δ_N and α_N . Assuming that the dissipation of the kinetic energy due to the slope change is negligible, the increase of the slide velocity to the slide impact velocity V_s is then determined from Eq. (3.6), with the value of V_{sNK} computed as shown e.g. in the previous sections

$$V_s = \sqrt{V_{sNK}^2 + 2a_s \Delta z_{sc}} = \sqrt{V_{sNK}^2 + 2a_s \frac{\Delta z_{sc}}{\sin \alpha}} \quad (3.9)$$

$$\text{where } V_{sNK} = \sqrt{2a_{sNK} \Delta z_{scN}} = \sqrt{2a_{sNK} \frac{\Delta z_{scN}}{\sin \alpha_N}} \quad (3.10)$$

For dry granular material, Eq. (3.10) can directly be expressed as a function of the dynamic bed friction angles, slope inclinations and drop heights (Figure 3-5)

$$V_s = \sqrt{2g \left[\Delta z_{scN} (1 - \tan \delta_N \cot \alpha_N) + \Delta z_{sc} (1 - \tan \delta \cot \alpha) \right]}. \quad (3.11)$$

a_s [m/s ²]	= Acceleration of the slide along the slope after the point of slope change (Figure 3-5)
a_{sNK} [m/s ²]	= Acceleration of the slide along the slope before the point of slope change (Figure 3-5)
g [m/s ²]	= Gravitational acceleration; $g = 9.81$ m/s ²
V_s [m/s]	= Slide impact velocity (Figure 3-5)
V_{sNK} [m/s]	= Slide velocity at point of slope change (Figure 3-5)
α [°]	= Slide impact angle (Figure 3-5)
δ [°]	= Dynamic bed friction angle (Figure 3-5)
Δz_{sc} [m]	= Drop height of centre of gravity of the slide (Figure 3-5)

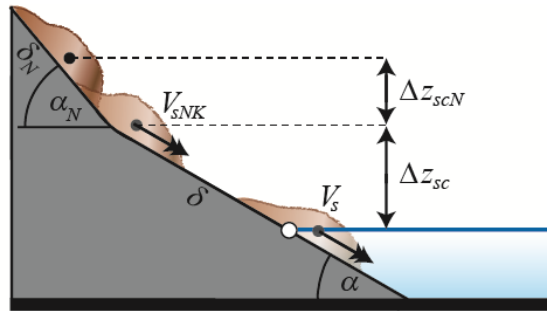


Figure 3-5 Sketch defining the parameters to determine the slide impact velocity V_s for slopes with a slope change.

For a number of slope changes, the analysis may proceed analogously. The slide velocity at the uppermost slope change can be computed according to the previous section by introducing the values of Δz_{scN} , δ_N and α_N , valid for the slope above the change. The obtained slide velocity V_{sNK} is then introduced in Eq. (3.10), together with the relevant values for the next slope section. For each successive slope section, the same Eq. (3.10) can be applied, introducing the values for the slope in question and the slide velocity at the end of the previous section. Eq. (3.2) is therefore a special case of Eq. (3.10) with $V_{sNK} = 0$.

3.2.4 Reservoir shape

3.2.4.1 Values independent of 2D or 3D

The equations given below are valid for both extreme cases (a) and (b) of idealised reservoir geometries as described in Subsection 3.2.1. Intermediate geometries have to be considered in Step 2 of the computational procedure (Section 4.2.1).

The impulse product parameter P by Heller (2007) and Heller and Hager (2010) has an important role in both 2D and 3D computations. It is defined as

$$P = FS^{1/2}M^{1/4}\{\cos[(6/7)\alpha]\}^{1/2}. \quad (3.12)$$

b [m]	=	Slide width (Figure 3-3b)
F [-]	=	Slide Froude number; $F = V_s/(gh)^{1/2}$
g [m/s ²]	=	Gravitational acceleration; $g = 9.81$ m/s ²
h [m]	=	Still water depth (in the slide impact zone)
M [-]	=	Relative slide mass; $M = \rho_s V_s / (\rho_w b h^2)$
P [-]	=	Impulse product parameter
s [m]	=	Slide thickness (Figure 3-3a)
S [-]	=	Relative slide thickness; $S = s/h$
V_s [m/s]	=	Slide impact velocity, e.g. from Eq. (3.1) or Eq. (3.2) (Figure 3-3a)
V_s [m ³]	=	Bulk slide volume (Figure 3-3a)
α [°]	=	Slide impact angle (Figure 3-3a)
ρ_s [kg/m ³]	=	Bulk slide density (Figure 3-3a)
ρ_w [kg/m ³]	=	Water density

Apart from the water density ρ_w and the gravitational acceleration g , the value of P is determined only from governing parameters and can therefore be estimated prior to any slide event. The significance of the dimensionless values F , S , M and α , as applied in Eq. (3.12), is discussed by Heller (2007) and Heller and Hager (2010).

In the equations given below, slide densities from compact snow to granite, slide impact angles from 30° to 90°, and distances from the coordinate origin of up to $59h$ for the 2D case and $16h$ for the 3D case, respectively, are taken into account, as these represent the experimental parameters ranges on which the equations are based. In practice, the *limitations* given in Tables 3-2 and 3-3 must be respected when using this procedure.

3.2.4.2 Extreme case (a) (2D)

The equations presented here are based on Heller (2007) and Heller and Hager (2010) (Figure 3-1). They apply for the computation of impulse waves propagating longitudinally in a laterally confined reservoir, following the impact of a slide mass in the streamwise direction (Figure 3-2a; extreme case (a) in Subsection 3.2.1). With regard to the effects of impulse waves on dams, above all the wave height H and the wave amplitude a are of particular importance. In addition, the wave length L and the wave period T are taken into consideration which, according to the linear wave theory, are connected with the wave celerity c as $L = Tc$ (Section 2.1). The maximum wave height H_M in the slide impact zone is often formed by a wall of water rather than by a stable wave. For this reason, it will be distinguished between the maximum wave height H_M in the slide

impact zone and the wave height H in the wave propagation zone. The former may be determined as

$$H_M = (5/9)P^{4/5}h. \quad (3.13)$$

h [m]	=	Still water depth (in the slide impact zone)
H_M [m]	=	Maximum wave height (Figure 3-3a)
P [-]	=	Impulse product parameter from Eq. (3.12)

The distance of the maximum wave height from the slide impact location x_M is given by

$$x_M = (11/2)P^{1/2}h. \quad (3.14)$$

h [m]	=	Still water depth (in the slide impact zone)
P [-]	=	Impulse product parameter from Eq. (3.12)
x_M [m]	=	Streamwise distance of the maximum wave amplitude from the impact location (Figure 3-3a)

The wave period T_M of the maximum wave height H_M can be computed as

$$T_M = 9P^{1/2}(h/g)^{1/2}. \quad (3.15)$$

g [m/s ²]	=	Gravitational acceleration; $g = 9.81$ m/s ²
h [m]	=	Still water depth (in the slide impact zone)
H_M [m]	=	Maximum wave height (Figure 3-3a)
P [-]	=	Impulse product parameter from Eq. (3.12)
T_M [s]	=	Wave period of H_M

The value of the wave amplitude a is determined indirectly from the wave height H , by applying Eqs. (3.13) or (3.19). For a known wave height H , the wave amplitude a is

$$a = (4/5)H. \quad (3.16)$$

a [m]	=	Wave amplitude (Figure 3-3a)
H [m]	=	Wave height from Eqs. (3.13) or (3.19) (Figure 3-3a)

The wave trough is thus equal on average to only about 20% of the wave height H in 2D (Figure 3-3a).

The wave celerity c is determined using the equation for the solitary wave celerity

$$c = [g(h+a)]^{1/2}. \quad (3.17)$$

a [m]	=	Wave amplitude (Figure 3-3a)
c [m/s]	=	Wave celerity
g [m/s ²]	=	Gravitational acceleration; $g = 9.81$ m/s ²
h [m]	=	Still water depth

The value of c can be determined locally or between two points. In the latter case, the average values of a and h , between the two points, are introduced into Eq. (3.17). An impulse wave with an amplitude of $a = 20$ m in $h = 100$ m deep water will have a celerity c of about 34 m/s or 124 km/h.

With T_M from Eq. (3.15), and with the linear relation $L = Tc$, the wave length L_M of H_M can be determined as

$$L_M = T_M c. \quad (3.18)$$

c [m/s]	=	Solitary wave celerity from Eq. (3.17)
H_M [m]	=	Maximum wave height (Figure 3-3a)
L_M [m]	=	Wave length of H_M
T_M [s]	=	Wave period of H_M

For the evaluation of wave run-up, the wave height at the dam or reservoir shore is required, and not only the maximum wave height H_M in the slide impact zone. Furthermore, the streamwise coordinate x must be considered (Figure 3-3a). If the wave height H sought is located farther from the slide impact location than where the maximum wave height H_M occurs ($x/h = X > X_M = x_M/h$), then the wave height H follows

$$H(x) = (3/4) \left(P X^{-1/3} \right)^{4/5} h \quad \text{for } X > X_M. \quad (3.19)$$

h [m]	=	Still water depth (in the slide impact zone)
H [m]	=	Wave height (Figure 3-3a)
P [-]	=	Impulse product parameter from Eq. (3.12)
x [m]	=	Streamwise coordinate in the longitudinal channel direction (Figure 3-3a)
x_M [m]	=	Streamwise distance of the maximum wave amplitude from the impact location
X [-]	=	Relative streamwise distance; $X = x/h$
X_M [-]	=	Relative streamwise distance of the maximum wave amplitude from the impact location; $X_M = x_M/h$

Equation (3.19) is only to be used when $x > x_M$. The wave period $T(x)$ is determined as (Heller *et al.* 2009)

$$T(x) = 9P^{1/4} X^{5/16} (h/g)^{1/2} \quad \text{for } X > X_M. \quad (3.20)$$

g [m/s ²]	=	Gravitational acceleration; $g = 9.81$ m/s ²
h [m]	=	Still water depth (in the slide impact zone)
P [-]	=	Impulse product parameter from Eq. (3.12)
T [s]	=	Wave period (Figure 3-3a)
x [m]	=	Streamwise coordinate in the longitudinal channel direction (Figure 3-3a)
x_M [m]	=	Streamwise distance of the maximum wave amplitude from the impact location
X [-]	=	Relative streamwise distance; $X = x/h$
X_M [-]	=	Relative streamwise distance of the maximum wave amplitude from the impact location; $X_M = x_M/h$

Again, in accordance with the linear wave theory, the wave length $L(x)$ is determined from

$$L(x) = T(x)c(x). \quad (3.21)$$

c [m/s]	=	Solitary wave celerity from Eq. (3.17)
L [m]	=	Wave length (Figure 3-3a)
T [s]	=	Wave period from Eq. (3.20) (Figure 3-3a)
x [m]	=	Streamwise coordinate in longitudinal channel direction (Figure 3-3a)

Equations (3.12) to (3.21) were empirically derived from laboratory experiments. Therefore, the parameters must be kept within the limitations given in Table 3-2 for practical applications.

Table 3-2 Limitations to compute the 2D impulse wave generation and propagation.

Term	Range	Definition
Slide Froude number	$0.86 \leq F \leq 6.83$	$F = V_s/(gh)^{1/2}$
Relative slide thickness	$0.09 \leq S \leq 1.64$	$S = s/h$
Relative slide mass	$0.11 \leq M \leq 10.02$	$M = \rho_s V_s / (\rho_w b h^2)$
Relative slide density	$0.59 \leq D \leq 1.72$	$D = \rho_s / \rho_w$
Relative granulate density	$0.96 \leq \rho_g / \rho_w \leq 2.75$	ρ_g / ρ_w
Relative slide volume	$0.05 \leq V \leq 5.94$	$V = V_s / (b h^2)$
Bulk slide porosity	$30.7\% \leq n \leq 43.3\%$	n
Slide impact angle	$30^\circ \leq \alpha \leq 90^\circ$	α
Relative slide width	$0.74 \leq B \leq 3.33$	$B = b/h$
Relative streamwise distance	$2.7 \leq X \leq 59.2$	$X = x/h$
Impulse product parameter	$0.17 \leq P \leq 8.13$	$P = FS^{1/2} M^{1/4} \{\cos[(6/7)\alpha]\}^{1/2}$

3.2.4.3 Extreme case (b) (3D)

The equations for the 3D case are based on Evers (2017) and Evers *et al.* (2019) (Figure 3-1). They can be used to analyse impulse waves propagating radially and completely freely in a reservoir (Figure 3-2b; extreme case (b) in Section 3.2.1). The governing slide parameters are identical to the 2D case shown in Figure 3-3(a). However, in contrast to the 2D case, wave parameters are predicted depending on their position in the impulse wave train (Figure 3-6a).

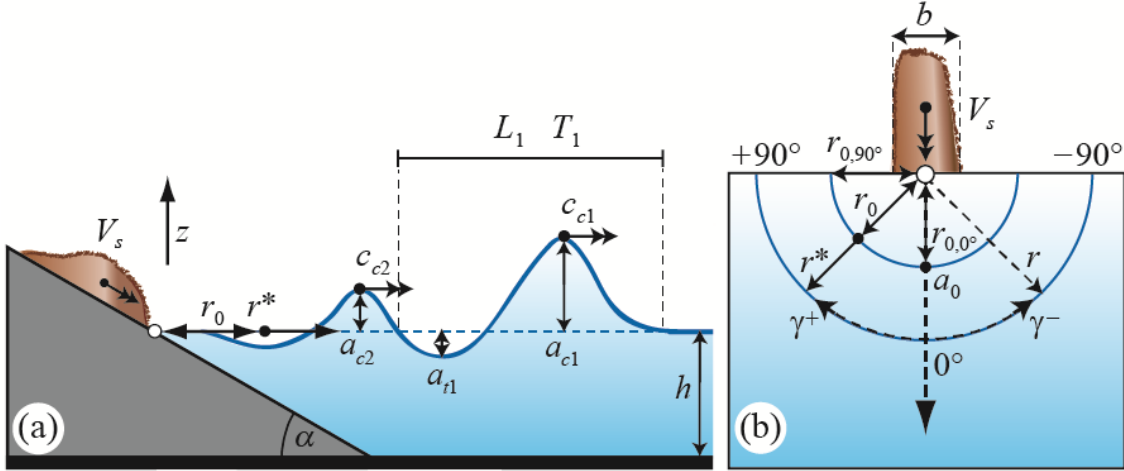


Figure 3-6 Sketches defining the most important wave parameters (for extreme case 3D) and the coordinate system.

The slide impact zone is delimited by the impact radius r_0 (Figure 3-6). For $r < r_0$, no distinct wave features may be predicted due to the highly turbulent slide-water interactions related to the wave generation process. Depending on the slide characteristics, r_0 ranges between one and five times the still water depth. The elliptical extent of the slide impact zone r_0 is determined based on the impact radii $r_{0,0^\circ}$ and $r_{0,90^\circ}$ for $\gamma = 0^\circ$ and 90° , respectively, with

$$r_{0,0^\circ} = 2.5 \left(P \left(\frac{b}{h} \right) \cos \alpha_{\text{eff}} \right)^{0.25} h \quad \text{for } \gamma = 0^\circ, \quad (3.22)$$

$$r_{0,90^\circ} = \left(\frac{b}{2} \right) + 1.5 \left(P \cos \alpha_{\text{eff}} \right)^{0.25} h \quad \text{for } \gamma = \pm 90^\circ, \quad (3.23)$$

$$r_0(\gamma) = \sqrt{\frac{r_{0,0^\circ}^2 r_{0,90^\circ}^2}{r_{0,0^\circ}^2 \sin^2 \gamma + r_{0,90^\circ}^2 \cos^2 \gamma}} \quad \text{for } -90^\circ < \gamma < +90^\circ. \quad (3.24)$$

b [m]	=	Slide width (Figure 3-6b)
h [m]	=	Still water depth (in the slide impact zone)
P [-]	=	Impulse product parameter from Eq. (3.12)
r_0 [m]	=	Impact radius (Figure 3-6)

$r_{0,0^\circ}$ [m]	=	Impact radius for $\gamma = 0^\circ$ (Figure 3-6b)
$r_{0,90^\circ}$ [m]	=	Impact radius for $\gamma = 90^\circ$ (Figure 3-6b)
α_{eff} [°]	=	Effective slide impact angle; $\alpha_{eff} = (6/7)\alpha$
γ [°]	=	Wave propagation angle (Figure 3-6b)

Outside the slide impact zone (Figure 3-6), the wave characteristics are computed based on the surrogate radial wave propagation distance r^* defined as

$$r^* = r - r_0 \quad \text{for } r \geq r_0. \quad (3.25)$$

r [m]	=	Radial distance from the impact location in the wave basin (Figure 3-6b)
r_0 [m]	=	Impact radius (Figure 3-6b)
r^* [m]	=	Surrogate radial distance from the impact location in the wave basin (Figure 3-6b)

The initial amplitudes of the first wave crest $a_{0,c1}$, first wave trough $a_{0,t1}$ and second wave crest $a_{0,c2}$ for $r^* = 0$ and $\gamma = 0^\circ$ (Figure 3-6b) may be determined with

$$a_{0,c1} = 0.2P^{0.5} \left(\frac{b}{h} \right)^{0.75} (\cos \alpha_{eff})^{0.25} h \quad \text{for } r^* = 0 \text{ and } \gamma = 0^\circ, \quad (3.26)$$

$$a_{0,t1} = 0.35 \left(P \left(\frac{b}{h} \right) \cos \alpha_{eff} \right)^{0.5} h \quad \text{for } r^* = 0 \text{ and } \gamma = 0^\circ, \quad (3.27)$$

$$a_{0,c2} = 0.14 \left(P \left(\frac{b}{h} \right) \cos \alpha_{eff} \right)^{0.25} h \quad \text{for } r^* = 0 \text{ and } \gamma = 0^\circ. \quad (3.28)$$

$a_{0,c1}$ [m]	=	Initial first wave crest amplitude (Figure 3-6)
$a_{0,c2}$ [m]	=	Initial second wave crest amplitude (Figure 3-6)
$a_{0,t1}$ [m]	=	Initial first wave trough amplitude (Figure 3-6)
b [m]	=	Slide width (Figure 3-6b)
h [m]	=	Still water depth (in the slide impact zone)
P [-]	=	Impulse product parameter from Eq. (3.12)
α_{eff} [°]	=	Effective slide impact angle; $\alpha_{eff} = (6/7)\alpha$

The initial height of the first wave is determined as the sum of the wave crest and trough amplitudes at the same location.

The amplitudes at any point beyond the impact radius r_0 , i.e. $r^* \geq 0$ and $-90^\circ \leq \gamma \leq 90^\circ$, of the first wave crest a_{c1} , first wave trough a_{t1} , and second wave crest a_{c2} (Figure 3-6b) may be determined with

$$a_{c1}(r^*, \gamma) = a_{0,c1} \exp \left[-0.4 \left(\frac{a_{0,c1}}{h} \right)^{-0.3} \sqrt{\frac{r^*}{h}} \right] \left[\operatorname{sech} \left(3.2 \frac{\gamma}{90^\circ} \right) \right]^{\cos \alpha_{eff} \exp \left(-0.15 \sqrt{\frac{r^*}{h}} \right)}, \quad (3.29)$$

$$a_{t1}(r^*, \gamma) = a_{0,t1} \exp \left[-0.4 \left(\frac{a_{0,t1}}{h} \right)^{-0.3} \sqrt{\frac{r^*}{h}} \right] \left[\operatorname{sech} \left(3.6 \frac{\gamma}{90^\circ} \right) \right]^{\cos \alpha_{eff} \exp \left(-0.15 \sqrt{\frac{r^*}{h}} \right)}, \quad (3.30)$$

$$a_{c2}(r^*, \gamma) = a_{0,c2} \exp \left[-0.1 \left(\frac{a_{0,c2}}{h} \right)^{-0.3} \sqrt{\frac{r^*}{h}} \right] \left[\operatorname{sech} \left(3 \frac{\gamma}{90^\circ} \right) \right]^{\cos \alpha_{eff} \exp \left(-0.15 \sqrt{\frac{r^*}{h}} \right)}. \quad (3.31)$$

$a_{0,c1}$ [m]	=	Initial first wave crest amplitude (Eq. 3.26) (Figure 3-6)
$a_{0,c2}$ [m]	=	Initial second wave crest amplitude (Eq. 3.27) (Figure 3-6)
$a_{0,t1}$ [m]	=	Initial first wave trough amplitude (Eq. 3.28) (Figure 3-6)
a_{c1} [m]	=	First wave crest amplitude (Figure 3-6)
a_{c2} [m]	=	Second wave crest amplitude (Figure 3-6)
a_{t1} [m]	=	First wave trough amplitude (Figure 3-6)
h [m]	=	Still water depth (in the slide impact zone)
r^* [m]	=	Surrogate radial distance from the impact location in the wave basin (Figure 3-6b)
γ [°]	=	Wave propagation angle (Figure 3-6b)

Equations (3.29) to (3.31) include hyperbolic secant functions (sech) to describe the wave amplitude shape along γ . Similar to the initial wave amplitudes, wave heights are determined as the sum of wave crest and trough amplitudes at the same location.

The celerities of the first and second wave crests c_{c1} and c_{c2} are given as a fraction of the solitary wave celerity c (Eq. 3.17) with

$$c_{c1}(r^*, \gamma) = 0.95 \sqrt{g(h + a_{c1})}, \quad (3.32)$$

$$c_{c2}(r^*, \gamma) = 0.7 \sqrt{g(h + a_{c2})}. \quad (3.33)$$

a_{c1} [m]	=	First wave crest amplitude from Eq. (3.29) (Figure 3-6)
a_{c2} [m]	=	Second wave crest amplitude from Eq. (3.31) (Figure 3-6)
c_{c1} [m/s]	=	First wave crest celerity (Figure 3-6)
c_{c2} [m/s]	=	Second wave crest celerity (Figure 3-6)
g [m/s ²]	=	Gravitational acceleration; $g = 9.81$ m/s ²
h [m]	=	Still water depth

The period of the first wave T_1 may be determined with

$$T_1(r^*, \gamma) = \left[10 \left(\frac{a_{c1} + a_{t1}}{h} \right)^{0.2} + \frac{r^*}{2h} \right] \sqrt{\frac{h}{g}} \quad (3.34)$$

a_{c1} [m]	=	First wave crest amplitude from Eq. (3.29) (Figure 3-6)
a_{t1} [m]	=	First wave trough amplitude from Eq. (3.30) (Figure 3-6)
g [m/s ²]	=	Gravitational acceleration; $g = 9.81$ m/s ²
h [m]	=	Still water depth
r^* [m]	=	Surrogate radial distance from the impact location in the wave basin (Figure 3-6)
T_1 [s]	=	First wave period (Figure 3-6)

In analogy to the 2D case, the wavelength L_1 of the first wave, again according to the linear wave theory, is given by

$$L_1(r^*, \gamma) = T_1(r^*, \gamma) c_{c1}(r^*, \gamma) \quad (3.35)$$

c_{c1} [m/s]	=	First wave crest celerity from Eq. (3.32) (Figure 3-6)
L_1 [m]	=	Wavelength of the first wave (Figure 3-6a)
T_1 [s]	=	First wave period from Eq. (3.34) (Figure 3-6a)

Equations (3.12) and (3.22) to (3.35) were empirically derived from laboratory experiments. Therefore, the parameters must be kept within the limitations given in Table 3-3.

Table 3-3 Limitations to compute the 3D impulse wave generation and propagation.

Term	Range	Definition
Slide Froude number	$0.40 \leq F \leq 3.40$	$F = V_s/(gh)^{1/2}$
Relative slide thickness	$0.15 \leq S \leq 0.60$	$S = s/h$
Relative slide mass	$0.25 \leq M \leq 1.00$	$M = \rho_s V_s / (\rho_w b h^2)$
Relative slide density	$D = 1.338$	$D = \rho_s / \rho_w$
Relative granulate density	$\rho_g / \rho_w = 2.429$	ρ_g / ρ_w
Relative slide volume	$0.187 \leq V \leq 0.750$	$V = V_s / (b h^2)$
Slide impact angle	$30^\circ \leq \alpha \leq 90^\circ$	α
Relative slide width	$0.83 \leq B \leq 5.00$	$B = b/h$
Relative radial distance	$1 \leq r/h \leq 16$	r/h
Wave propagation angle	$-90^\circ \leq \gamma \leq 90^\circ$	γ
Impulse product parameter	$0.13 \leq P \leq 2.08$	$P = FS^{1/2} M^{1/4} \{\cos[(6/7)\alpha]\}^{1/2}$

The limitations for the computation of the 3D wave generation and propagation in Table 3-3 cover different parameter ranges than Table 3-2 for the 2D case; e.g. for 3D the impulse product parameter is within $0.13 \leq P \leq 2.08$, while it is within $0.17 \leq P \leq 8.13$ for 2D. Furthermore, the experiments underlying the 3D equations were conducted

with a single granulate density (Table 3-3), representing rock material. However, the adoption of \mathbf{P} allows for the consideration of different granular densities and Eqs. (3.22) to (3.35) may also be applied for a wider slide density range including snow or ice avalanches ($0.59 \leq D \leq 1.72$) for a preliminary hazard assessment.

3.3 Wave run-up and dam overtopping

3.3.1 Introduction

In contrast to wave generation, the equations for wave run-up and dam overtopping can be based only on 2D investigations. 3D effects such as dam curvature or asymmetrical wave impact angles can generally not be taken into account. They must be estimated in the Step 2 in Section 4.2 *after* the initial computation based on generally applicable equations is completed. In this regard, for the 2D run-up formula, it is irrelevant whether the wave parameters have been determined using the equations given in Subsections 3.2.4.2 or 3.2.4.3.

3.3.2 Governing parameters

Figure 3-7 shows a sketch defining the effects of impulse waves on dams, together with the relevant parameters. The following parameters have an influence in this procedure on the wave run-up or overtopping processes:

- Wave amplitude a near the dam
- Wave height H near the dam
- Still water depth h near the dam
- Run-up angle equal to dam face slope β
- Freeboard f
- Crest width b_K

The first two parameters a and H characterise the approaching impulse wave. They refer to the cross-section in front of the dam, where they are still not affected by the dam (Figure 3-7). These values are determined in Subsection 3.2.4. The still water depth h should be taken as that immediately upstream of the dam. The run-up angle β is measured from the horizontal (Figure 3-7). For the overtopping volume \mathcal{V} per unit length dam crest, as shown in Figure 3-7, the freeboard f and the crest width b_K are of relevance. The roughness of the dam slope is neglected. Experiments by Teng *et al.* (2000) showed reduced run-up heights on rough slopes for mild slope angles $\alpha < 20^\circ$. Therefore, predictions of wave run-up as well as dam overtopping with equations derived from laboratory experiments featuring smooth slopes are on the safe side.

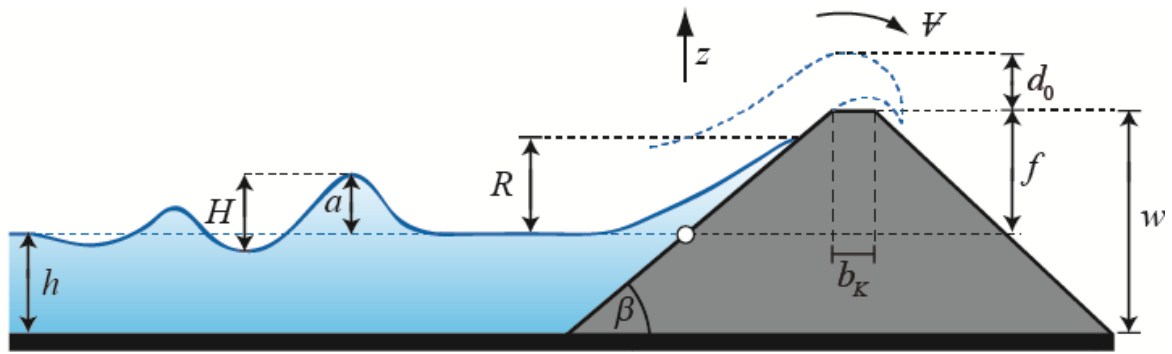


Figure 3-7 Sketch defining the parameters for the wave run-up and dam overtopping.

3.3.3 Wave run-up

The following equation is taken from Evers and Boes (2019) (Figure 3-1). The run-up height R can be determined by

$$R = 2a \exp(0.4\varepsilon) \left(\frac{90^\circ}{\beta} \right)^{0.2}. \quad (3.36)$$

a [m]	=	Wave crest amplitude (in front of the dam) (Figure 3-7)
h [m]	=	Still water depth (in front of the dam)
R [m]	=	Run-up height (Figure 3-7)
β [°]	=	Run-up angle equal to upstream dam face slope (Figure 3-7)
ε [-]	=	Relative wave crest amplitude; $\varepsilon = a/h$

Equation (3.36) is limited to non-breaking impulse wave run-up. For $\beta > 12^\circ$ and $\varepsilon < 0.78$, generally no wave breaking is expected during run-up. The value $\varepsilon = 0.78$ represents the maximum relative wave crest amplitude of a non-breaking solitary wave on a horizontal bottom. To predict whether an impulse wave is breaking or non-breaking during run-up for $10^\circ \leq \beta \leq 12^\circ$, the slope parameter S_o by Grilli *et al.* (1997) may be applied, which is defined as

$$S_o = 1.521 \frac{\tan \beta}{\sqrt{\varepsilon}}. \quad (3.37)$$

For $S_o > 0.37$, non-breaking wave run-up is expected (Grilli *et al.* 1997) and the application of Eq. (3.36) is valid. Wave breaking would involve higher uncertainty. However, the application of Eq. (3.36) can be regarded to be on the safe side, as wave breaking induces energy dissipation. Additional limitations on the use of Eq. (3.36) are shown in Table 3-4.

Table 3-4 Limitations for the computation of the wave run-up.

Term	Range	Term	Range
Relative wave crest amplitude	$0.007 \leq \varepsilon \leq 0.69$	Run-up angle	$10^\circ \leq \beta \leq 90^\circ$
Non-linearity	$0.57 \leq a/H \leq 1.04$	Slope parameter	$S_o \geq 0.37$

3.3.4 Wave overtopping at rigid dams

If the run-up height exceeds the available freeboard, i.e. $R > f$, water overtops the dam crest. Unforeseen discharge on the dam's airside may cause substantial damage to its structure and potentially lead to dam failure. Moreover, large overtopping volumes may create severe flooding downstream of the dam. The equations for the prediction of the overtopping process at rigid dams are taken from Kobel *et al.* (2017). The overtopping volume per unit length dam crest \mathcal{V} is determined with

$$\mathcal{V} = 1.35 \left(\frac{a}{H} \right)^{1.5} \left[\varepsilon \left(\frac{h}{w} \right)^{(2/\varepsilon)(\beta/90^\circ)^{0.25}} \left(\frac{a_w}{b_K} \right)^{0.12} \right]^{0.7} h^2. \quad (3.38)$$

a [m]	=	Wave crest amplitude (in front of the dam) (Figure 3-7)
a_w [m]	=	Effective wave crest amplitude; $a_w = h + a - w = a - f$
b_K [m]	=	Dam crest width (Figure 3-7)
f [m]	=	Freeboard
h [m]	=	Still water depth (in front of the dam)
H [m]	=	Wave height (in front of the dam) (Figure 3-7)
\mathcal{V} [m ³ /m]	=	Overtopping volume per unit dam crest length
w [m]	=	Dam height (Figure 3-7)
β [°]	=	Run-up angle equal to upstream dam face slope (Figure 3-7)
ε [-]	=	Relative wave crest amplitude; $\varepsilon = a/h$

Equation (3.38) includes the effective wave crest amplitude a_w , which needs to be positive by definition. Therefore, the overtopping volume may only be estimated for wave crest amplitude larger than the freeboard, i.e. $a > f$.

The maximum flow depth during wave overtopping on the water facing side of the dam crest (Figure 3-7) is relevant for estimating the required clearance above the dam crest (e.g. for bridges). The maximum wave overtopping flow depth d_0 is determined with

$$d_0 = 1.32 \left[\varepsilon \left(\frac{h}{w} \right)^{4[(\beta/90^\circ)^{-0.21} - \varepsilon]} \left(\frac{\beta}{90^\circ} \right)^{0.16} \right] w. \quad (3.39)$$

a [m]	=	Wave crest amplitude (in front of the dam) (Figure 3-7)
d_0 [m]	=	Maximum wave overtopping flow depth (Figure 3-7)
h [m]	=	Still water depth (in front of the dam)
w [m]	=	Dam height (Figure 3-7)
β [°]	=	Run-up angle equal to upstream dam face slope (Figure 3-7)
ε [-]	=	Relative wave crest amplitude; $\varepsilon = a/h$

In addition to Ψ , the discharge per unit dam crest length is also important. The determination of the discharge requires the wave overtopping duration given by

$$t_o = \frac{1}{0.15} \left[\varepsilon^{0.2} \left(\frac{h}{w} \right)^{(-0.9/\varepsilon)(\beta/90^\circ)^{0.4}} \right]^{-1.9} (w/g)^{0.5}. \quad (3.40)$$

a [m]	=	Wave crest amplitude (in front of the dam) (Figure 3-7)
g [m/s ²]	=	Gravitational acceleration; $g = 9.81$ m/s ²
h [m]	=	Still water depth (in front of the dam)
t_o [s]	=	Wave overtopping duration
w [m]	=	Dam height (Figure 3-7)
β [°]	=	Run-up angle equal to upstream dam face slope (Figure 3-7)
ε [-]	=	Relative wave crest amplitude; $\varepsilon = a/h$

The average discharge per unit dam crest length q_m on the dam crest is then determined from

$$q_m = \Psi/t_o. \quad (3.41)$$

q_m [m ² /s]	=	Average unit discharge
t_o [s]	=	Wave overtopping duration (Eq. 3.40)
Ψ [m ³ /m]	=	Overtopping volume (Eq. 3.38)

The maximum discharge q_{0M} per unit dam crest length is also important. The data of Müller (1995) indicate the relation $q_{0M} \approx 2q_{0m}$ between the average and the maximum discharge if no freeboard is available, i.e. $f = 0$. This estimate may also be transferred to cases featuring a small freeboard compared to the still water depth, i.e. $f \ll h$.

Equations (3.38) to (3.40) were derived from experiments with solitary waves ($a/H = 1$), characterised by a large horizontal mass transport (Section 2.2). Therefore, this wave type represents an extreme case. Equation (3.38) was generalised by Kobel *et al.* (2017) with the data by Müller (1995) to include also waves with a subsequent wave trough, i.e. $a/H < 1$. Limitations on the use of Eqs. (3.38) to (3.40) are shown in Table 3-5.

Table 3-5 Limitations to compute the wave overtopping at rigid dams.

Term	Range	Term	Range
Relative wave crest amplitude	$0.013 \leq \varepsilon \leq 0.700$	Dam angle	$18.4^\circ \leq \beta \leq 90^\circ$
Relative effective wave amplitude	$0.02 \leq a_w/b_K \leq 130$	Non-linearity	$0.63 \leq a/H \leq 1.00$
Relative still water depth	$0.67 \leq h/w \leq 1.00$	Relative crest width	$0.07 \leq b_K/w \leq 0.53$

3.4 Overland flow

3.4.1 Introduction

If the topography after the run-up shore is horizontal, overland flow can be generated. While for plain wave run-up only the maximum run-up height is considered as the assessment parameter, the inundation depth and flow velocity are important for overland flow. Evacuation plans are primarily based on the flow front propagation, i.e. the duration of the flow front to reach a given location. The subsequent hazard assessment step is based on local flow depths and flow velocities to determine forces on infrastructure. The following overland flow equations are based on experiments with solitary waves by Fuchs (2013) and Fuchs and Hager (2015). The first incoming wave crest can be considered as a solitary wave, although the generated wave pattern may be more complex and additional wave-wave interaction between the reflected primary wave and the incoming secondary wave will be observed.

3.4.2 Governing parameters

Overland flow features strongly depend on (Figure 3-8):

- Relative wave height $\varepsilon = a/h$
- Run-up angle β
- Freeboard $f = w - h$

A larger relative wave height generally increases the resulting overland flow. For a mild run-up angle, the incoming wave is gradually transformed into overland flow such that a small flow depth and a high flow velocity are already observed at the transition point x_{tr} . In contrast, for a steeper run-up angle the flow depth at the transition point is large and the corresponding flow velocity is small. If the freeboard f is large, the wave-shore interaction is similar to the plane wave run-up case. In contrast, for small values of f , a major portion of the incoming wave energy is transmitted to the connecting horizontal plane such that even small waves lead to overland flow.

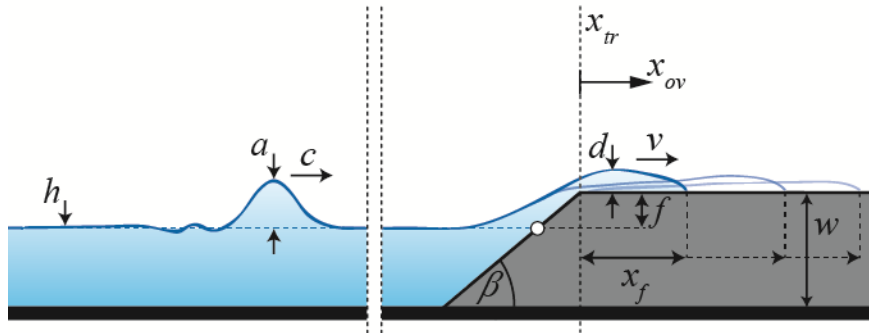


Figure 3-8 Sketch defining the parameters for the overland flow.

The minimum relative wave amplitude required to induce overland flow is

$$\varepsilon_{min} = \frac{f (\tan \beta)^{0.05}}{3h} . \quad (3.42)$$

a [m]	=	Wave amplitude (in front of the shore) (Figure 3-8)
f [m]	=	Freeboard (Figure 3-8)
h [m]	=	Still water depth (in front of the shore) (Figure 3-8)
β [°]	=	Run-up angle (Figure 3-8)
ε_{min} [-]	=	Minimum relative wave amplitude to induce overland flow

By subtracting ε_{min} from the incoming relative wave amplitude, the wave portion effectively determining the overland flow characteristics (subscript *eff*) is

$$\varepsilon_{eff} = \varepsilon - \varepsilon_{min} . \quad (3.43)$$

ε [-]	=	Relative wave amplitude; $\varepsilon = a/h$ (Figure 3-8)
ε_{eff} [-]	=	Effective relative wave amplitude
ε_{min} [-]	=	Minimum relative wave amplitude to induce overland flow (Eq. 3.42)

The limitations for the overland flow computations are specified in Table 3-6.

Table 3-6 Limitations to compute the overland flow.

Term	Range	Term	Range
Relative wave amplitude	$0.1 \leq \varepsilon \leq 0.7$	Relative freeboard	$0.04 \leq f/h \leq 0.56$
Run-up angle	$11^\circ \leq \beta \leq 34^\circ$	Relative overland flow distance	$0 \leq x_{ov}/w \leq 10$

3.4.3 Overland flow front propagation

If the relative freeboard f/h is large, then the incoming wave is first transformed into a shore slope-parallel run-up flow before the run-up tongue reaches the transition point where it transforms into a horizontal overland flow. Therefore, a part of the incoming wave energy is reflected or dissipated during the run-up process and does not contribute to the overland flow. For small f/h , however, the incoming wave is nearly fully transmitted into the overland flow. The wave is then compressed at the shore and overland flow is subsequently accelerated by the transformation of potential to kinetic energy. The overland flow propagation is generally faster for gentle slopes since the overland flow characteristics are then already fully established at the transition point, in contrast to steeper slopes ($\beta \approx 34^\circ$). The flow front position x_f is represented as a function of the relative time $T_r = t(c/a)$ by

$$x_f = \left(1.7 \frac{f}{h} + 0.5 \right) \left[\frac{T_r \varepsilon^{\frac{f}{h} + 1.45}}{(\tan \beta)^{0.25}} \right]^{1.35 - 1.15 \frac{f}{h}} w. \quad (3.44)$$

a [m]	=	Wave amplitude (in front of the shore) (Figure 3-8)
c [m/s]	=	Wave celerity (Eq. 3.17) (Figure 3-8)
f [m]	=	Freeboard (Figure 3-8)
h [m]	=	Still water depth (in front of the shore) (Figure 3-8)
T_r [-]	=	Relative time; $T_r = t(c/a)$
w [m]	=	Shore height (Figure 3-8)
x_f [m]	=	Flow front position (Figure 3-8)
β [°]	=	Run-up angle (Figure 3-8)
ε [-]	=	Relative wave height; $\varepsilon = a/h$ (Figure 3-8)

3.4.4 Overland flow depth

First, the maximum flow depth at the transition point $d_0 = d_{max}(x_{ov} = 0)$ is determined based on the incident parameters. For a small relative freeboard of $f/h = 0.04$, the maximum flow depth can be larger than the incident wave amplitude. As described above, a steep run-up angle of $\beta = 34^\circ$ leads to a more abrupt wave reflection and thus to larger flow depths at x_{tr} , as compared with a mild angle of $\beta = 11^\circ$. This slope effect is prominent for large incident wave amplitudes, whereas the differences remain small for small a . The effect of the shore slope also increases with increasing freeboard. The maximum flow depth d_0 at x_{tr} is found with

$$d_0 = \frac{(0.4 \tan \beta + 0.9) \varepsilon_{eff}}{(w/h)^{0.45 \cot \beta}} h. \quad (3.45)$$

d_0 [m]	=	Maximum flow depth at x_{tr} (Figure 3-8)
h [m]	=	Still water depth (in front of the shore) (Figure 3-8)
w [m]	=	Shore height (Figure 3-8)
β [°]	=	Run-up angle (Figure 3-8)
ε_{eff} [-]	=	Effective relative wave height (Eq. 3.43)

In a second step, the maximum flow depths on the overland flow portion $d_{max}(x_{ov})$ are evaluated based on d_0 . The maximum flow depth along the shore rapidly reduces within a short propagation distance. For example, at a relative overland flow position $x_{max}^* = 5$, only $\approx 23\%$ of the initial flow depth d_0 remains. The maximum flow depth d_{max} at a given x_{max}^* is

$$d_{max} = d_0 \left\{ 1 - \tanh \left[0.54 \left(x_{max}^* \right)^{0.39} \right] \right\} \quad (3.46)$$

with

$$x_{max}^* = \frac{x_{ov}}{w} \left(\frac{w}{h} \right)^{5.3 \tan \beta - 1.4}. \quad (3.47)$$

d_0 [m]	=	Maximum flow depth at x_{tr} (Eq. 3.45) (Figure 3-8)
d_{max} [m]	=	Maximum flow depth at x_{ov}
h [m]	=	Still water depth (in front of the shore) (Figure 3-8)
w [m]	=	Shore height (Figure 3-8)
x_{max}^* [-]	=	Relative overland flow position
x_{ov} [m]	=	Streamwise overland flow coordinate (Figure 3-8)
x_{tr} [-]	=	Transition point (Figure 3-8)
β [°]	=	Run-up angle (Figure 3-8)

3.4.5 Overland flow velocity

Overland flow velocities are generally larger for larger incoming waves. For a large relative freeboard ($f/h = 0.56$) the flow velocities considerably reduce, as compared with the flow on a shore of smaller freeboard. The flow then has to adapt to two consecutive changes of flow directions before reaching the horizontal portion at $x_{ov} > 0$. A part of the incoming wave energy is dissipated or reflected and does not contribute to the overland flow. In addition, flow velocities are strongly affected by the shore slope. For a steep slope with $\beta = 34^\circ$, the flow characteristics at x_{tr} are determined by the incoming wave

particle motion in contrast to the well-established overland flow features generated on gentler slopes with $\beta = 11^\circ$ to 22° . The maximum depth-averaged horizontal flow velocity at x_{tr} is represented by a hyperbolic tangent function (tanh) as

$$\tilde{v}_{x,max} = 5c \tanh \left[0.017 \varepsilon_{eff} \left(\frac{w}{h} \right)^{3 \tan \beta + 2.5} (\cot \beta)^{0.5} \right]^{0.5}. \quad (3.48)$$

c [m/s]	=	Wave celerity (Eq. 3.17) (Figure 3-8)
h [m]	=	Still water depth (in front of the shore) (Figure 3-8)
$\tilde{v}_{x,max}$ [m/s]	=	Maximum depth-averaged horizontal flow velocity at x_{tr}
w [m]	=	Shore height (Figure 3-8)
x_{tr} [-]	=	Transition point (Figure 3-8)
β [°]	=	Run-up angle (Figure 3-8)
ε_{eff} [-]	=	Effective relative wave height (Eq. 3.43)

For larger distances x_{ov} , the overland flow is fully established with the maximum flow velocities located at the flow front. Similar to the maximum flow velocities at x_{tr} , flow front velocities v_f are larger for a larger incoming wave height. The shore slope effect is mainly concentrated at the transition point x_{tr} . While the flow is strongly accelerated for the steep slope $\beta = 34^\circ$, the front velocity remains almost constant during propagation for $\beta = 11^\circ$. For larger x_{ov} the shore slope has only a minor effect on v_f with generally larger flow velocities for mild slopes.

Values of the front velocity at $x_{ov}/w = 5$ were observed to represent the maximum front velocity during overland flow propagation. For $x_{ov}/w = 1$ to 5, the potential energy converted to kinetic energy may accelerate the flow, at least for a steep shore slope. For $x_{ov}/w = 5$ to 9, the energy dissipation due to turbulence and viscous effects dominates, leading to reduced flow front velocities. Therefore, the values $v_{f,max} = v_f(x_{ov}/w = 5)$ are considered as the maximum onshore flow velocities for all parameter configurations. The maximum flow front velocity is

$$v_{f,max} = 1.6c \tanh \left[2.2 \left(\varepsilon_{eff} \frac{h}{w} \right)^{0.75} \right]. \quad (3.49)$$

c [m/s]	=	Wave celerity (Eq. 3.17) (Figure 3-8)
h [m]	=	Still water depth (in front of the shore) (Figure 3-8)
$v_{f,max}$ [m/s]	=	Maximum flow front velocity at $x_{ov}/w = 5$
w [m]	=	Shore height (Figure 3-8)
x_{ov} [m]	=	Streamwise overland flow coordinate (Figure 3-8)
ε_{eff} [-]	=	Effective relative wave amplitude (Eq. 3.43)

The maximum 'far field' flow front velocity is almost independent of the shore slope. Maximum values of the front velocity are $v_f \approx 1.6c$ for large relative wave amplitudes ε and a small relative freeboard f/h corresponding to a small relative shore height $w/h = f/h + 1$. The maximum front velocity is therefore about 1/3 higher than the maximum particle velocities at the transition point x_{tr} (Eq. 3.48).

The wave-induced overland flow discharge per unit width at x_{tr} corresponds to the horizontal particle velocity v_x integrated over the flow depth d as

$$q = \int_{z=0}^{z=d} v_x dz . \quad (3.50)$$

The observed discharge characteristics are similar to unsteady flow, supporting the analogy to dam break or surge flow with a larger flow velocity and correspondingly smaller flow depth at the ascending stage, as compared to the descending stage. The maximum discharge at the transition point $q_0 = q_{max}(x_{ov} = 0)$ increases with larger ε and smaller f/h without a distinct shore slope effect. The maximum specific discharge is represented by the hyperbolic tangent function

$$q_0 = 0.83ca \tanh \left[\frac{\varepsilon_{eff}}{\left(\frac{w}{h}\right)^{1.5 \cot \beta} (\cot \beta)^{0.5}} \right]^{0.5} . \quad (3.51)$$

a [m]	=	Wave amplitude (Figure 3-8)
c [m/s]	=	Wave celerity (Eq. 3.17) (Figure 3-8)
h [m]	=	Still water depth (in front of the shore) (Figure 3-8)
q_0 [m ² /s]	=	Maximum specific discharge at x_{tr}
w [m]	=	Shore height (Figure 3-8)
x_{tr} [-]	=	Transition point (Figure 3-8)
β [°]	=	Run-up angle (Figure 3-8)
ε_{eff} [-]	=	Effective relative wave amplitude (Eq. 3.43)

For large wave heights and small freeboards, the unit discharge in Eq. (3.51) approaches 83% of the maximum mass flux within the solitary wave $\tilde{v}_x (h + a) = ca$.

3.5 Wave force on dams

3.5.1 Introduction

This section covers the impulse wave force acting on dams. The prediction of this force is subject to great uncertainty; even if the forces of identical waves are measured in model tests, there can be considerable scatter of the results. Walkden (1999) generated 330 identical waves but found that their maximum force on bank protection varied by up to +100% and -50% from the mean value. The variation may be smaller for forces acting on a flat surface, e.g. the face of a dam. Marzeddu *et al.* (2017) repeated experiments with nearly breaking waves impacting a vertical wall 120 times and found the maximum measured total force at 168% of the minimum force and at 133% of the mode value, i.e. the most frequent value. The following computations are based on an estimation of the run-up height R such that the computation of R with Eq. (3.36) is not necessary. However, they do require the wave amplitude a given in Subsection 3.2.4.

Subsection 3.5.2 considers the effects resulting from the still water pressure. Impulse waves can have different profiles and hence properties (Heller and Hager 2011). Among these wave types, the solitary-like waves represent the extreme case, as these are characterised by a large horizontal mass transport and a high wave celerity (Section 2.2). To make a conservative estimate of the force acting on a dam, this wave type is therefore considered as the upper limiting case for all wave types in the following. In Subsection 3.5.3, the total horizontal force due to wave run-up as well as wave overtopping are determined based on Ramsden (1996). Assuming a dam is designed to withstand hydrostatic pressure of the maximum reservoir level h plus the freeboard f , e.g. for wave and wind surges, the case of impulse wave run-up without overtopping ($f \geq R$) is not expected to exert any critical force on the structure. Nonetheless, the computation of the wave force without overtopping is a prerequisite for assessing the resulting overtopping wave force. Analogous to an overfall weir, the wave force due to overtopping is subsequently determined. When considering the force on dams, it must be noted that this is the maximum wave force which often acts in the prototype for only a few seconds.

3.5.2 Hydrostatic pressure

Figure 3-9(a) shows a reservoir with a still water depth h impounded by a dam with vertical upstream face. The resulting hydrostatic pressure distribution is shown in Figure 3-9(b). The maximum water pressure $\rho_w g h$ acts on the foundation, the horizontal force component $F_{RW,h}$ acts $h/3$ above the foundation level (e.g. Schröder and Saenger 2002).

The horizontal force component $F_{RW,h}$ per unit length dam crest resulting only from the hydrostatic pressure, can be computed as

$$F_{RW,h} = \rho_w g h^2 / 2. \quad (3.52)$$

g [m/s ²]	=	Gravitational acceleration; $g = 9.81$ m/s ²
h [m]	=	Still water depth (in front of the dam)
$F_{RW,h}$ [N/m]	=	Horizontal force component per unit dam crest length resulting only from hydrostatic pressure
ρ_w [kg/m ³]	=	Water density

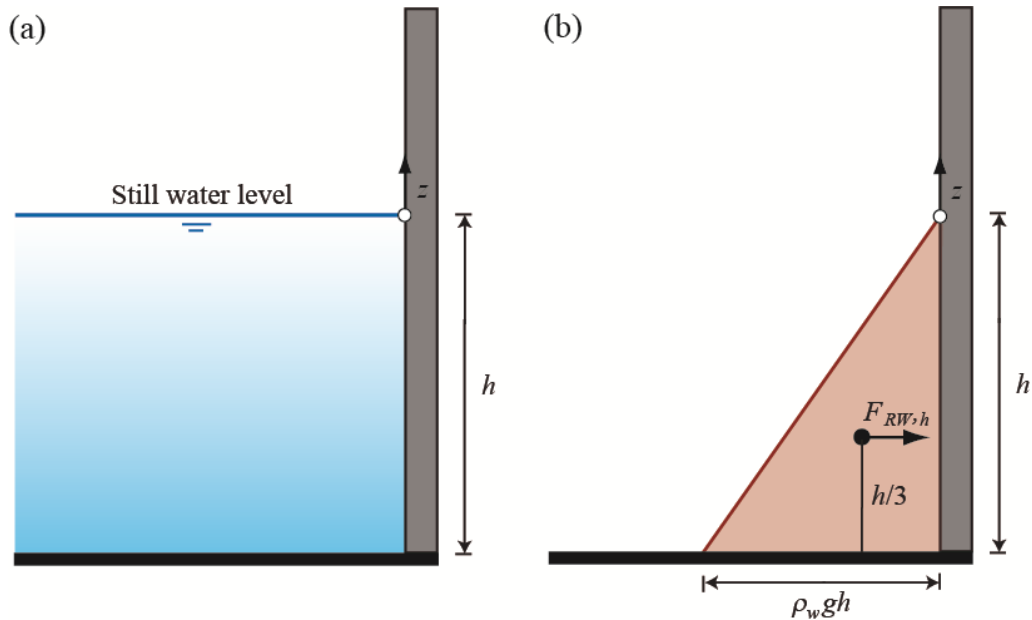


Figure 3-9 Effect of impounded volume on a dam with vertical upstream face: (a) still water surface for still water depth h and (b) hydrostatic pressure distribution with horizontal force component $F_{RW,h}$ per unit dam crest length and elevation $h/3$ of the resultant of $F_{RW,h}$.

If the upstream dam face is inclined at angle β , the water load results in a vertical force component, in addition to the horizontal force component (Figure 3-10). This vertical force component is of importance, e.g. for the determination of the safety of a dam against sliding in a total stress analysis. The horizontal still water pressure is not affected by the dam face slope β and can be computed for $\beta < 90^\circ$ using Eq. (3.52). The vertical force component $F_{RW,v}$ per unit dam crest length is given, according to Figure 3-10, by

$$F_{RW,v} = \rho_w g h^2 / (2 \tan \beta) = F_{RW,h} / \tan \beta. \quad (3.53)$$

$F_{RW,h}$ [N/m]	=	Horizontal force component per unit dam crest length resulting only from hydrostatic pressure
$F_{RW,v}$ [N/m]	=	Vertical force component per unit dam crest length resulting only from hydrostatic pressure
g [m/s ²]	=	Gravitational acceleration; $g = 9.81$ m/s ²
h [m]	=	Still water depth (in front of the dam)
β [°]	=	Dam face slope (Figure 3-10)
ρ_w [kg/m ³]	=	Water density

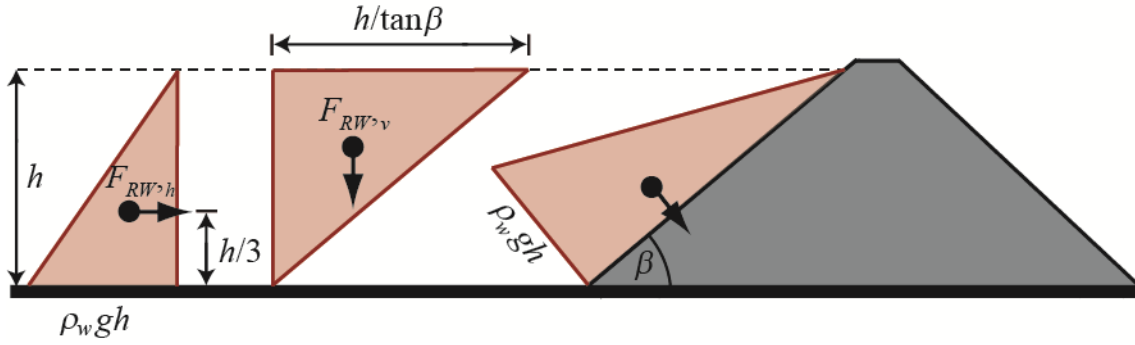


Figure 3-10 Pressure distribution for a still water depth h impounded by an inclined dam face: on the left the horizontal force component, in the centre the vertical force component and on the right the total force is illustrated (after Schröder and Saenger 2002).

3.5.3 Wave run-up and overtopping

As shown in Figure 3-11(a), the pressure distribution of a solitary-like wave is approximately triangular. For the assessment of the force effect, the run-up height R is considered to be independent of the values computed in Eq. (3.36), and is assumed equal to $2a$. Equation (3.54) for the determination of the total horizontal force component $F_{tot,h}$ per unit dam crest length resulting from an impulse wave and hydrostatic pressure is based on the measured values of Ramsden (1996). The component $F_{tot,h}$ is a function of the relative wave amplitude a/h (Heller *et al.* 2009) and may be approximated by

$$F_{tot,h} = [1 - 1.5(a/h)]^{1/6} F_{hs,h} \quad \text{for } 0 \leq a/h \leq 0.6. \quad (3.54)$$

a [m]	=	Wave amplitude (in front of the dam) (Figure 3-7)
$F_{hs,h}$ [N/m]	=	Horizontal component of hydrostatic force per unit dam crest length resulting from a still water level displaced upwards by $2a$, according to Ramsden (1996)
$F_{tot,h}$ [N/m]	=	Total horizontal force component per unit dam crest length resulting from an impulse wave and hydrostatic pressure
h [m]	=	Still water depth (in front of the dam)

The wave amplitude a can be determined for the 2D case from the wave height H as $a = (4/5)H$ (Eq. 3.16). For the 3D case, a may be computed directly with Eqs. (3.29) and (3.31). In Eq. (3.55), the horizontal component of the hydrostatic force $F_{hs,h}$ resulting from a still water level displaced upwards by $2a$, is applied. Ramsden (1996) made use of this parameter $F_{hs,h}$ to calibrate the measurement points. It is given by

$$F_{hs,h} = \rho_w g (2a + h)^2 / 2. \quad (3.55)$$

a [m]	=	Wave amplitude (in front of the dam) (Figure 3-7)
$F_{hs,h}$ [N/m]	=	Horizontal component of hydrostatic force per unit dam crest length resulting from a still water level displaced upwards by $2a$, according to Ramsden (1996)
g [m/s ²]	=	Gravitational acceleration; $g = 9.81$ m/s ²
h [m]	=	Still water depth (in front of the dam)
ρ_w [kg/m ³]	=	Water density

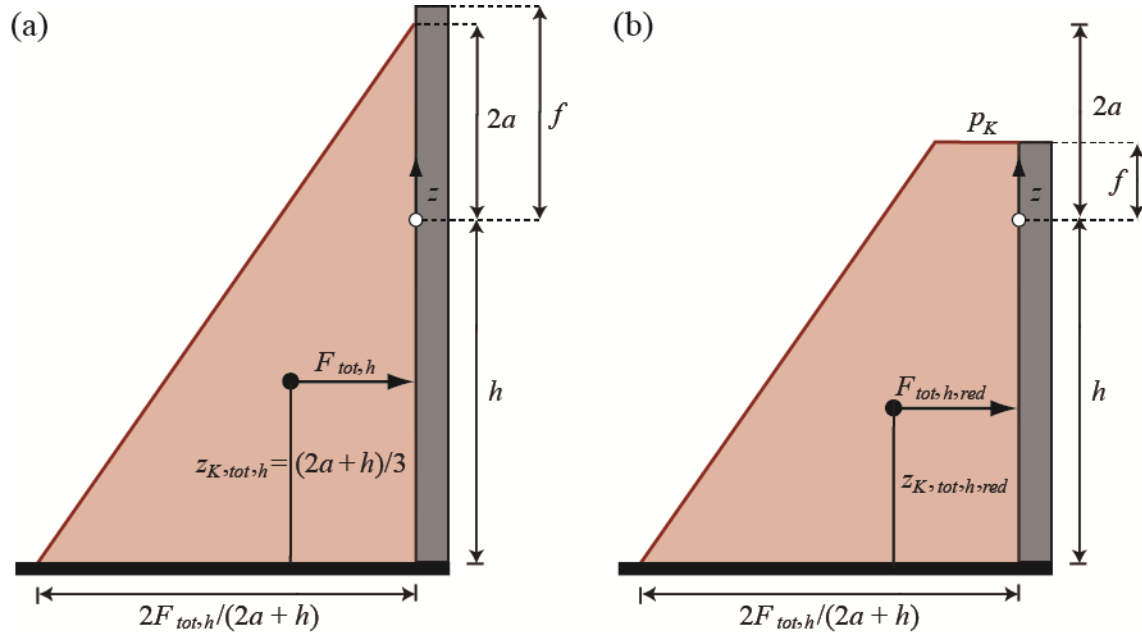


Figure 3-11 Pressure distribution on the vertical dam face as a result of a solitary-like wave with a maximum value of $2F_{tot,h}/(2a+h)$ for the cases of (a) $f \geq 2a$ and (b) reduced pressure effects if $f < 2a$.

The elevation $z_{K,tot,h}$ of the resultant of $F_{tot,h}$ is located $(2a+h)/3$ above the dam foundation (Figure 3-11a).

Should the wave overtop the dam crest, i.e. if the freeboard is less than twice the wave amplitude $f < 2a$, the force effect is reduced as shown in Figure 3-11(b). The pressure at the dam crest p_K is determined in proportion as

$$p_K = \frac{2F_{tot,h}}{(2a+h)^2}(2a-f) \quad \text{for } f < 2a. \quad (3.56)$$

a [m]	=	Wave amplitude (in front of the dam) (Figure 3-7)
f [m]	=	Freeboard (Figure 3-7)
$F_{tot,h}$ [N/m]	=	Total horizontal force component per unit dam crest length resulting from an impulse wave and hydrostatic pressure (Eq. 3.54)
h [m]	=	Still water depth (in front of the dam)
p_K [N/m ²]	=	Pressure at dam crest (Figure 3-11b)

With Eq. (3.54), the reduced total horizontal force component per unit dam crest length $F_{tot,h,red}$ resulting from an impulse wave and hydrostatic pressure for $f < 2a$ may be generally formulated as

$$F_{tot,h,red} = \frac{(h+f)}{2} \left[p_K + \frac{2F_{tot,h}}{2a+h} \right] \quad \text{for } f < 2a. \quad (3.57)$$

a [m]	=	Wave amplitude (in front of the dam) (Figure 3-7)
f [m]	=	Freeboard (Figure 3-7)
$F_{tot,h}$ [N/m]	=	Total horizontal force component per unit dam crest length resulting from an impulse wave and hydrostatic pressure (Eq. 3.54)
$F_{tot,h,red}$ [N/m]	=	Reduced total horizontal force component per unit dam crest length resulting from an impulse wave and hydrostatic pressure (Eq. 3.57)
h [m]	=	Still water depth (in front of the dam)
p_K [N/m ²]	=	Pressure at dam crest (Figure 3-11b)

The elevation $z_{K,tot,h,red}$ of the resultant of the reduced total horizontal force component $F_{tot,h,red}$ is shown in Figure 3-11(b) and may be expressed as

$$z_{K,tot,h,red} = \frac{\left[2F_{tot,h} / (2a+h) - p_K \right] \frac{(h+f)^2}{6} + p_K \frac{(h+f)^2}{2}}{\left[2F_{tot,h} / (2a+h) - p_K \right] \frac{h+f}{2} + p_K (h+f)}. \quad (3.58)$$

a [m]	=	Wave amplitude (in front of the dam) (Figure 3-7)
f [m]	=	Freeboard (Figure 3-7)
$F_{tot,h}$ [N/m]	=	Total horizontal force component per unit dam crest length resulting from an impulse wave and hydrostatic pressure (Eq. 3.54)
$F_{tot,h,red}$ [N/m]	=	Reduced total horizontal force component per unit dam crest length resulting from an impulse wave and hydrostatic pressure (Eq. 3.57)
h [m]	=	Still water depth (in front of the dam)
p_K [N/m ²]	=	Pressure at dam crest (Figure 3-11b)
$z_{K,tot,h,red}$ [m]	=	Elevation of the resultant of $F_{tot,h,red}$

The effect of the hydrostatic pressure in accordance with Eq. (3.52) is already taken into account in the computational procedure in Subsection 3.5.3. The horizontal force effect remains independent of the dam face slope β . For $\beta < 90^\circ$, an additional vertical force component exists (Figure 3-10), equal to the force determined in Eq. (3.54) or Eq.

(3.57), respectively, divided by $\tan\beta$ (Subsection 3.5.2). For the sake of simplification, the total force effect is thereby considered to approximate static conditions. According to Heller and Hager (2011), in extreme cases featuring large wave amplitudes and small water depths, bore-like waves can also develop in 2D, for

$$S^{1/3} M \cos \alpha_{eff} > 11F^{-5/2}. \quad (3.59)$$

b [m]	=	Slide width
F [-]	=	Slide Froude number; $F = V_s / (gh)^{1/2}$
g [m/s ²]	=	Gravitational acceleration; $g = 9.81$ m/s ²
h [m]	=	Still water depth (in the slide impact zone)
M [-]	=	Relative slide mass; $M = \rho_s V_s / (\rho_w b h^2)$
s [m]	=	Slide thickness (Figure 3-3a)
S [-]	=	Relative slide thickness; $S = s/h$
V_s [m/s]	=	Slide impact velocity (Figure 3-3a)
V_s [m ³]	=	Bulk slide volume (Figure 3-3a)
α [°]	=	Slide impact angle (Figure 3-3a)
α_{eff} [°]	=	Effective slide impact angle; $\alpha_{eff} = (6/7)\alpha$
ρ_s [kg/m ³]	=	Bulk slide density (Figure 3-3a)
ρ_w [kg/m ³]	=	Water density

If bore-like waves are created close to the slide impact zone, they transform over a short distance into cnoidal or solitary-like waves, particularly in 3D (Section 2.2). Initially bore-like waves may therefore also be analysed by this method, if the slide impact location is not too close to the dam structure.

3.6 Final comments

The computational procedure presented in accordance with Figure 3-1 is based on generally applicable equations established from model tests in a prismatic wave channel or in a rectangular wave basin. Deviations from these ideal shapes may lead to model effects (Subsection 3.2.1). It is absolutely essential to estimate the effects which are neglected in the generally applicable equations, such as the reservoir geometry and the mass movement type. In the computational procedure shown in Figure 3-1, this is explained in Step 2. These effects are described in Chapter 4. They also have to be considered when applying the computational tool (Section 5.5).

4 Step 2, sensitivity analysis and safety allowance

4.1 Introduction

Sections 4.2 to 4.5 cover Step 2 of the computational procedure shown in Figure 3-1 for the analysis of landslide-generated impulse waves. The influences explained here may lead to significant changes in the wave parameters and thus the run-up heights, as compared with these determined in Step 1. Step 2 should also account for the effects of exceeding the limitations for the computation of impulse waves, in accordance with Tables 3-2 to 3-6. Large deviations from the values calculated in Step 1, as a result of breaching the limitations in question, are generally not expected, but they do increase the level of uncertainty of the results.

In addition to the momentum transmission, there will be a displacement mechanism if the slide volume is large in relation to the stored water volume in the reservoir. An approximation of the resulting increase of the reservoir level can be made by dividing the slide volume by the surface area of the reservoir (e.g. Subsection 5.1.3).

The equations in Chapter 3 are based on a prismatic channel (2D), or a rectangular wave basin (3D), in each case with a horizontal bed. The influence, which a reservoir shape varying from these ideal forms has on the wave parameters, is discussed in Section 4.2. In addition, an approach for approximating wave heights and amplitudes in geometries neither clearly 2D or 3D based on the water body side angle θ is provided. Section 4.3 addresses edge waves, which are impulse waves propagating along the same slope as the landslide moves in the 3D water body. The underlying physics of these edge waves is somehow different from the offshore propagating waves covered in Step 1. The equations in Chapter 3 are based on movement of a granular slide, but mass movement can also comprise of a solid body. The various *mass movement types* are discussed in Section 4.4. Then the difference between the maximum wave amplitude generated by a solid body, compared with that created by granular slide, is addressed. Section 4.5 accounts for the run-out distance of underwater landslide deposits, as these might interfere with submerged reservoir infrastructure including e.g. bottom outlets. In Section 4.6, a *sensitivity analysis* of the run-up height R , as a function of the governing parameters, is described. Finally, some comments are made in Section 4.7 on the accuracy of the results and on *safety allowances*.

4.2 Effects of the reservoir shape

This Section considers the effects of the reservoir geometry for situations where the geometry deviates from the two extreme cases of (a) confined uni-directional (2D) and (b) completely free, radial (3D) propagation of the generated waves (Figure 3-2). These effects are presented here in order that their influence on wave height, and thus on the run-

up height, can be assessed in Step 2 (Figure 3-1). The shape of the reservoir has a significant effect on the propagation of impulse waves (Camfield 1980, Heller and Spinneken 2015, Ruffini *et al.* 2019), particularly for large water bodies. As the still water depth h decreases, a deep-water wave ($L/h < 2$) at first changes to an intermediate-water wave ($2 < L/h < 20$) before becoming a shallow-water wave ($L/h > 20$), i.e. the wave is then influenced by the bed. The contact with the bed normally results in an increase of the wave height, as the friction losses of the bed may be neglected compared with shoaling. A shallow-water wave will be influenced not only by shoaling but also by refraction. Irrespective of whether it is classed as a shallow, intermediate or deep-water wave, any wave will be subject to diffraction, constriction and reflection (Coastal Engineering Manual USACE 2006). These effects are described as follows:

- a) Refraction (Figure 4-1a): a shallow-water wave changes direction such that it moves mostly perpendicularly onto the shore.

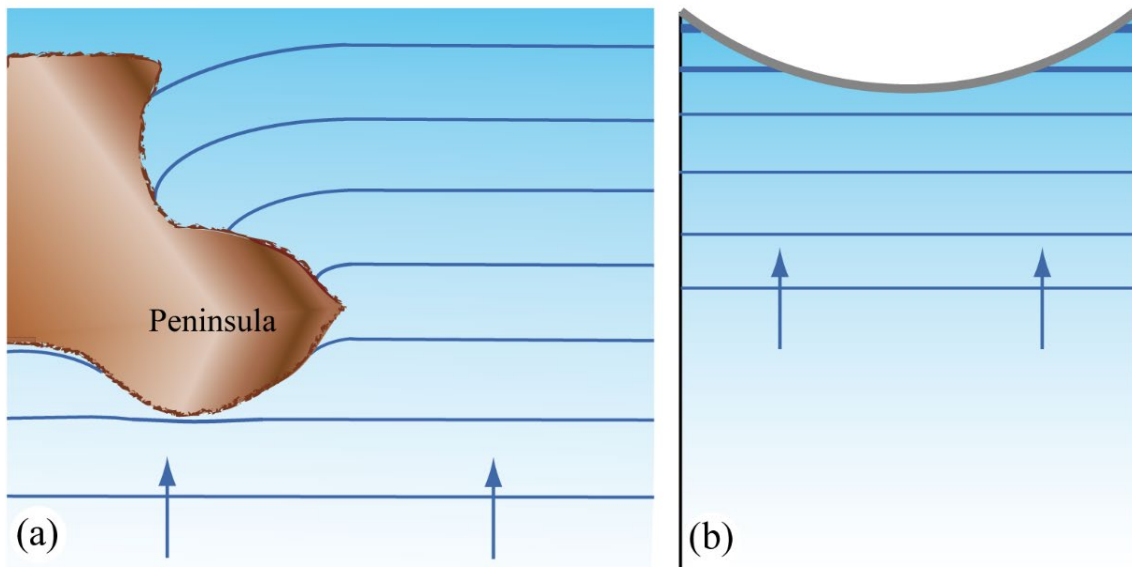


Figure 4-1 (a) Principles of refraction near a shore and diffraction around a peninsula and (b) wave height increase resulting from constrictions near the flanks of an arch dam.

- b) Shoaling (Figure 4-2b): the height of a shallow-water wave increases whilst, at the same time, the wave length decreases. The increase in wave height due to shoaling may be determined according to Dean and Dalrymple (2004) as

$$\frac{H_2}{H_1} = \left(\frac{h_1}{h_2} \right)^{1/4} \left(\frac{b_1}{b_2} \right)^{1/2} \quad (4.1)$$

b_1 [m]	=	Reservoir width at cross-section 1 of Figure 4-2(b)
b_2 [m]	=	Reservoir width at cross-section 2 of Figure 4-2(b)
h_1 [m]	=	Still water depth at cross-section 1 of Figure 4-2(b)
h_2 [m]	=	Still water depth at cross-section 2 of Figure 4-2(b)

H_1 [m]	=	Wave height at cross-section 1 of Figure 4-2(b)
H_2 [m]	=	Wave height at cross-section 2 of Figure 4-2(b)

Equation (4.1) is based on the assumption of a constant energy flux between cross-sections 1 and 2, as shown in Figure 4-2(b). If the widths between cross-sections 1 and 2 are constant, $b_1 = b_2$, then Eq. (4.1) can be reduced to $H_2/H_1 = (h_1/h_2)^{1/4}$, known as Green's law. For situations where the width is not constant between two cross-sections, the water body geometry affects wave propagation, which is discussed in Section 4.2.1 in more detail.

- c) Diffraction (Figure 4-1a): a wave passes around an obstacle and gives up some of its energy laterally into the area of the obstacle shadow.
- d) Constriction (Figure 4-1b): a wave in a constricted area of a reservoir will increase in height, due to the concentration of wave energy. This can occur, for instance, at the flank of a dam. For shallow-water waves, the estimation is again possible using Eq. (4.1) and for deep-water waves Eq. (4.1) can be simplified to $H_2/H_1 = (b_1/b_2)^{1/2}$ because $h_2 \approx h_1$. The effects of constrictions at dam flanks will be quantified in Section 4.2.2.
- e) Reflection (Figure 4-2a): on reaching the shore, a wave is reflected and moves back with reduced height. The height of the reflected wave depends on how much of the wave energy is dissipated during run-up. The energy dissipation during run-up at dams with vertical faces, where wave overtopping cannot take place, is almost negligible resulting in total reflection. The height and amplitude of the reflected wave are then practically the same as for the incident wave $a \approx a_R$. When a reflected wave meets an incident wave, non-linear superposition occurs at the meeting point, provided neither of the waves has broken. The individual waves move amongst each other and their profiles, after the waves have crossed, are practically uninfluenced by their encounter (Figure 4-3).

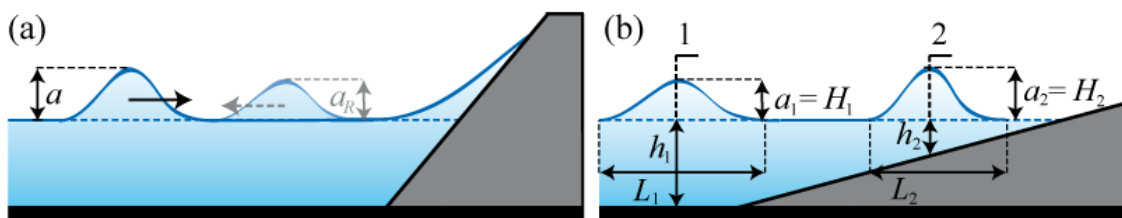


Figure 4-2 Principle sketches from (a) reflection of a solitary wave by the face of a dam with $a > a_R$ and (b) shoaling of a solitary wave close to the shore with $a_1 < a_2$ and $L_1 > L_2$.

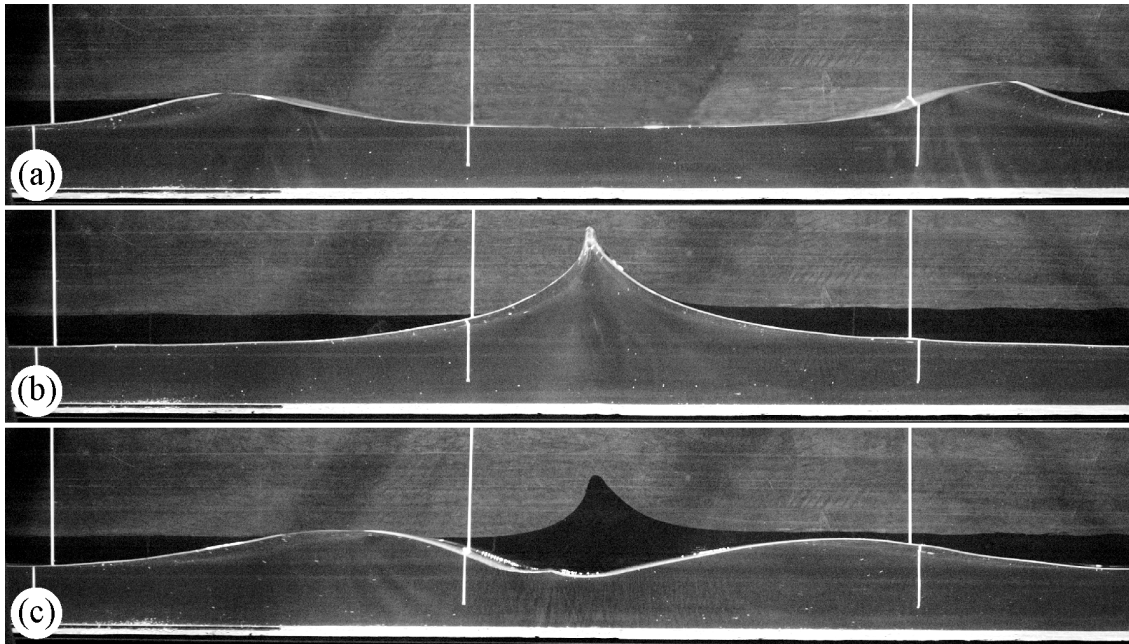


Figure 4-3 Collision of two waves in the VAW channel: (a) two similar solitary waves approach each other, (b) they meet and form a non-linear water oscillation and (c) after they have crossed their profiles have changed only insignificantly as a result of the collision (Heller 2007).

4.2.1 Water body geometries between 2D and 3D

Step 1 in Chapter 3 covers the idealised 2D and 3D water body geometries only. Heller *et al.* (2009) highlighted the need to investigate the behaviour of landslide-generated impulse waves in intermediate geometries between 2D and 3D. This has been addressed in the meantime along with a quantification of how the impulse wave characteristics in 3D relate to the ones observed in 2D (Heller *et al.* 2012, 2016, Heller and Spinneken 2015, Ruffini *et al.* 2019). This section starts with an illustration of the relevance of the effect of the water body geometry, followed by a method to quantify impulse waves in intermediate geometries based on Eqs. (3.13) and (3.16) for 2D.

In the slide impact zone, the wave height in 3D is only 20% smaller than in 2D, for the violent block slide event (large F , S and M and thus P) investigated by Heller *et al.* (2012). This extreme slide event supports the finding of Huber and Hager (1997) that the waves in the impact zone in 3D and 2D deviate little from each other. However, less violent events (small F , S and M and thus P) investigated by Heller and Spinneken (2015) showed that the wave magnitudes in the slide impact zone in 3D can already be a factor of 2.7 smaller than in 2D. This new research confirms that the basic assumption of identical wave heights at $x/h = r/h = 5$ used in Heller *et al.* (2009) is very imprecise for some impulse waves, hence, the parts of the method in the manual affected by this assumption have been replaced in this 2nd edition (Chapter 3). Independently of whether the waves are similarly large or not in the slide impact zone, they decay differently in the far field (Eq. (3.19) versus Eq. (3.29)). Heller *et al.* (2012) found a difference in 3D relative to 2D wave heights of nearly a factor of 4 at $x/h = r/h = 12.5$ on the slide axis, whilst the difference between 3D and 2D wave heights are typically an order of magnitude in the far field

at $x/h = r/h = 35$ (Heller and Spinneken 2015). Some guidance is thus required for wave heights and amplitudes in geometries between 2D and 3D.

Ruffini *et al.* (2019) introduced a method to quantify the wave parameters in intermediate geometries in the far field based on the 2D near field wave parameters. The method is developed for idealised geometries as shown in Figure 4-4 where the reservoir geometry is essentially a function of the water body side angles θ (Figure 4-4). The 6 investigated geometries involve the 2D ($\theta = 0^\circ$) and 3D ($\theta = 90^\circ$) cases as well as 4 intermediate geometries with $\theta = 7.5^\circ, 15^\circ, 30^\circ$ and 45° on both slide sides (symmetrical cases). Geometries with $\theta > 45^\circ$ were not investigated because the maximum wave parameters along the slide axis for such geometries are essentially identical to the ones observed in 3D (Heller *et al.* 2012). The water body beds were horizontal for all investigated cases.

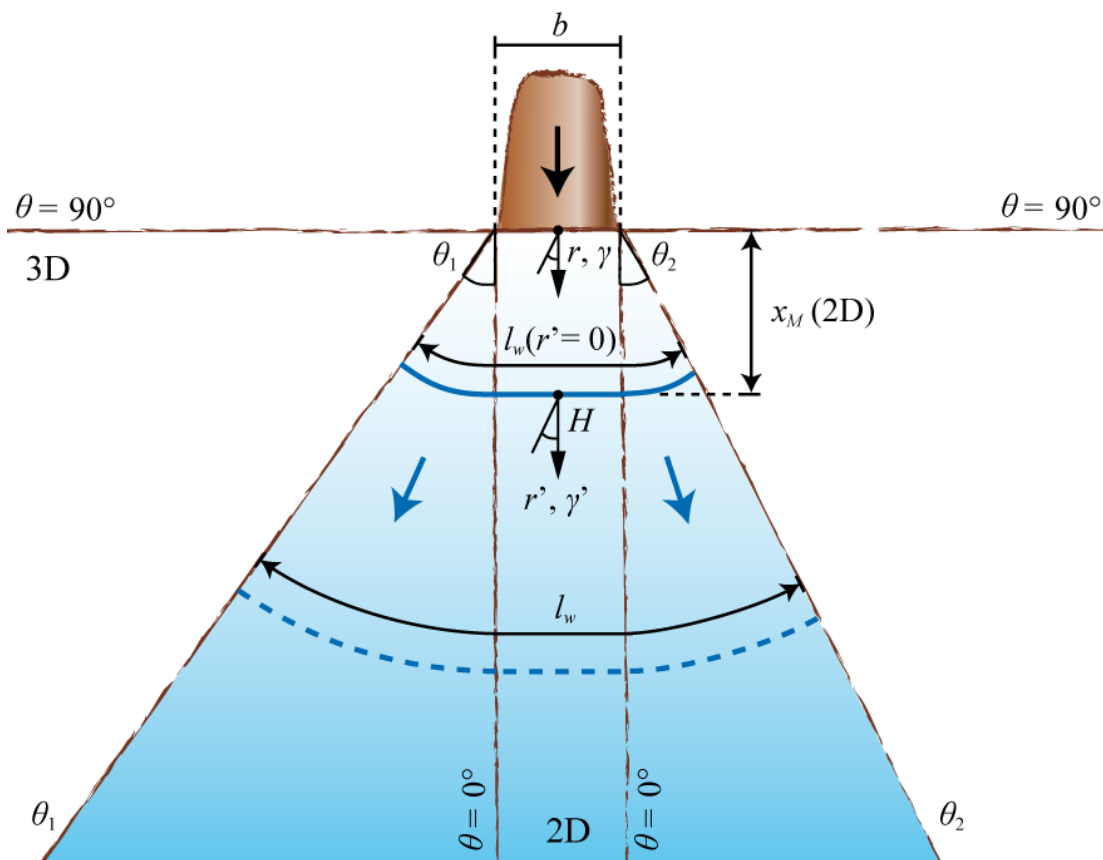


Figure 4-4 Sketch defining the governing parameters of wave propagation in water body geometries with water body side angles between $\theta = 0^\circ$ (2D) and 90° (3D); symmetrical case for $\theta_1 = \theta_2$ and asymmetrical case for $\theta_1 \neq \theta_2$.

Ruffini *et al.* (2019) investigated wave propagation with the numerical model SWASH. Four theoretical wave types were introduced in the geometries, namely (i) approximate linear waves, (ii) 5th order Stokes waves, (iii) 5th order cnoidal waves and (iv) 1st order solitary waves. The following concentrates on the wave types Stokes, cnoidal and solitary only (Chapter 2) as impulse waves are non-linear. Figure 4-5 shows Stokes waves in 6 geometries at different distances $r'/h = 3.0, 7.5, 15$ and 35 from the wave

generation zone. Note that the generation zone is located at the boundary between the near and far fields such that the coordinate system shown in Figure 3-3 is shifted downwave and specified with an apostrophe (x' , r' , etc.). The offset between x and x' can be computed with Eq. (3.14). The waves in 2D in Figure 4-5 stay reasonably constant over all distances, but they decrease in size with increasing θ ; at a distance $r'/h = 3.0$ the difference between the wave heights in 2D and 3D features already a factor of 2.8 and this difference increases further to a factor of 8.4 at $r'/h = 35$.

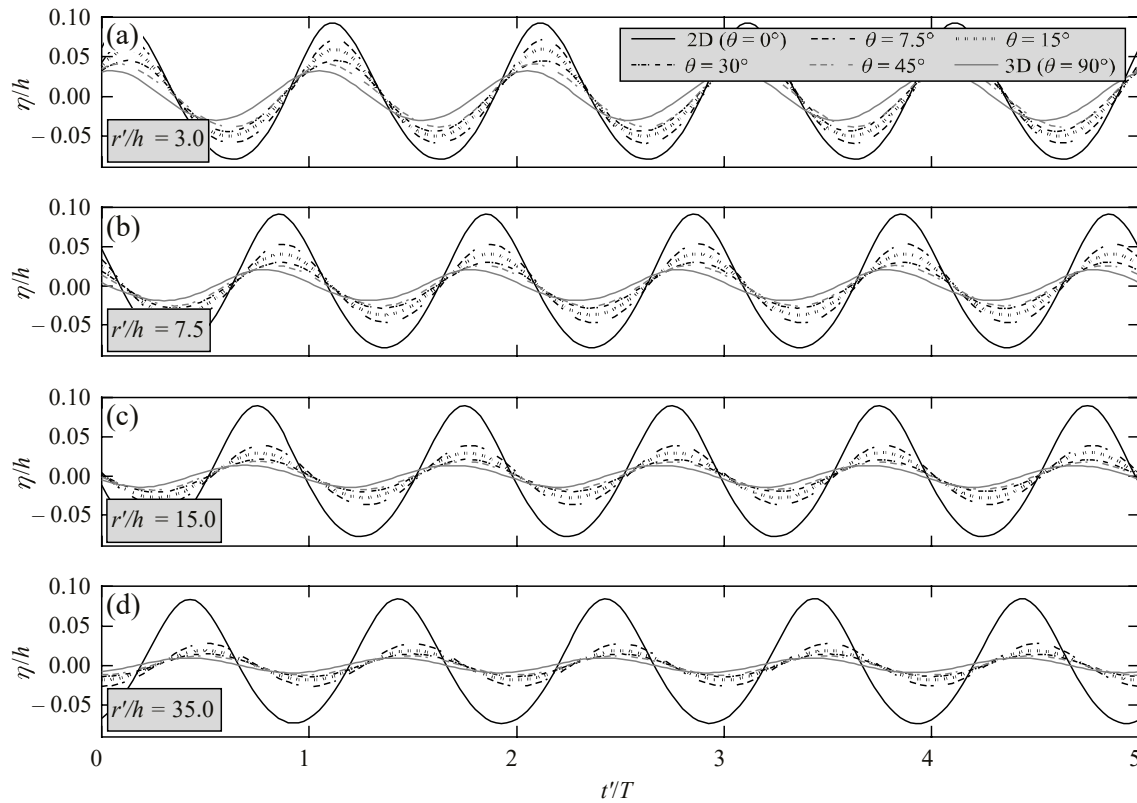


Figure 4-5 Relative water surface elevation η/h versus time normalised with the wave period t'/T for 5th order Stokes waves at different relative distances r'/h (Ruffini *et al.* 2019).

The wave heights H extracted from Figure 4-5 are plotted in Figure 4-6 in dimensionless form H/h over the relative wave front length l_w/h . The wave front length l_w (Figure 4-4) is given by

$$l_w(r', \theta) = b + 2r'\theta_{rad}. \quad (4.2)$$

b [m]	=	Slide width in 2D
l_w [m]	=	Wave front length
θ_{rad} [rad]	=	Water body side angle in radians (Figure 4-4)

The data of all geometries along the slide axis collapse on a parabola given by Eq. (4.1) if the width b_2 is replaced by the wave front length l_w at the corresponding position. The

maximum wave height along the slide axis in any geometry can therefore be derived based on Eq. (4.1) by considering Eq. (4.2). The wave amplitude a can be derived analogously by replacing H with a in Eq. (4.1) (Ruffini *et al.* 2019).

All wave heights at any position (along and off the slide axis) for all 6 geometries are plotted in Figure 4-6(b). The wave height is included in the expression $H/h/(b'/l_w)^{1/2}$ on the y -axis which is plotted over the wave propagation angle γ' . The semi-theoretical black curve in Figure 4-6(b) involves again Eq. (4.1) and is identical for all investigated wave types by Ruffini *et al.* (2019). This semi-theoretical curve is given by Eq. (4.3), and the corresponding expression for a is given in Eq. (4.4), as

$$\frac{H(r', \gamma', \theta) / h}{(b' / l_w(r', \theta))^{1/2}} = \beta \frac{H(r' = 0, \gamma' = 0^\circ, \theta = 0^\circ)}{h} \cos^2 \left(\frac{\gamma'}{3} \right) \quad (4.3)$$

$$\frac{a(r', \gamma', \theta) / h}{(b' / l_w(r', \theta))^{1/2}} = \beta \frac{a(r' = 0, \gamma' = 0^\circ, \theta = 0^\circ)}{h} \cos^2 \left(\frac{\gamma'}{3} \right) \quad (4.4)$$

$a(r', \gamma', \theta)$ [m]	=	Wave amplitude (Figure 3-3) in any geometry
$a(r' = 0, \gamma' = 0^\circ, \theta = 0^\circ)$ [m]	=	Wave amplitude (Figure 3-3) in 2D
b' [m]	=	Source width at the coupling location in 2D
h [m]	=	Still water depth
$H(r', \gamma', \theta)$ [m]	=	Wave height (Figure 3-3) in any geometry
$H(r' = 0, \gamma' = 0^\circ, \theta = 0^\circ)$ [m]	=	Wave height (Figure 3-3) in 2D
l_w [m]	=	Wave front length
r' [m]	=	Radial distance from the coupling location
β [-]	=	Pre-factor in Eqs. (4.3) and (4.4) (Table 4-1)
γ' [°]	=	Wave propagation angle from the coupling location (Figure 3-3b)
θ [°]	=	Water body side angle (Figure 4-4)

The pre-factors β in Eqs. (4.3) and (4.4) are available from Table 4-1 and differ for each wave type.

Table 4-1 Pre-factor β in Eqs. (4.3) and (4.4) for different wave types observed in 2D classified with the wave type product $T = S^{1/3}M\cos(6/7\alpha)$.

Wave type	Stokes waves	cnoidal waves	solitary wave
Classification based on T and F for granular slides in 2D	$T < 4/5F^{-7/5}$	$4/5F^{-7/5} \leq T \leq 11F^{-5/2}$	$4/5F^{-7/5} \leq T \leq 11F^{-5/2}$
β for Eq. (4.3)	1.10 (+13%, -14%)	1.03 (+23%, -12%)	1.20 (+36%, -21%)
β for Eq. (4.4)	1.01 (+17%, -14%)	0.85 (+26%, -39%)	0.84 (+36%, -38%)

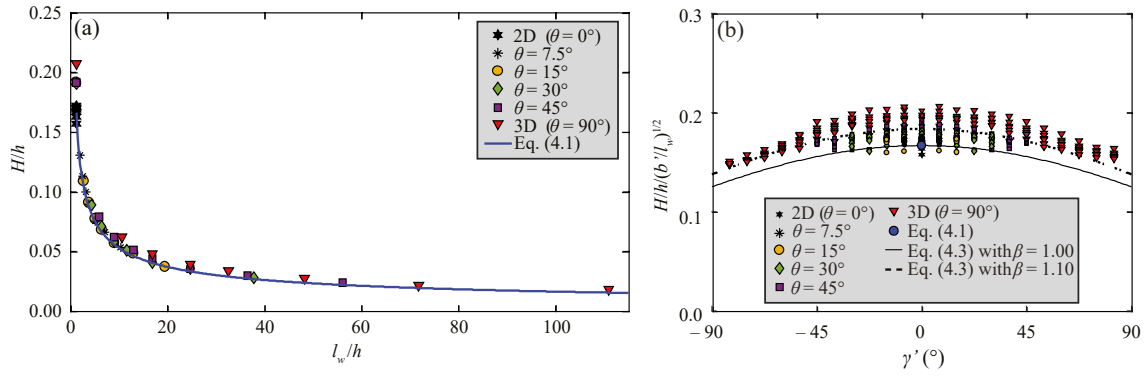


Figure 4-6 Wave height prediction of 5th order Stokes waves: (a) relative wave height H/h decay along the slide axis with l_w/h and (b) lateral wave height decay compared with Eq. (4.3) (after Ruffini *et al.* 2019).

The wave parameters in reservoir geometries deviating from the idealised 2D and 3D cases can be evaluated based on the following steps (Ruffini *et al.* 2019):

1. Define the landslide parameters $b, s, V_s, \alpha, m_s, \rho_s, \rho_w$ and h
2. Evaluate the wave type in 2D using the wave type product $T = S^{1/3} M \cos(6/7 \alpha)$
3. Calculate the maximum wave height H_M for 2D and its position from the slide impact $r = d_M$
4. Define θ_1 and θ_2 (Figure 4-4) at the slide sides to approximate the current geometry with an idealised one up to $r' = 0$ and calculate the wave front length $l_w(r' = 0, \theta)$
5. Compute $H(r' = 0, \gamma' = 0^\circ, \theta)$ by applying energy conservation $H(r' = 0, \gamma' = 0^\circ, \theta) = H_M(r' = 0, \gamma' = 0^\circ, \theta = 0^\circ)(b/l_w(r' = 0, \theta))^{1/2}$
6. Define θ_3 and θ_4 (Figure 4-3) at the slide sides to approximate the geometry up to a desired distance $r' > 0$, thereby taking any restrictions or expansions of the water body into account, and calculate $l_w(r', \theta)$
7. Use Eqs. (4.3) and (4.4) to calculate $H(r', \gamma', \theta)$ and $a(r', \gamma', \theta)$ at the desired location

This approach is illustrated in Chapter 5 with the 2014 Lake Askja case where a subaerial landslide-generated impulse wave reached a maximum run-up height of 71 m.

The introduced method from Ruffini *et al.* (2019) is based on idealised waves which essentially exclude frequency dispersion. While this method results only in slightly larger wave predictions for waves in or close to the shallow-water regime (cnoidal- and solitary-like waves), it may over-predict the wave parameters for waves closer to the deep-water regime. E.g. at a relative distance $x/h = 12.88$ in 2D the wave amplitude in the laboratory (including frequency dispersion) is 30% smaller than based on the method of Ruffini *et al.* (2019) (excluding frequency dispersion). The discrepancy between waves affected by frequency dispersion and the idealised waves is likely to increase with increasing relative distance. This means that the method of Ruffini *et al.* (2019) is likely to overpredict the wave magnitude and operates on the safe side.

Heller *et al.* (2012) investigated a slide mass impacting at the corner of a reservoir, similarly as a potential scenario for the K uthai reservoir investigated by Fuchs *et al.* (2011). The behaviour of the impulse waves in this geometry is somehow distinct, but reasonably close to the values observed for a geometry with $\theta = 15^\circ$ for the slide event investigated by Heller *et al.* (2012). In other words, the values for the wave parameters for a slide impacting in the corner of a reservoir are much closer to the values in 3D than in 2D. This is in line with the findings of Fuchs *et al.* (2011) where the potential K uthai reservoir case was investigated with a prototype-specific model at scale 1:130 and the wave height values predicted with the 2D method of Heller *et al.* (2009) significantly overpredicted the actually measured values in the physical model.

4.2.2 Constriction at dam flanks

M uller (1995) measured the run-up height on dam faces taking account of a lateral reservoir flank. The angle between the dam and the valley slope acts as a constriction (Figure 4-7a). Even if a deep-water wave approaches the shore it will, as the still water depth decreases, transform into a shallow-water wave and be influenced by the bed due to shoaling. Figure 4-7(b) shows, for a lateral shore inclination of 3:4, the relation of the run-up height to the run-up height at the dam centre R/R_m , as a function of the relative width of the reservoir flank l/l_F . The wave run-up heights in the vicinity of the inclined shore are about 20-30% greater than at the centre of the dam. The run-up height based on Green's law according to Eq. (4.1) is also shown. However, it overpredicts the wave height at the dam flank. M uller (1995) gives two possible explanations: (i) the wave in the model does not approach the lateral reservoir flank directly, and (ii) the friction losses at the bed reduce the run-up height in the model compared with its theoretical value as deduced from Green's law.

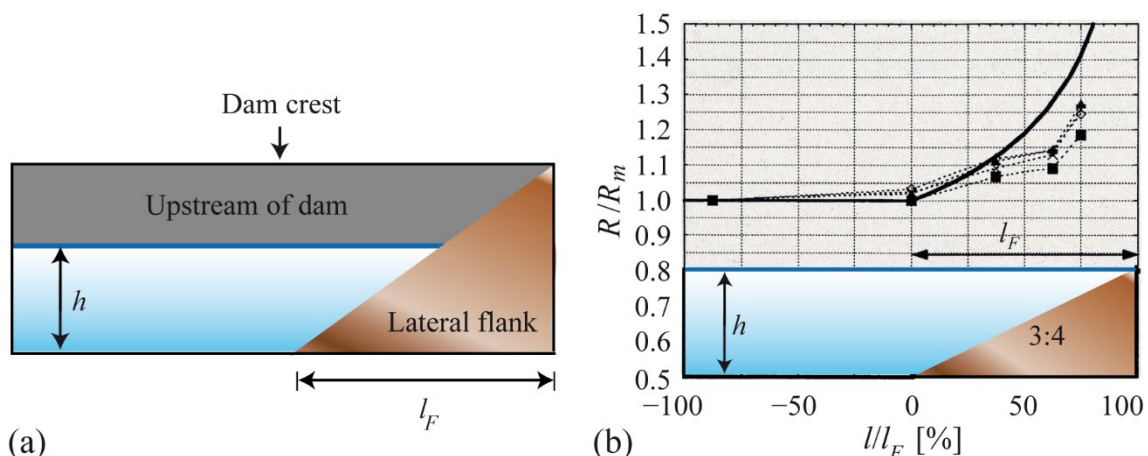


Figure 4-7 Run-up height as a consequence of an inclined lateral reservoir flank and constriction: (a) definition sketch showing the lateral flank of the reservoir and (b) relationship of the run-up height to the run-up height at the dam centre R/R_m as a function of the relative width of the reservoir flank l/l_F [%] as well as the values calculated from Green's law (—) according to Eq. (4.1) (after M uller 1995).

4.2.3 Ice cover

The effects of *ice cover* on impulse waves were investigated by Müller (1995). Ice up to 0.5 m thick has a negligible effect on wave attenuation, irrespective of whether the cover is broken or compact. A prerequisite for this is that the slide mass pierces through the ice layer. If a snow avalanche does not succeed in penetrating the ice layer two dangers may nevertheless arise on the shore; the additional weight may cause the ice cover to tip into an inclined position and thus create a small impulse wave, or water which is displaced under the ice cover may, for instance, flow up from under the ice on the shore.

4.3 Edge waves

Excluded from Step 1 in Chapter 3 are edge waves, also known as lateral onshore wave run-up or trapped waves. Edge waves propagate along the same slope as the landslide moves in the 3D water body as shown in Figure 4-8. There are situations where the maximum edge wave run-up height R_{eM} exceeds the waves predicted in Step 1 in 3D and the physics of edge waves is different from the offshore waves covered in Step 1 such that some findings about edge waves are summarised hereafter.

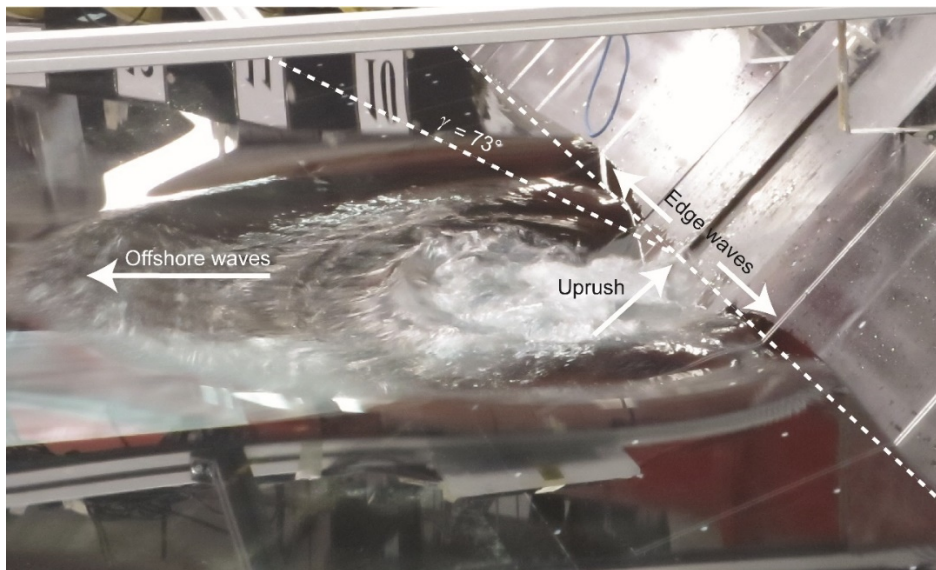


Figure 4-8 Landslide-tsunami propagation in 3D from a 45° slope with offshore propagating waves, edge waves and the uprush in the wake of the already submerged landslide (after Heller and Spinneken 2015).

Edge waves on sloping straight coasts were investigated by Ursell (1952), Lynett and Liu (2005), Di Risio *et al.* (2009a), Heller and Spinneken (2015) and McFall and Fritz (2017), amongst others. Edge waves were also quantified at conical islands by Di Risio (2009b) and McFall and Fritz (2017); these results are applicable to round volcanic islands or the front of strongly curved slopes such as peninsulas (Figure 4-1a). Mainly findings of Heller and Spinneken (2015) and McFall and Fritz (2017) are included hereafter.

These authors correlated the edge wave features by considering the water depth h and thus essentially use the same dimensionless parameters as introduced in Section 3, allowing for a coherent consideration of edge waves in this manual. Further, the focus is on the maximum edge wave run-up height R_{eM} and its decay with distance r as the most relevant parameter regarding hazard assessment. The reader is referred to Heller and Spinneken (2015) and McFall and Fritz (2017) for further results such as the maximum edge wave run-down and the wave length.

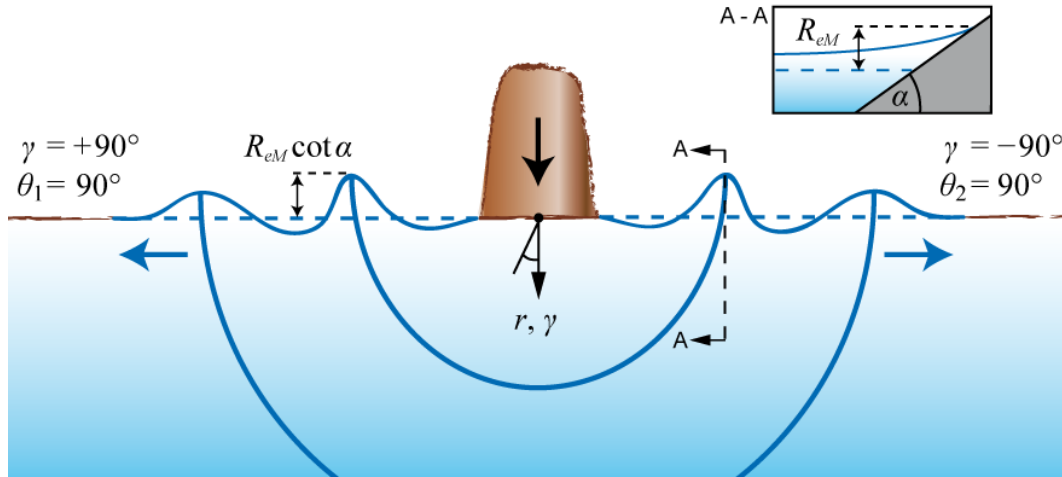


Figure 4-9 Definition sketch of edge wave propagation on a planar slope with top and side view.

Heller and Spinneken (2015) conducted 18 experiments in a wave basin with block slides. They found that the relative primary offshore wave amplitude $a_{c1}/h(r/h, \gamma = 0^\circ)$ is roughly a factor of three larger than the primary edge wave run-up height $R_{e1}/h(r/h, \gamma = 90^\circ)$. However, the primary offshore wave amplitude closer to the basin boundary is smaller with $a_{c1}/h(r/h, \gamma = 73^\circ) \approx 0.82R_{e1}/h(r/h, \gamma = 90^\circ)$ (Figures 4-8 and 4-9). This illustrates that the run-up R_{e1} is larger than the corresponding offshore wave amplitude at $\gamma = 73^\circ$, such that the edge wave may exceed the run-up height caused by the offshore waves for situations where the landslide slope connects directly to the dam flank or to the shore of interest. The maximum edge wave run-up height R_{eM} , irrespectively if observed at the primary or at a later wave within the wave train, is given by

$$\frac{R_{eM}}{h} = 0.15[1 - \exp(-1.5FM)] \quad (4.5)$$

b [m]	=	Slide width (Figure 3-3b)
F [-]	=	Slide Froude number; $F = V_s/(gh)^{1/2}$
g [m/s ²]	=	Gravitational acceleration; $g = 9.81 \text{ m/s}^2$
h [m]	=	Still water depth (in the slide impact zone)
M [-]	=	Relative slide mass; $M = \rho_s V_s / (\rho_w b h^2)$
R_{eM} [m]	=	Maximum edge wave run-up height

V_s [m/s]	=	Slide impact velocity
V_s [m ³]	=	Bulk slide volume (Figure 3-3a)
ρ_s [kg/m ³]	=	Bulk slide density (Figure 3-3a)
ρ_w [kg/m ³]	=	Water density

Table 4-2 Limitations to calculate the maximum edge wave run-up with Eq. (4.5).

Term	Range	Definition
Slide Froude number	$0.54 \leq F \leq 2.47$	$F = V_s/(gh)^{1/2}$
Relative slide thickness	$0.25 \leq S \leq 0.50$	$S = s/h$
Relative slide mass	$0.25 \leq M \leq 2.49$	$M = \rho_s V_s / (\rho_w b h^2)$
Slide impact angle	$\alpha = 45^\circ$	α
Relative streamwise distance	$3.0 \leq r/h \leq 22.5$	r/h

The parameter limitations for Eq. (4.5) are given in Table 4-2. R_{eM} was never observed at the first wave in the wave train; in 14 out of the 18 experiments it was measured at the second wave, in 3 at the third and in 1 experiment even at the fourth wave within the wave train. The travel of the wave maximum backwards in the wave train is typical for dispersive waves and in agreement with the findings of Di Risio *et al.* (2009a,b). Eq. (4.5) applies only to the region outside the slide path and shows that the run-up height R_{eM} reaches a limit of $0.15h$. Water may run-up much higher in the slide path which is less relevant, however, as this region is already affected by the landslide. This run-up is a consequence of the impact crater and strictly speaking no edge wave (Figure 4-8). A similar limit for R_{eM} was found by Di Risio *et al.* (2009b) for edge waves propagating around a conical (volcanic) island. McFall and Fritz (2017) present an alternative to Eq. (4.5) for the maximum edge waves which predicts up to $R_{eM}/h \approx 0.25$ for their experimental conditions. In most studies R_{eM} was observed some distance away from the slide impact location, e.g. Di Risio *et al.* (2009a) observed it at $r \approx 2b$, Heller and Spinneken (2015) measured R_{eM} within $r/h \leq 10$ and McFall and Fritz (2017) at $r \approx 1.23b$.

Correlations for edge wave decays with distance r/h are provided by Heller and Spinneken (2015) and McFall and Fritz (2017). Heller and Spinneken (2015) found an expression for the decay of the primary edge wave in function of $(r/h)^{-0.67}$. This decay lays between the primary wave decay $(x/h)^{-0.30}$ observed in 2D and $(r/h)^{-1.0}$ in 3D for the offshore waves under the same experimental conditions. This indicates once more that the edge waves may be larger at some distance from the slide impact zone than 3D waves due to a slower decay.

McFall and Fritz (2017) derived an edge wave decay expression for the largest wave, irrespectively where it is observed in the wave train. They conducted landslide-tsunami experiments in a wave basin with granular material accelerated by pneumatic pistons prior to impact. They presented the following expression based on the parameter limitations in Table 4-3

$$\frac{R_{eM}(r)}{h} = 0.2F^{1.15}S^{0.5}V^{0.12}(r/h)^{-0.2F^{0.35}B^{0.08}V^{-0.30}} \quad (4.6)$$

b [m]	=	Slide width (Figure 3-3b)
B [-]	=	Relative slide width; $B = b/h$
F [-]	=	Slide Froude number; $F = V_s/(gh)^{1/2}$
g [m/s ²]	=	Gravitational acceleration; $g = 9.81$ m/s ²
h [m]	=	Still water depth (in the slide impact zone)
r [m]	=	Radial distance from the impact location in the wave basin (Figure 3-3b)
R_{eM} [m]	=	Maximum edge wave run-up height
s [m]	=	Slide thickness (Figure 3-3a)
S [-]	=	Relative slide thickness; $S = s/h$
V_s [m/s]	=	Slide impact velocity
V [-]	=	Relative slide volume; $V = \mathcal{V}_s/h^3$
\mathcal{V}_s [m ³]	=	Bulk slide volume (Figure 3-3a)

Note that the relative slide volume V in Eq. (4.6) is differently defined than elsewhere in this manual. For typical values of $F = 2.0$, $B = 4.0$ and $V = 10$, Eq. (4.6) results in a decay of $(r/h)^{-0.14}$, which is much slower than $(r/h)^{-0.67}$ found by Heller and Spinneken (2015) for the primary wave. This may again be explained by frequency dispersion. McFall and Fritz (2017) expanded Eq. (4.6) to conical islands with hill slope coefficients reducing to 1 in the case of planar slopes covered by Eq. (4.6).

Table 4-3 Limitations to calculate the maximum edge wave decay with Eq. (4.6).

Term	Range	Definition
Slide Froude number	$1.05 \leq F \leq 3.85$	$F = V_s/(gh)^{1/2}$
Relative slide thickness	$0.08 \leq S \leq 0.46$	$S = s/h$
Relative slide volume	$0.2 \leq V \leq 28$	$V = \mathcal{V}_s/h^3$
Relative slide width	$1.0 \leq B \leq 7.0$	$B = b/h$
Slide impact angle	$\alpha = 27.1^\circ$	α
Relative streamwise distance	$0 \leq r/h \leq 28$	r/h

The edge wave celerity is slightly slower than for offshore waves and can be approximated with the 0th mode of the dispersion relation given by Ursell (1952). This is not further detailed here as the estimation of the celerity based on Eqs. (3.17), (3.32), and (3.33) for the offshore propagating waves is faster and thus on the safe side and the travel distances of impulse waves in lakes and reservoir is often short (it typically takes the waves in the region of minutes to reach the critical infrastructure). Nevertheless, it is recommended to take edge waves into account in landslide-generated impulse wave hazard assessments. This is particularly important if a slide impacts in proximity of a dam

where the landslide slope connects directly (in a straight line) with the dam flank or the shore in question and where critical infrastructure is located at the slide impact shore.

4.4 Mass movement types

The equations in Chapter 3 are based on granular or mesh-packed granular material. In natural conditions, however, there exists a range of mass movement types and slide compositions. Much research has been conducted to investigate these effects on impulse waves by Heller and Kinnear (2010), Heller and Spinneken (2013), Bolin *et al.* (2014), Evers and Hager (2015), Lindstrøm (2016), Heller *et al.* (2018) and Tang *et al.* (2018) since the first release of the manual over 10 years ago to complement the then available findings of Zweifel (2004) and Ataie-Ashtiani and Nik-Khah (2008). If the mass moves as one block, then the wave height H is normally larger than that for granular material. How much depends essentially on the grain diameter and the slide impact velocity. At low velocity water can enter the pore volume of a granular slide whilst this is less well possible at a larger velocity as well as for a block of porosity $n \approx 0$ as it displaces all the water (Lindstrøm 2016). Furthermore, the shape of a granular slide is changing during impact compared to blocks where it remains constant (Zweifel 2004; Heller and Spinneken 2013).

Classifications help to judge whether a mass moves as a granular slide rather than as a solid body. In this section, the mass movement types and their processes are discussed, as described by Cruden and Varnes (1996), for rock, debris or earth. This information also helps the understanding of the processes for snow and ice avalanches as well as for glacier calving. An alternative classification was, for example, developed by Nemcok *et al.* (1972).

A mass movement may be roughly defined by two nouns; the material in question followed by the movement type, for example landslide or rockfall. Cruden and Varnes (1996) identified five mass movement types (Figure 4-10):

- *Sliding* (Figure 4-10a): the slide mass can move rotating (Figure 4-10a) along a curved concave slide plane or by translation on a plane. Slides can move as solid bodies or as granular material; in the latter case the bulk slide volume V_s increases during the travel to the impact zone (Subsection 3.2.3).
- *Flowing* (Figure 4-10b): the mass behaves similar as a viscous liquid.
- *Falling* (Figure 4-10c): a fall may be considered to be mostly a free-fall, if the hill slope angle $\alpha > 76^\circ$; if this angle is smaller the mass falls onto the slope where it typically breaks.
- *Toppling* (Figure 4-10d): the mass moves around a rotation point or axis located below its centre of gravity.

- *Spreading* (Figure 4-10e): the mass volume spreads and breaks into finer material. This movement type occurs when the slope angle is small $0.3^\circ \leq \alpha \leq 5^\circ$ and is most often triggered by an earthquake. This form of movement is rarely significant, in particular in Alpine regions, for the generation of impulse waves.

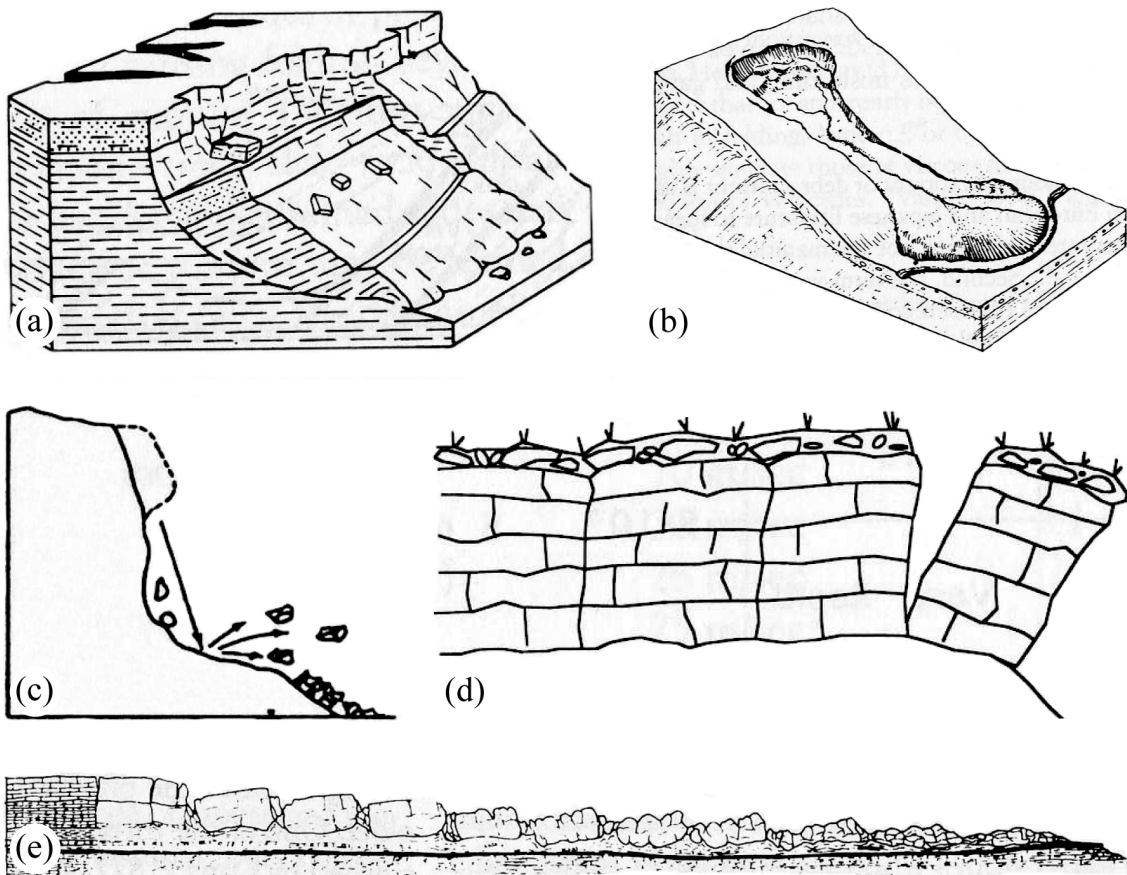


Figure 4-10 Mass movement types: (a) sliding, (b) flowing, (c) falling, (d) toppling and (e) spreading (Cruden and Varnes 1996).

The effect of the slide type and composition on impulse waves is addressed hereafter. Heller and Spinneken (2013) conducted 144 experiments in 2D based on block slides and compared the results to the 2D granular slide tests of Heller and Hager (2010) (Section 3.2.4.2). They also varied three previously ignored block model parameters namely the blockage ratio $b/b_f = 0.88, 0.96$ and 0.98 (the width of the slide b relative to the flume width b_f), the slide front angle ϕ ($30, 45, 60$ and 90°) and the transition type at the slope toe (no transition where the blocks stopped immediately versus a circular transition where the blocks run-out more smoothly). The blocks with a slide front angle of 90° generated on average 55% larger wave heights $H(x)$ than blocks with 30° and the wave heights generated with a circular transition were also 39% larger on average than in experiments with no transition. On the other hand, the change in the blockage ratio affected the wave height only by 8.9% on average. Based on these findings, Heller and Spinneken (2013)

found new correlations for their 2D block model experiments for all relevant wave parameters such as a_{Mb} , H_{Mb} , $a_b(x)$, $H_b(x)$, etc. A systematic comparison of impulse waves generated by block compared to granular slides was performed by dividing their new equations by the equations for granular slides of Heller and Hager (2010) as introduced in Section 3.2.4.2.

Figure 4-11 shows a graphical representation of the upper and lower envelopes of some of these results, namely the observed ratios a_{Mb}/a_M , H_{Mb}/H_M , $a_b(x)/a(x)$ and $H_b(x)/H(x)$. The upper envelope is observed for the largest investigated blockage ratio $b/b_f = 0.98$, $\phi = 90^\circ$ and a circular transition such that the block runs out smoothly. This may represent the fairest comparison with granular slides in most situations as granular slides fill the entire channel width in 2D, they also adapt roughly to $\phi = 90^\circ$ during impact and they also run out relatively smoothly, even for a very abrupt change in the slope at the slope toe. The upper envelope shows that the impulse wave parameters generated by blocks are on average 1.3 to 1.9 times larger than generated by granular slides under otherwise identical conditions.

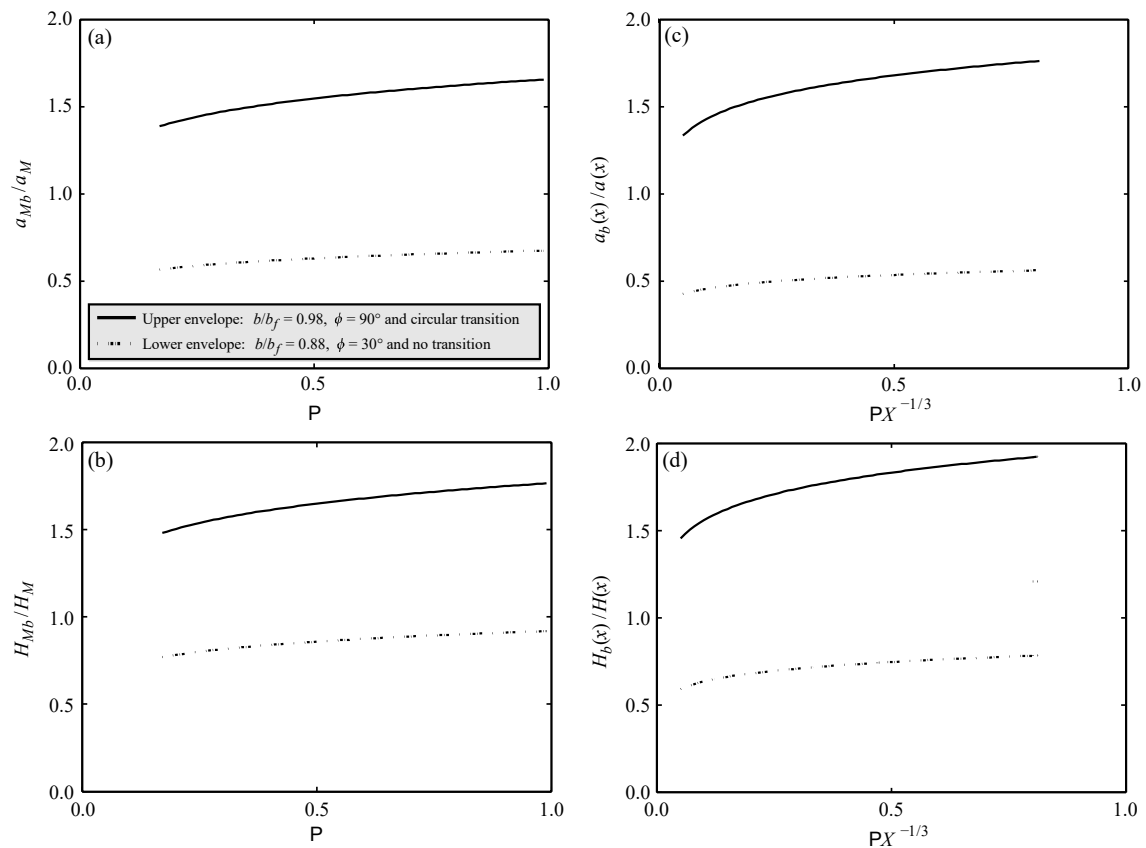


Figure 4-11 Upper and lower envelopes of the values of waves generated by block relative to the ones of granular slides: (a) maximum wave amplitude a_{Mb}/a_M versus impulse product parameter P , (b) maximum wave height H_{Mb}/H_M versus P , (c) wave amplitude $a_b(x)/a(x)$ versus $PX^{-1/3}$ and (d) wave height $H_b(x)/H(x)$ versus $PX^{-1/3}$ (after Heller and Spinneken 2013).

Heller and Spinneken (2013) also showed that block slides may generate up to 0.4 times smaller waves than granular slides if the block model parameters are much smaller

than $b/b_f = 0.98$ and $\phi = 90^\circ$ in combination with an abrupt change of the transition at the base of the slope such that the slide stops abruptly. The most extreme cases investigated are represented by the lower envelopes in Figure 4-11 (for $b/b_f = 0.88$, $\phi = 30^\circ$ and no transition (abrupt slide stop)). Whilst this lower case was observed in laboratory tests, it may be very rarely observed in real world events and also be challenging to predict. Details about this method and the corresponding empirical equations can be found in Heller and Spinneken (2013).

Lindström (2016) conducted five 2D experiments with a block and with four different granular materials with grain diameters of 3 to 25 mm. The investigated Froude numbers were in the range $0.34 \leq F \leq 0.93$. Lindström (2016) explained the change in the impulse wave magnitude in function of the slide type with the permeability k through the slide given by the Kozeny-Carman equation which simplifies for spherical grains impacting into water to

$$k = 55200 d_g^2 \frac{e^3}{1+e} \quad (4.7)$$

d_g [m]	=	Grain diameter
e [-]	=	Void ratio; $e = n/(1 - n)$
k [m/s]	=	Permeability
n [-]	=	Bulk slide porosity

If the granular slide impact velocity is $V_s < k$, then the water penetrates into the slide instantaneously as the slide enters the water, resulting in a reduction of the generated wave compared to a block. This was e.g. the case in Lindström's (2016) experiment based on alumina spheres with diameter $d_g = 0.025$ m and porosity $n = 0.43$ where $k = 6.13$ m/s was computed, compared to $V_s = 0.97$ m/s. On the other hand, if $V_s > k$, the slide will not be instantaneously penetrated by water during wave generation and the generated impulse wave agree better with block slide waves.

Equation (4.7) was developed for laminar flow through porous media (Carrier, 2003). This condition is not met for typical slide velocities during impulse wave generation. Nevertheless, the underlying principle still applies and helps to understand some previous findings in the technical literature; Zweifel (2004) found indeed in 2D experiments conducted in the range $0.5 \leq F \leq 2.8$ that impulse waves due to block slides generate up to 7.5 times larger waves than granular slides at $F = 0.5$ ($V_s < k$), but only 1.37 times larger waves at $F = 2.8$ ($V_s > k$). The later value is close to the corresponding value observed in Figure 4-11(a) which in addition shows the velocity dependence (smaller differences between impulse waves generated by block to granular slides with smaller P). Heller and Hager (2010) found the grain size distribution for tests involving $d_g = 2, 4, 5, 8$ mm and mixtures to be negligibly small for wave generation and Evers and Hager (2015) found by packing some of these materials into meshes that the differences between impulse

waves generated by free and mesh-packed granular materials are relatively small in 2D. However, some authors including Bolin *et al.* (2014) found that the effect of the grain size is not negligible anymore for a larger range of grain sizes namely $5 \text{ mm} \leq d_g \leq 100 \text{ mm}$. This seemingly contradiction can be explained with the k concept: k may change insignificantly for the relatively small range of d_g investigated by Heller and Hager (2010), but covers a wider range for larger ranges of d_g as investigated by Bolin *et al.* (2014).

The discussed studies in this Section 4.4 investigated the differences in impulse waves from block in relation to granular slides for the mass movement type “slide” (Figure 4-10a). Tsunamis generated by the fall and toppling cases (Figure 4-10c,d) were compared by Heller *et al.* (2019) in the context of iceberg calving. They conducted experiments in a wave basin and the icebergs were modelled with polypropylene homopolymer blocks with a size of $0.80 \text{ m} \times 0.50 \text{ m} \times 0.50 \text{ m}$ and $0.80 \text{ m} \times 0.50 \text{ m} \times 0.25 \text{ m}$. Several iceberg calving mechanisms were investigated including the fall and toppling (overturning) cases for subaerial, partially submerged and fully submerged icebergs. The overturning icebergs generated typically 50% larger maximum wave heights H_M than the icebergs that fell vertically into the water body.

Given that the slide type may change the wave magnitude by nearly a factor of 2 according to Figure 4-11, this effect should be taken into account for masses impacting as a block rather than a granular material such as rockfalls or iceberg calving.

4.5 Underwater slide deposits

Slides with a density larger than water propagate into the water body and may affect the intake structure or safety organs of the reservoir such as the bottom outlet. The sediments may either damage the structure itself or block the respective inlet opening. The location (final slide front position x'_{end}) and dimensions (maximum deposition thickness S_{end}) of the underwater slide deposits are therefore important in terms of a detailed hazard assessment (Figure 4-12).

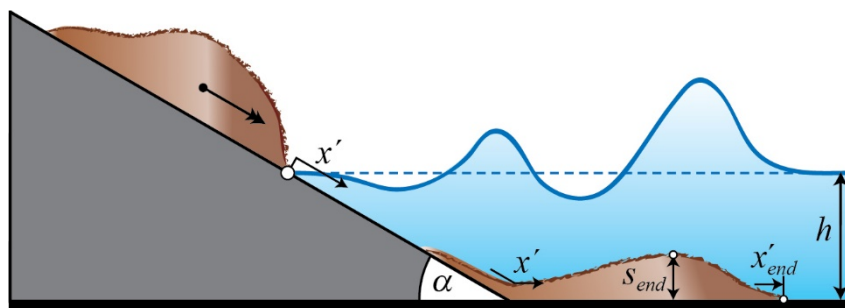


Figure 4-12 Sketch defining the parameters for underwater slide deposits.

The following equations are based on an analysis of the slide deposition geometry of 41 selected laboratory tests conducted in a 2D test set-up (Fuchs *et al.* 2013). In addition

to the final slide deposits presented below, Fuchs *et al.* (2013) also specified more detailed slide features, such as the underwater slide front propagation and velocity. Generally, a larger slide impact leads to larger underwater slide protrusion and thus smaller deposition thickness. However, according to their analysis, the underwater slide deposition is well represented by the impact angle-corrected relative slide mass, a static parameter excluding the slide impact kinematics:

$$M_s = m_s / (\rho_w b h^2) \sin[(6/7)\alpha]. \quad (4.8)$$

b [m]	=	Slide width (Figure 3-3)
h [m]	=	Still water depth (Figure 3-3)
m_s [kg]	=	Slide mass (Figure 3-3)
M_s [-]	=	Impact angle-corrected relative slide mass
α [°]	=	Slide impact angle (Figure 3-3)
ρ_w [kg/m ³]	=	Water density

A good correlation resulted for the main underwater landslide deposition parameters, i.e. the front position and thickness. For increasing M_s , the relative end position x'_{end}/h increases from 2 to 8 whereas the relative deposition thickness s_{end}/h decreases from 0.9 to 0.3.

$$x'_{end} = h(1.88M_s + 2.7) \quad (4.9)$$

$$s_{end} = h(0.79 - 0.2M_s) \quad (4.10)$$

h [m]	=	Still water depth (Figure 4-9)
M_s [-]	=	Impact angle-corrected relative slide mass from Eq. (4.8)
s_{end} [m]	=	Maximum thickness of slide deposits (Figure 4-9)
x'_{end} [m]	=	Front position of slide deposits (Figure 4-9)

Table 4-4 Limitations for underwater slide deposit calculations.

Term	Range	Meaning
Slide Froude number	$0.86 \leq F \leq 4.6$	$F = V_s / (gh)^{1/2}$
Relative slide volume	$0.19 \leq V \leq 2.97$	$V = V_s / (bh^2)$
Relative slide density	$1.43 \leq D \leq 1.72$	$D = \rho_s / \rho_w$
Relative slide mass	$0.27 \leq M \leq 5.0$	$M = \rho_s V_s / (\rho_w b h^2)$
Impact angle-corrected relative slide mass	$0.13 \leq M_s \leq 3.9$	$M_s = M [\sin(6/7)\alpha]$
Impulse product parameter	$0.18 \leq P \leq 4.83$	$P = FS^{1/2} M^{1/4} \{\cos[(6/7)\alpha]\}^{1/2}$
Grain Reynolds number	$8200 \leq R_g \leq 57000$	$R_g = V_s d_g / \nu$
Slide impact angle	$30^\circ \leq \alpha \leq 90^\circ$	α

Note that laboratory tests commonly underestimate the slide run-out as the grain Reynolds number R_g at reduced size is smaller than in nature (Davies and McSaveney 1999, Kessler *et al.* 2018). Further, landslides of volumes in excess of 10^6 m^3 show much larger run-outs above water than predicted with a typical basal friction angle, a phenomenon known as hypermobility or size effect (Pudasaini and Miller 2013). Large submarine landslides may also run-out significantly further than predicted with Eq. (4.9) (Hampton *et al.* 1996). Such effects may become relevant if the parameter limitations for the under-water slide deposit computations in Table 4-4 are violated.

4.6 Sensitivity analysis

This Section discusses the sensitivity of the run-up height R to variations of the governing parameters and defines those parameters to which R reacts particularly sensitively. As comprehensive calculation equations are available mainly for the Step 1, the sensitivity analysis relates only to them (Figure 3-1).

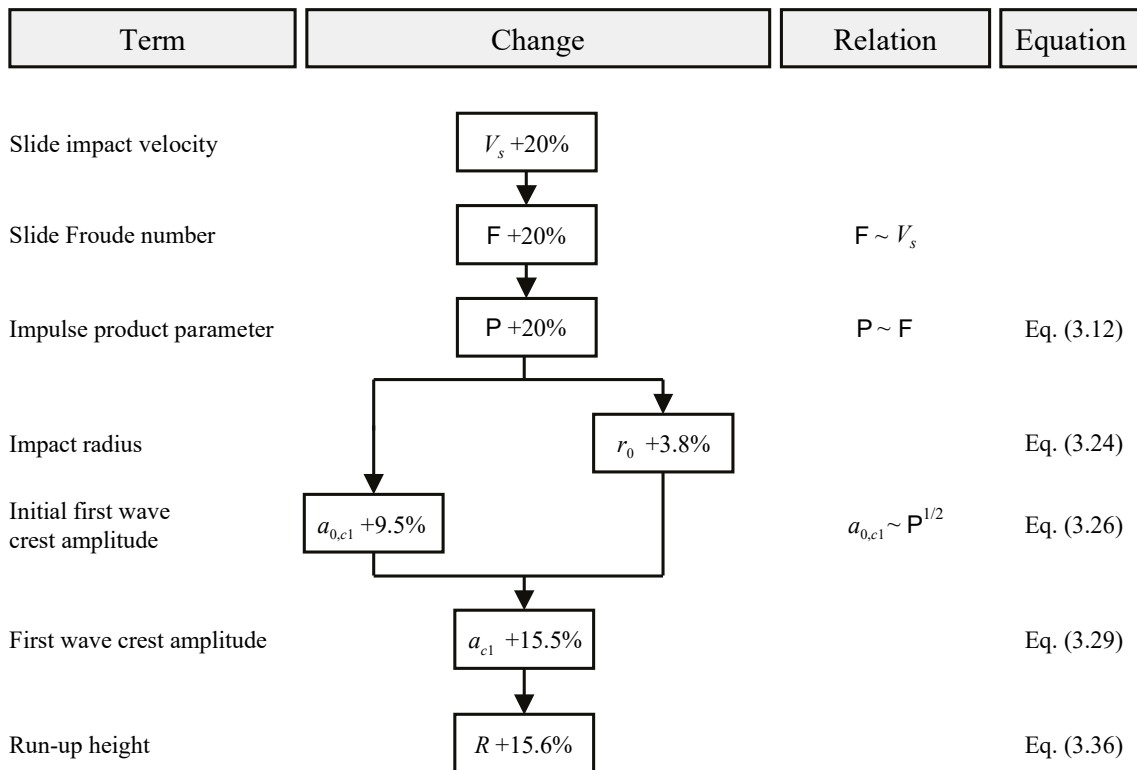


Figure 4-13 Calculation sequence to determine the effect on the run-up height R of a change of the slide impact velocity V_s by +20%.

Figure 4-13 shows the calculation sequence to determine the effect on the run-up height R of a change of the slide impact velocity V_s by +20% for the 3D case (Subsection 3.2.4.3). The following variables are included as initial governing parameters for wave generation and propagation: slide impact velocity $V_s = 40 \text{ m/s}$, still water depth $h = 50 \text{ m}$, slide thickness $s = 5 \text{ m}$, bulk slide volume $V_s = 50,000 \text{ m}^3$, bulk slide density $\rho_s = 1,700$

kg/m³, slide width $b = 50$ m, slide impact angle $\alpha = 45^\circ$, radial distance $r = 300$ m and the wave propagation angle $\gamma = 45^\circ$ (Subsection 3.2.2). The governing parameters considered for wave run-up and dam overtopping are the still water depth $h = 50$ m and the run-up angle $\beta = 20^\circ$ (Subsection 3.3.3). In this procedure, V_s was each time multiplied with 1.2 rather than 1.0, in order to determine the relative change. The value V_s occurs linearly in **F** and **P**. Equation (3.26) shows that the initial first wave crest amplitude $a_{0,c1}$ is proportional to $\mathbf{P}^{1/2}$, and the relative change decreases to $(1.2/1.0)^{1/2} = 1.095$ or +9.5%. The percentage change may be determined in steps for all those variables which are influenced directly or indirectly by V_s . Finally, the change of R may be determined. An increase of V_s by +20% raises R by +15.6% (Figure 4-13) for the given set of initial parameters. As the value of R is sensitive to V_s , the precise determination of the latter variable is important.

Analogous to Figure 4-13, the sensitivity of the run-up height R (Eq. 3.36) to a change by $\pm 20\%$ for the same set of initial parameters is determined for each of the individual governing parameters. These are illustrated in Figure 4-14. The individual parameters are presented in percentages as a bar chart, giving the variations and the extent of the effect on R . The radial distance r was intentionally not considered, as it may be determined precisely. The bulk slide porosity n was also neglected as it is only indirectly included in the equations through ρ_s .

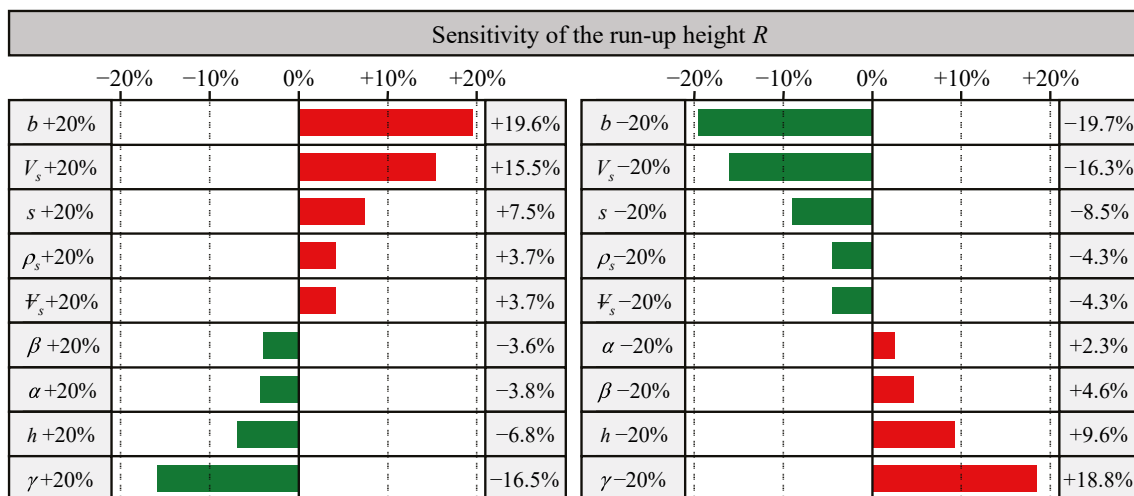


Figure 4-14 Sensitivity of the run-up height R according to Eq. (3.36) as a consequence of a variation of +20% (left) and -20% (right) of selected initial governing parameters for the 3D case, with an increasing effect in red and a decreasing effect in green on R .

The run-up height is particularly sensitive to the slide width b and slide impact velocity V_s because any variation of these slide parameters has a substantial influence (Figure 4-14). The wave propagation angle γ is not known exactly if the slide slope is inclined laterally and the principal impulse direction of the slide cannot be given clearly. The value R also reacts sensitively to γ . Finally, a relatively precise determination of the still water depth h and the slide thickness s are important. The effects of \mathcal{V}_s , ρ_s , α and β on R are of

secondary importance. From Figure 4-14 it can also be seen whether an increase or a decrease of a governing parameter acts negatively (red) or positively (green) on the value of R . To be on the safe side, the selected values of b , V_s , as well as of s , should be rather greater than estimated, and the corresponding values of h and γ rather smaller.

Figure 4-14 shows only the sensitivity of R to variations in each of the governing parameters by $\pm 20\%$ for a selected parameter set. Combinations of changes in the governing parameters were not considered. Note, especially in the 3D case, the effect of parameter variation does not propagate linearly and different sets of initial parameters may yield different sensitivities. Neither was the sensitivity of further variables such as the additional horizontal force component ΔF_h or the overtopping volume V per unit dam crest length included in Figure 4-14. Therefore, a specific sensitivity analysis should be conducted e.g. by applying the computational tool presented in Section 5.5.

4.7 Safety allowance

Basically, any dam overtopping by impulse waves should be prevented by precautionary water level lowering of the reservoir. Some safety considerations are given in this section. Further points are possible, depending on the prototype, and must be considered from case to case. The following factors affect the selection of *safety reserves*, for instance with regard to the run-up height R :

- (i) Scatter of the measurement points in the empirical equations
- (ii) Probability of occurrence of mass movement
- (iii) Extent of the deviations from the idealisation of Step 1
- (iv) Dam type (concrete dam, embankment dam with or without protective face)
- (v) Damage potential in the valley downstream of the dam

These factors are discussed in more detail hereafter.

- (i) Scatter of the measurement points in the empirical equations

The empirical equations presented in Chapter 3 are based on laboratory experiments. These equations do not accurately predict the measured data points, but the data points scatter within a certain range. The computational procedure of Chapter 3 applies these equations sequentially to calculate a target quantity. Similar to the calculation of error propagation (e.g. Hughes and Hase 2010), each individual scatter range needs to be considered to assess the prediction uncertainty of the overall process chain; i.e. the overall scatter of the run-up height R (Eq. 3.36) includes the individual scatter ranges of R as well as the wave amplitude a . For equation types composed as a product of power laws, the maximum relative scatter is equal *at most* to the sum of the individual values of the relative scatter of the parameters involved (Heller *et al.* 2009). In this case, a constant overall scatter value may be determined independently of the size of

the input parameters. For equations that are more complex, no single value for the overall scatter range may be given, but an individual determination for the present set of parameters is required. For example, the limitations for R regarding the relative wave crest amplitude $\varepsilon = a/h$ include 0.007 as the minimum and 0.69 as the maximum value (Table 3-4). With a scatter range of +25%, -45% (Table 4-5) for the first wave crest amplitude a_{c1} (Eq. 3.29) and $\pm 20\%$ for the run-up height R (Eq. 3.36), the maximum overall scatter of R results in +50%, -56% for $\varepsilon = 0.007$ and $\pm 61\%$ for $\varepsilon = 0.69$, respectively. Note, that the example does not consider the scatter range as a normally distributed probability density function, but assumes the likelihood of occurrence to be constant within the given scatter range. This approach yields a more conservative estimation of the overall scatter range.

Similar to the sensitivity analysis, the uncertainty propagation may be assessed by applying the computational tool (Hughes and Hase 2010). Table 4-5 gives individual scatter ranges for those equations, for which scatter ranges were provided in the original references. The scatter ranges are valid within the parameter limitations given in Chapter 3. Outside these limitations, the scatter may increase. Note that, except for the overtopping volume per unit crest length V at rigid dams (Eq. 3.38), all remaining wave overtopping related Eqs. (3.39) to (3.40) are based on solitary waves ($a/H = 1$). Consequently, larger scatter may arise for $a/H < 1$.

(ii) Probability of occurrence of mass movement

There are a number of signs that may indicate a larger probability of a catastrophic mass movement. For example already instable soil masses, e.g. creeping landslides, or metastable masses, e.g. dormant landslides that are only activated depending on pore water conditions, indicate zones with larger sliding potential. But also zones with increasing loss of permafrost may e.g. indicate a growing thread of collapse of rock masses. These situations do not form a complete list but aim to give examples for indicators of potentially catastrophic sliding. The higher the risk of occurrence of a slide, the more safety allowances are recommended.

(iii) Extent of the deviations from the idealisation of Step 1

In Step 1, according to Figure 3-1, computation equations are available. In Step 2, the effects of deviations from the idealisation in the Step 1 can often only qualitatively be determined. The greater the deviation from the idealised concept (e.g. rectangular reservoir form, granular slide), the greater safety allowances are needed.

(iv) Dam type (concrete dam, embankment dam with or without protective face)

Embankment dams without protection faces may be eroded by overtopping caused by impulse waves and, in the extreme case, this may lead to dam failure (Singh 1996).

Gravity and arch dams are more resistant in this respect. For example the Vaiont arch dam withstood overtopping by an impulse wave and suffered no damage except at the left hand side of the dam crest (Schnitter 1964).

(v) Damage potential in the valley downstream of the dam

The greater the population of the downstream valley that would be affected by the effects of an overtopping impulse wave or the greater the importance of the infrastructure of the valley, the larger should be the safety allowances. To determine the areas which would be affected, a numerical dam break simulation may be carried out.

Points (i) to (v) must be assessed case by case. Selection of the safety allowances depends much on the characteristics of the prototype. A publication by the International Commission On Large Dams ICOLD (2002) addresses risk management with regard to potential slides into reservoirs.

Table 4-5 Scatter ranges of empirical prediction equations.

Term	Symbol	Equation	Scatter
Maximum wave height (2D)	H_M	Eq. (3.13)	$\pm 30\%$
Streamwise distance of H_M (2D)	x_M	Eq. (3.14)	$\pm 50\%$
Wave period of H_M (2D)	T_M	Eq. (3.15)	$\pm 50\%$
Wave celerity (2D)	c	Eq. (3.17)	$\pm 15\%$
Wave height (2D)	H	Eq. (3.19)	$\pm 30\%$
Wave period (2D)	T	Eq. (3.20)	$\pm 100\%$
First wave crest amplitude (3D)	a_{c1}	Eq. (3.29)	+25%, -45%
First wave trough amplitude (3D)	a_{t1}	Eq. (3.30)	+40%, -25%
Second wave crest amplitude (3D)	a_{c2}	Eq. (3.31)	+50%, -60%
First wave crest celerity (3D)	c_{c1}	Eq. (3.32)	+10%, -15%
Second wave crest celerity (3D)	c_{c2}	Eq. (3.33)	+15%, -25%
First wave period (3D)	T_1	Eq. (3.34)	+15%, -10%
Run-up height	R	Eq. (3.36)	$\pm 20\%$
Overtopping volume per unit length dam crest (rigid dam)	V	Eq. (3.38)	$\pm 30\%$
Maximum overtopping flow depth (rigid dam)	d_0	Eq. (3.39)	$\pm 10\%$
Wave overtopping duration (rigid dam)	t_0	Eq. (3.40)	$\pm 10\%$

5 Computational examples

5.1 Example 1

5.1.1 Problem description and governing parameters

Figure 5-1 shows the reservoir geometry assumed for example 1. A rockfall at location A threatens to impact into a reservoir, which is covered by a 0.25 m thick layer of ice. Opposite the impact location there are critical infrastructure buildings. The maximum run-up height at point B as well as potential overland flow characteristics have to be determined. In addition, it has to be estimated whether the arch dam will be overtopped by the impulse wave and if so by how much the reservoir would have to be drawn down in order to prevent this overtopping. The freeboard at the shore is $f = 10$ m (Point B), while it is $f = 4$ m at the dam (Point C). The sections A-B and A-C, corresponding to the dashed lines in Figure 5-1, are shown in Figure 5-3.

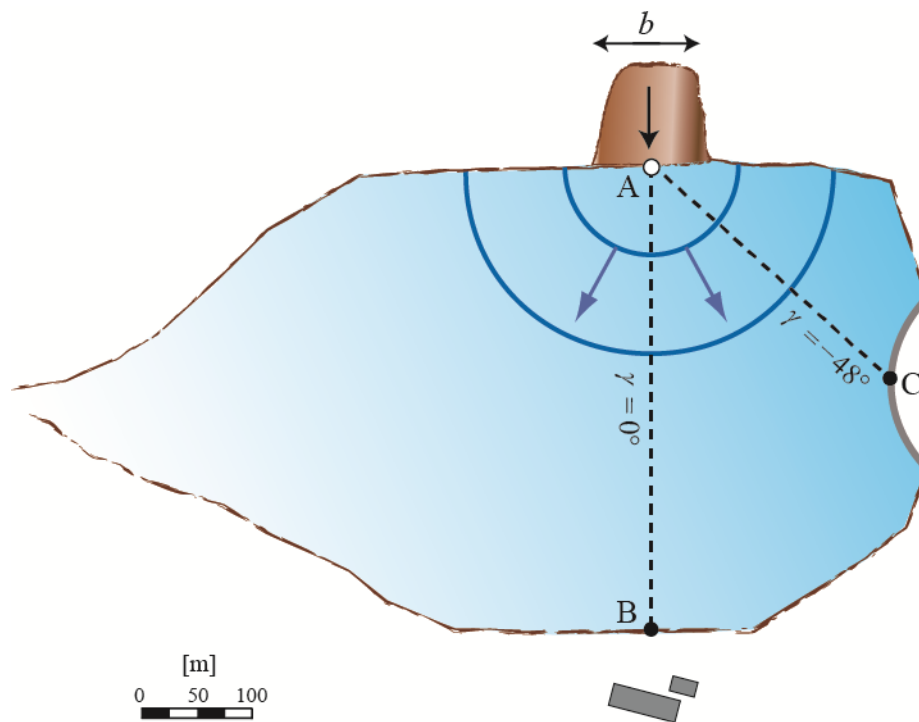


Figure 5-1 Reservoir geometry for example 1 with a rockfall impacting at point A; the reservoir is impounded by an arch dam.

The slide impact velocity V_s can be calculated using the detail from Figure 5-3(a) as shown in Figure 5-2. The parameters required to do this are given in Table 5-1. As there is a slope change, it is necessary to use both Eqs. (3.5) and (3.9) for the calculation of V_s . The slide velocity at the point of slope change V_{sNK} is given by

$$V_{sNK} = \sqrt{2g\Delta z_{scN} (1 - \tan \delta_N \cot \alpha_N)} \quad \text{after Eq. (3.5)}$$

$$V_{sNK} = \sqrt{2 \cdot 9.81 \cdot 100 (1 - \tan 20^\circ \cot 70^\circ)} = 41.3 \text{ m/s.}$$

From this the slide impact velocity V_s can be calculated as

$$V_s = \sqrt{V_{sNK}^2 + 2g\Delta z_{sc} (1 - \tan \delta \cot \alpha)} \quad \text{after Eqs. (3.2), (3.5) and (3.9)}$$

$$V_s = \sqrt{41.3^2 + 2 \cdot 9.81 \cdot 150 (1 - \tan 20^\circ \cot 40^\circ)} = 58.0 \text{ m/s.}$$

The calculated value of V_s , the governing parameters for wave generation, and those for the determination of the effects on the arch dam and on the opposite shore of the reservoir, are summarised in Table 5-2. The value b denotes the mean slide width and s is the maximum slide thickness in the impact zone. The values of bulk slide density ρ_s and bulk slide volume V_s also refer to the impact zone. The slide axis ($\gamma = 0^\circ$) is governing for the selection of the still water depth h (Figures 5-1 and 5-2).

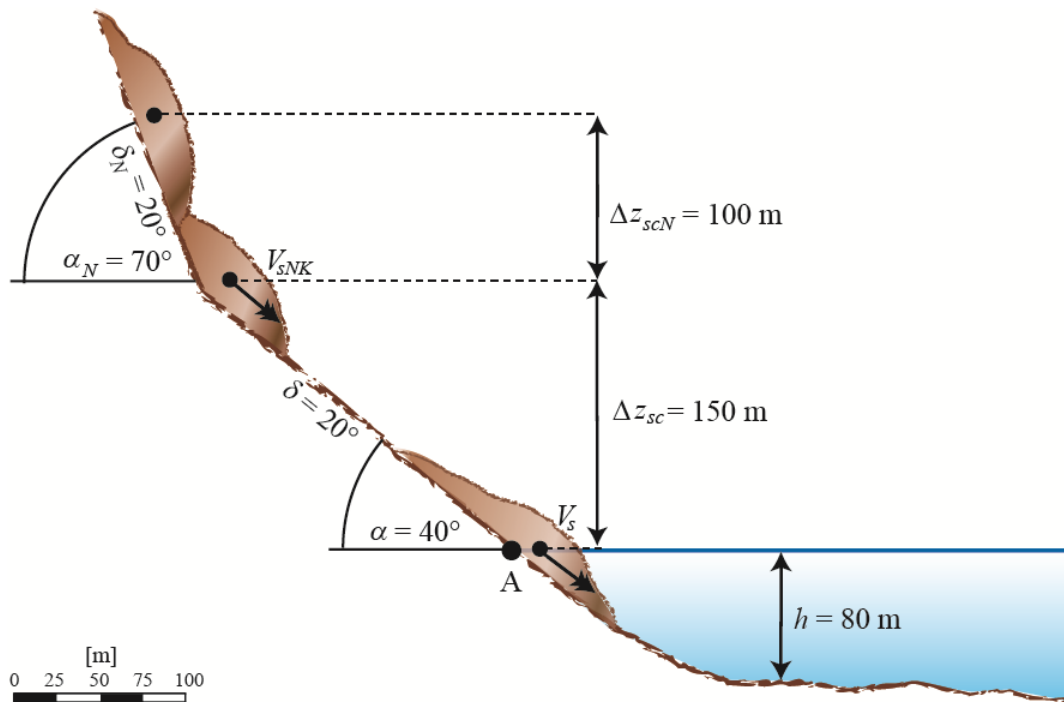


Figure 5-2 Parameters for the calculation of the slide impact velocity V_s .

Table 5-1 Governing parameters for the slide impact velocity V_s according to Figure 5-2.

First slope section				Second slope section			
Term	Symbol	Unit	Value	Term	Symbol	Unit	Value
Drop height of centre	Δz_{scN}	[m]	100	Drop height of centre	Δz_{sc}	[m]	150
Dynamic bed friction angle	δ_N	[°]	20	Dynamic bed friction angle	δ	[°]	20
Hill slope angle	α_N	[°]	70	Hill slope angle	α	[°]	40

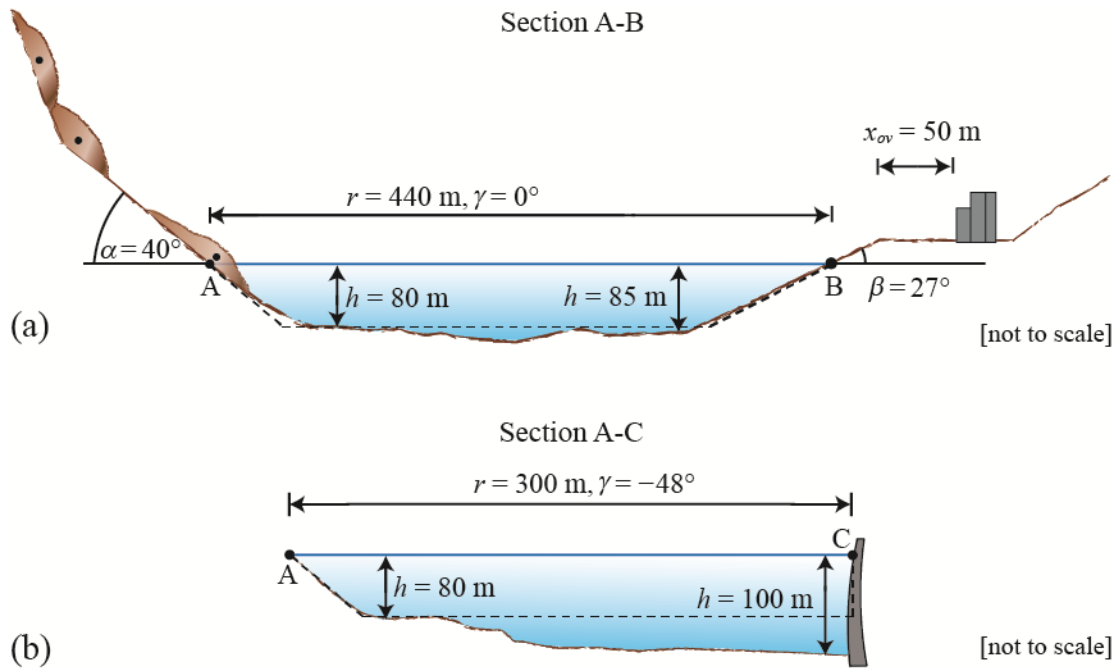


Figure 5-3 Sections for example 1 after Figure 5-1: (a) section A-B with rockslide and still water depth $h = 80$ m along the slide axis and (b) section A-C; the dashed lines indicate the idealised geometry for Step 1.

Table 5-2 Governing parameters for impulse wave generation and the effects on the opposite shore, as well as on the arch dam.

Term	Symbol	Unit	Value	Term	Symbol	Unit	Value
Still water depth (impact)	h	[m]	80	Bulk slide volume	V_s	[m ³]	220,000
Slide thickness	s	[m]	12	Bulk slide density	ρ_s	[kg/m ³]	1,700
Slide width	b	[m]	100	Bulk slide porosity	n	[%]	35
Slide impact velocity	V_s	[m/s]	58	Slide impact angle	α	[°]	40
Section A-B (shore)				Section A-C (dam)			
Radial distance	r	[m]	440	Radial distance	r	[m]	300
Wave propagation angle	γ	[°]	0	Wave propagation angle	γ	[°]	-48
Still water depth	h	[m]	85	Still water depth	h	[m]	100
Run-up angle	β	[°]	27	Run-up angle	β	[°]	90
Freeboard	f	[m]	10	Freeboard	f	[m]	4
Overland flow distance	x_{ov}	[m]	50	Crest width	b_K	[m]	8

5.1.2 Step 1

In this section, Step 1 is carried out, in accordance with Figure 3-1. The impulse wave propagates radially and completely freely. Hence, the wave parameters can be computed using the 3D equations for the reservoir of rectangular form (Subsection 3.2.1). The calculation proceeds in several partial steps:

- a) Dimensionless parameters and limitations check on the calculation of the wave generation and propagation

For optimum prediction with this computational procedure the dimensionless parameters of the prototype must be within the range of limitations for use of the calculation equations. The relevant dimensionless parameters and limitations (Subsection 3.2.4) are given in Table 5-3.

Table 5-3 Dimensionless parameters and limitations check for the calculation of the wave generation and propagation.

Term	Dimensionless parameter	Range	Satisfied?
Slide Froude number	$F = 58/(9.81 \cdot 80)^{0.5} = 2.07$	$0.40 \leq F \leq 3.40$	Yes
Relative slide thickness	$S = 12/80 = 0.15$	$0.15 \leq S \leq 0.60$	Yes
Relative slide density	$D = 1,700/1,000 = 1.70$	$(0.59 \leq D \leq 1.72)$	(Yes)
Relative slide volume	$V = 220,000/(100 \cdot 80^2) = 0.34$	$0.187 \leq V \leq 0.750$	Yes
Relative slide mass	$M = 1,700 \cdot 220,000/(1000 \cdot 100 \cdot 80^2) = 0.58$	$0.25 \leq M \leq 1.00$	Yes
Bulk slide porosity	$n = 35\%$	$(30.7 \leq n \leq 43.3)$	(Yes)
Relative slide width	$B = 100/80 = 1.25$	$0.83 \leq B \leq 5.00$	Yes
Slide impact angle	$\alpha = 40^\circ$	$30^\circ \leq \alpha \leq 90^\circ$	Yes
Impulse product parameter	$P = 2.07 \cdot 0.15^{0.5} \cdot 0.58^{0.25} \cdot \cos[6/7(40^\circ)]^{0.5} = 0.64$	$0.13 \leq P \leq 2.08$	Yes
Relative radial distance (A-B)	$r/h = 300/80 = 3.75$	$1 \leq r/h \leq 16$	Yes
Relative radial distance (A-C)	$r/h = 440/80 = 5.5$	$1 \leq r/h \leq 16$	Yes
Wave propagation angle (A-B)	$\gamma = 0^\circ$	$-90^\circ \leq \gamma \leq 90^\circ$	Yes
Wave propagation angle (A-C)	$\gamma = -48^\circ$	$-90^\circ \leq \gamma \leq 90^\circ$	Yes

In the wave generation phase all limitations are satisfied. The limitation ranges of the relative slide density D and the bulk slide porosity n are given in brackets, as these are within the slide density's extended parameter range of the impulse product parameter P for 3D wave generation and propagation (Subsection 3.2.4.3).

b) Calculation of wave generation and propagation

Wave generation will be analysed using the 3D method, as described in Subsection 3.2.4.3, for which important variables are the wave amplitudes a_{c1} , a_{t1} and a_{c2} , the first wave height H_1 , and the first wave crest celerity c_{c1} . The impact radius $r_{0,0^\circ}$ and $r_{0,90^\circ}$ as well as the initial wave amplitudes $a_{0,c1}$, $a_{0,t1}$ and $a_{0,c2}$ are independent from the considered wave propagation directions for both sections A-B and A-C and are determined as

$$r_{0,0^\circ} = 2.5 \left(P \left(\frac{b}{h} \right) \cos \alpha_{eff} \right)^{0.25} h \quad \text{Eq. (3.22)}$$

$$r_{0,0^\circ} = 2.5 \left(0.64 \left(\frac{100}{80} \right) \cos \left(\frac{6}{7} 40^\circ \right) \right)^{0.25} 80 = 180 \text{ m}$$

$$r_{0,90^\circ} = \left(\frac{b}{2} \right) + 1.5 \left(P \cos \alpha_{eff} \right)^{0.25} h \quad \text{Eq. (3.23)}$$

$$r_{0,90^\circ} = \left(\frac{100}{2} \right) + 1.5 \left(0.64 \cos \left(\frac{6}{7} 40^\circ \right) \right)^{0.25} 80 = 152 \text{ m}$$

$$a_{0,c1} = 0.2P^{0.5} \left(\frac{b}{h} \right)^{0.75} (\cos \alpha_{eff})^{0.25} h \quad \text{Eq. (3.26)}$$

$$a_{0,c1} = 0.2 \cdot 0.64^{0.5} \left(\frac{100}{80} \right)^{0.75} \left(\cos \left(\frac{6}{7} 40^\circ \right) \right)^{0.25} 80 = 14.4 \text{ m}$$

$$a_{0,t1} = 0.35 \left(P \left(\frac{b}{h} \right) \cos \alpha_{eff} \right)^{0.5} h \quad \text{Eq. (3.27)}$$

$$a_{0,t1} = 0.35 \left(0.64 \left(\frac{100}{80} \right) \cos \left(\frac{6}{7} 40^\circ \right) \right)^{0.5} 80 = 22.7 \text{ m}$$

$$a_{0,c2} = 0.14 \left(P \left(\frac{b}{h} \right) \cos \alpha_{eff} \right)^{0.25} h \quad \text{Eq. (3.28)}$$

$$a_{0,c2} = 0.14 \left(0.64 \left(\frac{100}{80} \right) \cos \left(\frac{6}{7} 40^\circ \right) \right)^{0.25} 80 = 10.1 \text{ m}$$

Section A-B

$$r_0(\gamma) = \sqrt{\frac{r_{0,0^\circ}^2 r_{0,90^\circ}^2}{r_{0,0^\circ}^2 \sin^2 \gamma + r_{0,90^\circ}^2 \cos^2 \gamma}} \quad \text{Eq. (3.24)}$$

$$r_0(0^\circ) = \sqrt{\frac{180^2 152^2}{180^2 \sin^2 0^\circ + 152^2 \cos^2 0^\circ}} = r_{0,0^\circ} = 180 \text{ m}$$

$$r^* = r - r_0 \quad \text{Eq. (3.25)}$$

$$r^* = 440 - 180 = 260 \text{ m}$$

$$a_{c1}(r^*, \gamma) = a_{0,c1} \exp \left[-0.4 \left(\frac{a_{0,c1}}{h} \right)^{-0.3} \sqrt{\frac{r^*}{h}} \right] \left[\operatorname{sech} \left(3.2 \frac{\gamma}{90^\circ} \right) \right]^{\cos \alpha_{eff} \exp \left(-0.15 \sqrt{\frac{r^*}{h}} \right)} \quad \text{Eq. (3.29)}$$

$$a_{c1} = 14.4 \exp \left[-0.4 \left(\frac{14.4}{80} \right)^{-0.3} \sqrt{\frac{260}{80}} \right] \left[\operatorname{sech} \left(3.2 \frac{0^\circ}{90^\circ} \right) \right]^{\cos \left(\frac{6}{7} 40^\circ \right) \exp \left(-0.15 \sqrt{\frac{260}{80}} \right)} = 4.3 \text{ m}$$

$$a_{t1}(r^*, \gamma) = a_{0,t1} \exp \left[-0.4 \left(\frac{a_{0,t1}}{h} \right)^{-0.3} \sqrt{\frac{r^*}{h}} \right] \left[\operatorname{sech} \left(3.6 \frac{\gamma}{90^\circ} \right) \right]^{\cos \alpha_{eff} \exp \left(-0.15 \sqrt{\frac{r^*}{h}} \right)} \quad \text{Eq. (3.30)}$$

$$a_{t1} = 22.7 \exp \left[-0.4 \left(\frac{22.7}{80} \right)^{-0.3} \sqrt{\frac{260}{80}} \right] \left[\operatorname{sech} \left(3.6 \frac{0^\circ}{90^\circ} \right) \right]^{\cos \left(\frac{6}{7} 40^\circ \right) \exp \left(-0.15 \sqrt{\frac{260}{80}} \right)} = 7.9 \text{ m}$$

$$a_{c2}(r^*, \gamma) = a_{0,c2} \exp \left[-0.1 \left(\frac{a_{0,c2}}{h} \right)^{-0.3} \sqrt{\frac{r^*}{h}} \right] \left[\operatorname{sech} \left(3 \frac{\gamma}{90^\circ} \right) \right]^{\cos \alpha_{eff} \exp \left(-0.15 \sqrt{\frac{r^*}{h}} \right)} \quad \text{Eq. (3.31)}$$

$$a_{c2} = 10.1 \exp \left[-0.1 \left(\frac{10.1}{80} \right)^{-0.3} \sqrt{\frac{260}{80}} \right] \left[\operatorname{sech} \left(3 \frac{0^\circ}{90^\circ} \right) \right]^{\cos \left(\frac{6}{7} 40^\circ \right) \exp \left(-0.15 \sqrt{\frac{260}{80}} \right)} = 7.2 \text{ m}$$

Section A-C

$$r_0(\gamma) = \sqrt{\frac{r_{0,0^\circ}^2 r_{0,90^\circ}^2}{r_{0,0^\circ}^2 \sin^2 \gamma + r_{0,90^\circ}^2 \cos^2 \gamma}} \quad \text{Eq. (3.24)}$$

$$r_0(-48^\circ) = \sqrt{\frac{180^2 152^2}{180^2 \sin^2(-48^\circ) + 152^2 \cos^2(-48^\circ)}} = 163 \text{ m}$$

$$r^* = r - r_0 \quad \text{Eq. (3.25)}$$

$$r^* = 300 - 163 = 137 \text{ m}$$

$$a_{c1}(r^*, \gamma) = a_{0,c1} \exp \left[-0.4 \left(\frac{a_{0,c1}}{h} \right)^{-0.3} \sqrt{\frac{r^*}{h}} \right] \left[\operatorname{sech} \left(3.2 \frac{\gamma}{90^\circ} \right) \right]^{\cos \alpha_{eff} \exp \left(-0.15 \sqrt{\frac{r^*}{h}} \right)} \quad \text{Eq. (3.29)}$$

$$a_{c1} = 14.4 \exp \left[-0.4 \left(\frac{14.4}{80} \right)^{-0.3} \sqrt{\frac{137}{80}} \right] \left[\operatorname{sech} \left(3.2 \frac{-48^\circ}{90^\circ} \right) \right]^{\cos \left(\frac{6}{7} 40^\circ \right) \exp \left(-0.15 \sqrt{\frac{137}{80}} \right)} = 2.9 \text{ m}$$

$$a_{t1}(r^*, \gamma) = a_{0,t1} \exp \left[-0.4 \left(\frac{a_{0,t1}}{h} \right)^{-0.3} \sqrt{\frac{r^*}{h}} \right] \left[\operatorname{sech} \left(3.6 \frac{\gamma}{90^\circ} \right) \right]^{\cos \alpha_{eff} \exp \left(-0.15 \sqrt{\frac{r^*}{h}} \right)} \quad \text{Eq. (3.30)}$$

$$a_{t1} = 22.7 \exp \left[-0.4 \left(\frac{22.7}{80} \right)^{-0.3} \sqrt{\frac{137}{80}} \right] \left[\operatorname{sech} \left(3.6 \frac{-48^\circ}{90^\circ} \right) \right]^{\cos \left(\frac{6}{7} 40^\circ \right) \exp \left(-0.15 \sqrt{\frac{137}{80}} \right)} = 4.5 \text{ m}$$

$$a_{c2}(r^*, \gamma) = a_{0,c2} \exp \left[-0.1 \left(\frac{a_{0,c2}}{h} \right)^{-0.3} \sqrt{\frac{r^*}{h}} \right] \left[\operatorname{sech} \left(3 \frac{\gamma}{90^\circ} \right) \right]^{\cos \alpha_{eff} \exp \left(-0.15 \sqrt{\frac{r^*}{h}} \right)} \quad \text{Eq. (3.31)}$$

$$a_{c2} = 10.1 \exp \left[-0.1 \left(\frac{10.1}{80} \right)^{-0.3} \sqrt{\frac{137}{80}} \right] \left[\operatorname{sech} \left(3 \frac{-48^\circ}{90^\circ} \right) \right]^{\cos \left(\frac{6}{7} 40^\circ \right) \exp \left(-0.15 \sqrt{\frac{137}{80}} \right)} = 4.2 \text{ m}$$

The largest wave amplitudes are to be expected on the slide axis $\gamma = 0^\circ$. Lateral to the slide axis $\gamma = 0^\circ$, the wave amplitudes decrease. At point B, the wave amplitudes are noticeably greater than at point C, even though the radial distance r on section A-C is shorter than for section A-B.

To determine the travel time of the first wave between the points A and B and between A and C (Figure 5-1), the first wave crest celerity c_{c1} has to be known, which is given with

$$c_{c1}(r^*, \gamma) = 0.95 \sqrt{g(h + a_{c1})} \quad \text{Eq. (3.32)}$$

Equation (3.32) yields the instantaneous wave crest celerity at a specific location (r^*, γ) . To estimate the travel time, a mean celerity for the overall propagation distance is selected. With $a_{0,c1} = 14.4$ m and $a_{c1}(260 \text{ m}, 0^\circ) = 4.3$ m, the mean (subscript m) first wave crest amplitude for section A-B is $a_{c1,m} = (14.4 + 4.3)/2 = 9.4$ m. With a mean still water depth $h_m = (80 + 85)/2 = 82.5$ m (Figure 5-3a), the mean wave crest celerity is

$$c_{c1,m} = 0.95 \sqrt{g(h_m + a_{c1,m})}$$

$$c_{c1,m} = 0.95 \sqrt{9.81(82.5 + 9.4)} = 28.5 \text{ m/s}$$

The impulse wave covers the distance $r = 440$ m to the shore in roughly $r/c = 440/28.5 = 15$ s.

For section A-C with $\gamma = -48^\circ$, the wave amplitude a_{c1} at r_0 needs to be computed. For $r^* = 0$, the exponential terms in Eq. (3.29) equal 1 and the equation simplifies to

$$a_{c1}(r^* = 0, \gamma) = a_{0,c1} \left[\operatorname{sech} \left(3.2 \frac{\gamma}{90^\circ} \right) \right]^{\cos \alpha_{eff}}$$

$$a_{c1}(0, -48^\circ) = 14.4 \left[\operatorname{sech} \left(3.2 \frac{-48^\circ}{90^\circ} \right) \right]^{\cos \left(\frac{6}{7} 40^\circ \right)} = 6.6 \text{ m}$$

With a mean still water depth $h_m = (80 + 100)/2 = 90$ m (Figure 5-3b) and a mean wave amplitude $a_{c1,m} = (6.6 + 2.9)/2 = 4.8$ m between point A and C, the mean wave celerity is

$$c_{c1,m} = 0.95 \sqrt{g(h_m + a_{c1,m})}$$

$$c_{c1,m} = 0.95 \sqrt{9.81(90 + 4.8)} = 29.0 \text{ m/s}$$

The impulse wave takes about $r/c = 300/29 = 10$ s to travel the 300 m from the impact location (point A) to the arch dam (point C).

c) Wave run-up including limitations check

With help of the wave parameters calculated in b), the dimensionless parameters for the arch dam as well as the run-up height R (Eq. 3.36) may be computed. The still water depth $h = 85$ m in front of the dam is thereby considered. Note, that the effect of shoaling may be taken into account in Step 2. For both sections, the second wave crest amplitudes a_{c2} are larger and are therefore considered for the estimation of R . As distinct from the case when waves run-up smooth and impermeable dams, the neglected governing parameters in Eq. (3.36), i.e. the permeability and roughness of the shore, may be relevant as they attenuate the run-up height R . The value obtained with Eq. (3.36) for point B at the shore thus tends to over-estimate the run-up height R . In Tables 5-4 and 5-5 compliance with the limiting parameters is verified and then the run-up height R is computed. To check the non-linearity limitation, the wave height H is approximated with $H = a_{c2} + a_{t1}$.

Point B

Table 5-4 Dimensionless parameters and limitations check for the calculation of wave run-up at point B.

Term	Dimensionless parameter	Range	Satisfied?
Relative wave crest amplitude	$\varepsilon = a_{c2}/h = 7.2/85 = 0.085$	$0.007 \leq \varepsilon \leq 0.69$	Yes
Non-linearity	$a_{c2}/H = 7.2/(7.2+7.9) = 0.48$	$0.57 \leq a/H \leq 1.04$	No
Run-up angle	$\beta = 27^\circ$	$10^\circ \leq \beta \leq 90^\circ$	Yes
Slope parameter	$S_o = 1.521(\tan 27^\circ / 0.085^{0.5}) = 2.7$	$S_o \geq 0.37$	Yes

$$R = 2a \exp(0.4\varepsilon) \left(\frac{90^\circ}{\beta} \right)^{0.2} \quad \text{Eq. (3.36)}$$

$$R = 2 \cdot 7.2 \exp\left(0.4 \frac{7.2}{85}\right) \left(\frac{90^\circ}{27^\circ} \right)^{0.2} = 19.0 \text{ m}$$

Point C

Table 5-5 Dimensionless parameters and limitations check for the calculation of wave run-up at point C.

Term	Dimensionless parameter	Range	Satisfied?
Relative wave crest amplitude	$\varepsilon = a_{c2}/h = 4.2/100 = 0.042$	$0.007 \leq \varepsilon \leq 0.69$	Yes
Non-linearity	$a_{c2}/H = 4.2/(4.2+4.5) = 0.48$	$0.57 \leq a/H \leq 1.04$	No
Run-up angle	$\beta = 90^\circ$	$10^\circ \leq \beta \leq 90^\circ$	Yes

$$R = 2a \exp(0.4\varepsilon) \left(\frac{90^\circ}{\beta} \right)^{0.2} \quad \text{Eq. (3.36)}$$

$$R = 2 \cdot 4.2 \exp\left(0.4 \frac{4.2}{100}\right) \left(\frac{90^\circ}{90^\circ}\right)^{0.2} = 8.5 \text{ m}$$

Only the non-linearity a/H exceeds the limitations for sections A-B and A-C. However, this may have just a small effect on the results. For section A-C there is no need to check the slope parameter as $S_o \rightarrow \infty$ for $\beta \rightarrow 90^\circ$ and no wave-breaking is expected. The impulse waves will, according to the preceding calculations, overtop the dam with a freeboard of $f = 4$ m at point C, since $R > f$.

e) Overland flow

As the freeboard of $f = 10$ m is smaller than the run-up height of $R = 19$ m at point B, a part of the impulse wave will transform to overland flow. New limitations govern the determination of the overland flow characteristics (Section 3.4):

Point B

Table 5-6 Dimensionless parameters and limitations check for the calculation of overland flow at point B.

Term	Dimensionless parameter	Range	Satisfied?
Relative wave crest amplitude	$\varepsilon = a_c/2h = 7.2/85 = 0.085$	$0.1 \leq \varepsilon \leq 0.7$	No
Relative freeboard	$f/h = 10/85 = 0.12$	$0.04 \leq f/h \leq 0.56$	Yes
Run-up angle	$\beta = 27^\circ$	$11^\circ \leq \beta \leq 34^\circ$	Yes
Overland flow distance	$x_{ov}/w = 50/(85+10) = 0.53$	$0 \leq x_{ov}/w \leq 10$	Yes

$$\varepsilon_{min} = \frac{f(\tan \beta)^{0.05}}{3h} \quad \text{Eq. (3.42)}$$

$$\varepsilon_{min} = \frac{10(\tan 27^\circ)^{0.05}}{3 \cdot 100} = 0.038$$

$$\varepsilon_{eff} = \varepsilon - \varepsilon_{min} = 0.085 - 0.038 = 0.05 \quad \text{Eq. (3.43)}$$

$$d_0 = \frac{(0.4 \tan \beta + 0.9) \varepsilon_{eff}}{\left(\frac{w}{h}\right)^{0.45 \cot \beta}} h \quad \text{Eq. (3.45)}$$

$$d_0 = \frac{(0.4 \tan 27^\circ + 0.9) 0.05}{\left(\frac{85+10}{85}\right)^{0.45 \cot 27^\circ}} 85 = 4.0 \text{ m}$$

$$x_{max}^* = \frac{x_{ov}}{w} \left(\frac{w}{h}\right)^{5.3 \tan \beta - 1.4} \quad \text{Eq. (3.47)}$$

$$x_{max}^* = \left(\frac{50}{85+10} \right) \left(\frac{85+10}{85} \right)^{5.3 \tan 27^\circ - 1.4} = 0.6$$

$$d_{max} = d_0 \left\{ 1 - \tanh \left[0.54 \left(x_{max}^* \right)^{0.39} \right] \right\} \quad \text{Eq. (3.46)}$$

$$d_{max} = 4.0 \left\{ 1 - \tanh \left[0.54 (0.6)^{0.39} \right] \right\} = 2.3 \text{ m}$$

$$v_{f,max} = 1.6c \tanh \left[2.2 \left(\varepsilon_{eff} \frac{h}{w} \right)^{0.75} \right] \quad \text{Eq. (3.49)}$$

$$v_{f,max} = 1.6\sqrt{9.81(85+7.2)} \tanh \left[2.2 \left(0.05 \frac{85}{85+10} \right)^{0.75} \right] = 9.7 \text{ m/s}$$

The maximum flow depth at the transition point from the shore slope to the horizontal foreland is $d_0 = 4.0$ m. After $x_{ov} = 50$ m, the maximum flow depth reduces to $d_{max} = 2.3$ m. The estimated maximum flow front velocity is $v_{f,max} = 9.7$ m/s. However, since $x_{ov}/w < 5$, this value represents an extreme value and is expected to be lower at the infrastructure buildings at $x_{ov} = 50$ m (Subsection 3.4.5).

The relative wave crest amplitude ε is slightly smaller than the limitation range given in Table 5-6. Given that the deviation from the lower limit is small, only minor effects on the results are expected.

e) Wave overtopping

As the dam's freeboard of $f = 4$ m is smaller than the run-up height of $R = 8.5$ m at point C, a part of the impulse wave will overtop the dam. New limitations govern the determination of the overtopping characteristics (Subsection 3.3.4):

Point C

Table 5-7 Dimensionless parameters and limitations check for the calculation of wave overtopping at point C.

Term	Dimensionless parameter	Range	Satisfied?
Relative wave crest amplitude	$\varepsilon = a_c/h = 4.2/100 = 0.042$	$0.013 \leq \varepsilon \leq 0.700$	Yes
Relative effective wave amplitude	$a_w/b_K = (4.2 - 4.0)/8 = 0.025$	$0.02 \leq a_w/b_K \leq 130$	Yes
Relative still water depth	$h/w = 100/104 = 0.96$	$0.67 \leq h/w \leq 1.00$	Yes
Dam angle	$\beta = 90^\circ$	$18.4^\circ \leq \beta \leq 90^\circ$	Yes
Non-linearity	$a_c/H = 4.2/(4.2+4.5) = 0.48$	$0.63 \leq a/H \leq 1.00$	No
Relative crest width	$b_K/w = 8/(100+4) = 0.08$	$0.002 \leq b_K/w \leq 0.530$	Yes

$$\mu = 1.35 \left(\frac{a}{H} \right)^{1.5} \left[\varepsilon \left(\frac{h}{w} \right)^{(2/\varepsilon)(\beta/90^\circ)^{0.25}} \left(\frac{a_w}{b_K} \right)^{0.12} \right]^{0.7} h^2 \quad \text{Eq. (3.38)}$$

$$\mathcal{F} = 1.35 \left(\frac{4.2}{4.2 + 4.5} \right)^{1.5} \left[0.042 \left(\frac{100}{100 + 4} \right)^{(2/0.042)(90^\circ/90^\circ)^{0.25}} \left(\frac{4.2 - 4.0}{8} \right)^{0.12} \right]^{0.7} 100^2$$

$$\mathcal{F} = 93 \text{ m}^3/\text{m}$$

$$d_0 = 1.32 \left[\varepsilon \left(\frac{h}{w} \right)^{4[(\beta/90^\circ)^{-0.21} - \varepsilon]} \left(\frac{\beta}{90^\circ} \right)^{0.16} \right] w \quad \text{Eq. (3.39)}$$

$$d_0 = 1.32 \left[0.042 \left(\frac{100}{100 + 4} \right)^{4[(90^\circ/90^\circ)^{-0.21} - 0.042]} \left(\frac{90^\circ}{90^\circ} \right)^{0.16} \right] (100 + 4) = 4.9 \text{ m}$$

$$t_O = \frac{1}{0.15} \left[\varepsilon^{0.2} \left(\frac{h}{w} \right)^{(-0.9/\varepsilon)(\beta/90^\circ)^{0.4}} \right]^{-1.9} (w/g)^{0.5} \quad \text{Eq. (3.40)}$$

$$t_O = \frac{1}{0.15} \left[0.042^{0.2} \left(\frac{100}{100 + 4} \right)^{(-0.9/0.042)(90^\circ/90^\circ)^{0.4}} \right]^{-1.9} \left(\frac{100 + 4}{9.81} \right)^{0.5} = 14.5 \text{ s}$$

The average discharge per unit length dam crest is thus

$$q_m = \mathcal{F}/t_O \quad \text{Eq. (3.41)}$$

$$q_{0m} = 93/14.5 = 6.4 \text{ m}^2/\text{s}.$$

The maximum discharge per unit length dam crest is according to Subsection 3.3.4 $q_M \approx 2 \cdot q_m = 2 \cdot 6.4 = 12.8 \text{ m}^2/\text{s}$, but this occurs for only a few seconds. From Table 5-7 it may be seen that the non-linearity limitation criterion $0.63 \leq a/H \leq 1.00$ is not satisfied. Analogous to the run-up height R , this may have just a small effect on the results. In any case, the equations describing the overtopping processes are based on solitary wave experiments and may therefore be regarded as conservative approximations.

f) Force effect on the arch dam during overtopping

The total horizontal force component at point C with $\varepsilon = a/h = 0.11$ is

$$F_{tot,h} = [1 - 1.5(a/h)]^{1/6} F_{hs,h} \quad \text{Eq. (3.54)}$$

$$F_{tot,h} = [1 - 1.5(4.2/100)]^{1/6} (1/2) 1,000 \cdot 9.81 (2 \cdot 4.2 + 100)^2 = 56.9 \cdot 10^6 \text{ N/m}.$$

As some of the impulse wave will overtop the arch dam, the structure does not receive the full horizontal force component, as shown in Figure 3-11(b). The reduced horizontal force component can be computed via the pressure at dam crest p_K given by

$$p_K = \frac{2F_{tot,h}}{(2a+h)^2} (2a-f) \quad \text{Eq. (3.56)}$$

$$p_K = \frac{2 \cdot 56.9 \cdot 10^6}{(2 \cdot 4.2 + 100)^2} (2 \cdot 4.2 - 4) = 41,879 \text{ N/m}^2.$$

The reduced total horizontal force component $K_{tot,h,red}$ per unit length dam crest resulting from an impulse wave and hydrostatic pressure is

$$F_{tot,h,red} = \frac{(h+f)}{2} \left[p_K + \frac{2F_{tot,h}}{2a+h} \right] \quad \text{Eq. (3.57)}$$

$$K_{tot,h,red} = \frac{(100+4)}{2} \left[41,879 + \frac{2 \cdot 56.9 \cdot 10^6}{2 \cdot 4.2 + 100} \right] = 56.8 \cdot 10^6 \text{ N/m}.$$

The elevation $z_{K,tot,h,red}$ of the resultant of $K_{tot,h,red}$ is

$$z_{K,tot,h,red} = \frac{\left[2F_{tot,h} / (2a+h) - p_K \right] \frac{(h+f)^2}{6} + p_K \frac{(h+f)^2}{2}}{\left[2F_{tot,h} / (2a+h) - p_K \right] \frac{h+f}{2} + p_K (h+f)} \quad \text{Eq. (3.58)}$$

$$\begin{aligned} z_{K,tot,h,red} &= \frac{\left[2 \cdot 56.9 \cdot 10^6 / (2 \cdot 4.2 + 100) - 41,879 \right] \frac{(100+4)^2}{6} + 41,879 \frac{(100+4)^2}{2}}{\left[2 \cdot 56.9 \cdot 10^6 / (2 \cdot 4.2 + 100) - 41,879 \right] \frac{100+4}{2} + 41,879 (100+4)} \\ &= 36 \text{ m}. \end{aligned}$$

If $F_{tot,h,red}$ is reduced by the horizontal force component $F_{RW,h}$ resulting from hydrostatic pressure then the additional horizontal force component resulting only from the impulse wave is obtained as

$$\begin{aligned} \Delta F_h &= F_{tot,h,red} - F_{RW,h} = F_{tot,h,red} - \rho_w g h^2 / 2 \quad \text{Eq. (3.57) - Eq. (3.52)} \\ \Delta F_h &= 56.9 \cdot 10^6 - 1,000 \cdot 9.81 \cdot 100^2 / 2 = 7.9 \cdot 10^6 \text{ N/m}. \end{aligned}$$

The additional horizontal force component ΔF_h resulting only from the impulse wave is relative to the hydrostatic effect $7.9 \cdot 10^6 / [1,000 \cdot 9.81 \cdot 100^2 / 2] = 16\%$. This additional impulse wave force component acts on the arch dam for only a short time, typically for a few seconds. The total horizontal force component $F_{tot,h}$ is only marginally reduced by the overtopping depth over the dam crest, which is $d_0 = 4.9$ m. Furthermore, no vertical force component is created as the upstream dam face is vertical (Subsection 3.5.2).

g) Required freeboard to prevent overtopping

The required freeboard f sufficient to ensure that the arch dam is not overtopped by the impulse wave, can now be determined. The run-up height at point C is equal to $R = 8.5$ m, whereas the freeboard is 4 m. Whether emergency drawdown of the reservoir by the difference $R - f = 4.5$ m will be adequate to prevent overtopping, is difficult to judge before a new calculation is made. This is because, when the reservoir level is lowered,

certain governing parameters such as the slide impact velocity V_s may change in an unfavourable sense. In this example, lowering the reservoir level by 10 m is assumed, giving a new freeboard of $f = 14$ m, and all calculations for section A-C have then to be repeated.

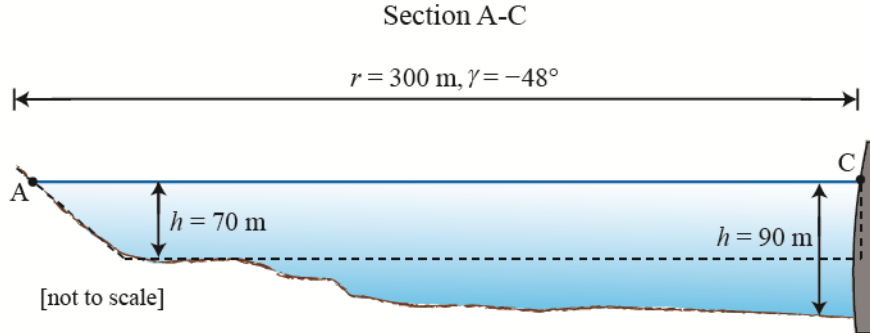


Figure 5-4 Section A-C after 10 m emergency drawdown of the reservoir and still water depth $h = 70$ m on the slide axis; the dashed line indicates the idealised geometry for Step 1.

The new slide impact velocity is

$$V_s = \sqrt{V_{sNK}^2 + 2g\Delta z_{sc}(1 - \tan \delta \cot \alpha)} \quad \text{after Eqs. (3.2), (3.5) and (3.9)}$$

$$V_s = \sqrt{41.3^2 + 2 \cdot 9.81 \cdot 160(1 - \tan 20^\circ \cot 40^\circ)} = 59.0 \text{ m/s.}$$

New dimensionless parameters (step a):

$F = 2.25$, $S = 0.17$, $D = 1.70$, $V = 0.45$, $M = 0.76$, $n = 35\%$, $B = 1.43$, $\alpha = 40^\circ$, $P = 0.79$, $r/h = 4.3$ and $\gamma \approx -48^\circ$. The limitations of the parameters in the impact zone are therefore still satisfied.

New wave parameters (step b):

$$r_{0,0^\circ} = 2.5 \left(P \left(\frac{b}{h} \right) \cos \alpha_{eff} \right)^{0.25} h \quad \text{Eq. (3.22)}$$

$$r_{0,0^\circ} = 2.5 \left(0.79 \left(\frac{100}{70} \right) \cos \left(\frac{6}{7} 40^\circ \right) \right)^{0.25} 70 = 172 \text{ m}$$

$$r_{0,90^\circ} = \left(\frac{b}{2} \right) + 1.5 \left(P \cos \alpha_{eff} \right)^{0.25} h \quad \text{Eq. (3.23)}$$

$$r_{0,90^\circ} = \left(\frac{100}{2} \right) + 1.5 \left(0.79 \cos \left(\frac{6}{7} 40^\circ \right) \right)^{0.25} 70 = 144 \text{ m}$$

$$r_0(\gamma) = \sqrt{\frac{r_{0,0^\circ}^2 r_{0,90^\circ}^2}{r_{0,0^\circ}^2 \sin^2 \gamma + r_{0,90^\circ}^2 \cos^2 \gamma}} \quad \text{Eq. (3.24)}$$

$$r_0(-48^\circ) = \sqrt{\frac{172^2 144^2}{172^2 \sin^2(-48^\circ) + 144^2 \cos^2(-48^\circ)}} = 155 \text{ m}$$

$$r^* = r - r_0 \quad \text{Eq. (3.25)}$$

$$r^* = 300 - 155 = 145 \text{ m}$$

$$a_{0,c1} = 0.2 \mathbf{P}^{0.5} \left(\frac{b}{h} \right)^{0.75} (\cos \alpha_{eff})^{0.25} h \quad \text{Eq. (3.26)}$$

$$a_{0,c1} = 0.2 \cdot 0.79^{0.5} \left(\frac{100}{70} \right)^{0.75} \left(\cos \left(\frac{6}{7} 40^\circ \right) \right)^{0.25} 70 = 15.5 \text{ m}$$

$$a_{0,t1} = 0.35 \left(\mathbf{P} \left(\frac{b}{h} \right) \cos \alpha_{eff} \right)^{0.5} h \quad \text{Eq. (3.27)}$$

$$a_{0,t1} = 0.35 \left(0.79 \left(\frac{100}{70} \right) \cos \left(\frac{6}{7} 40^\circ \right) \right)^{0.5} 70 = 23.7 \text{ m}$$

$$a_{0,c2} = 0.14 \left(\mathbf{P} \left(\frac{b}{h} \right) \cos \alpha_{eff} \right)^{0.25} h \quad \text{Eq. (3.28)}$$

$$a_{0,c2} = 0.14 \left(0.64 \left(\frac{100}{80} \right) \cos \left(\frac{6}{7} 40^\circ \right) \right)^{0.25} 80 = 9.6 \text{ m}$$

$$a_{c1}(r^*, \gamma) = a_{0,c1} \exp \left[-0.4 \left(\frac{a_{0,c1}}{h} \right)^{-0.3} \sqrt{\frac{r^*}{h}} \right] \left[\operatorname{sech} \left(3.2 \frac{\gamma}{90^\circ} \right) \right]^{\cos \alpha_{eff} \exp \left(-0.15 \sqrt{\frac{r^*}{h}} \right)} \quad \text{Eq. (3.29)}$$

$$a_{c1} = 15.5 \exp \left[-0.4 \left(\frac{15.5}{70} \right)^{-0.3} \sqrt{\frac{145}{70}} \right] \left[\operatorname{sech} \left(3.2 \frac{-48^\circ}{90^\circ} \right) \right]^{\cos \left(\frac{6}{7} 40^\circ \right) \exp \left(-0.15 \sqrt{\frac{145}{70}} \right)} = 3.1 \text{ m}$$

$$a_{t1}(r^*, \gamma) = a_{0,t1} \exp \left[-0.4 \left(\frac{a_{0,t1}}{h} \right)^{-0.3} \sqrt{\frac{r^*}{h}} \right] \left[\operatorname{sech} \left(3.6 \frac{\gamma}{90^\circ} \right) \right]^{\cos \alpha_{eff} \exp \left(-0.15 \sqrt{\frac{r^*}{h}} \right)} \quad \text{Eq. (3.30)}$$

$$a_{c1} = 23.7 \exp \left[-0.4 \left(\frac{23.7}{70} \right)^{-0.3} \sqrt{\frac{145}{70}} \right] \left[\operatorname{sech} \left(3.6 \frac{-48^\circ}{90^\circ} \right) \right]^{\cos \left(\frac{6}{7} 40^\circ \right) \exp \left(-0.15 \sqrt{\frac{145}{70}} \right)} = 4.7 \text{ m}$$

$$a_{c2}(r^*, \gamma) = a_{0,c2} \exp \left[-0.1 \left(\frac{a_{0,c2}}{h} \right)^{-0.3} \sqrt{\frac{r^*}{h}} \right] \left[\operatorname{sech} \left(3 \frac{\gamma}{90^\circ} \right) \right]^{\cos \alpha_{eff} \exp \left(-0.15 \sqrt{\frac{r^*}{h}} \right)} \quad \text{Eq. (3.31)}$$

$$a_{c2} = 9.6 \exp \left[-0.1 \left(\frac{9.6}{70} \right)^{-0.3} \sqrt{\frac{145}{70}} \right] \left[\operatorname{sech} \left(3 \frac{-48^\circ}{90^\circ} \right) \right]^{\cos \left(\frac{6}{7} 40^\circ \right) \exp \left(-0.15 \sqrt{\frac{145}{70}} \right)} = 4.0 \text{ m}$$

New wave run-up height considering the second wave crest amplitude a_{c2} (step c):

$$R = 2a \exp(0.4\varepsilon) \left(\frac{90^\circ}{\beta} \right)^{0.2} \quad \text{Eq. (3.36)}$$

$$R = 2 \cdot 4.0 \exp \left(0.4 \frac{4.0}{90} \right) \left(\frac{90^\circ}{90^\circ} \right)^{0.2} = 8.0 \text{ m}$$

Table 5-8 Dimensionless parameters and limitations check for the calculation of wave run-up at point C, following drawdown by 10 m.

Term	Dimensionless parameter	Range	Satisfied?
Relative wave crest amplitude	$\varepsilon = a_{c2}/h = 4.0/90 = 0.044$	$0.007 \leq \varepsilon \leq 0.69$	Yes
Non-linearity	$a_{c2}/H = 4.0/(4.0+4.7) = 0.46$	$0.57 \leq a/H \leq 1.04$	No
Run-up angle	$\beta = 90^\circ$	$10^\circ \leq \beta \leq 90^\circ$	Yes

Wave overtopping (step e):

For $R = 8.0 \text{ m} < f = 14 \text{ m}$, overtopping by an impulse wave after Step 1 is improbable. The assessment of Step 2 is given in Subsection 5.1.3.

New force effect (step f):

The horizontal force components $F_{tot,h}$ and ΔF_h are

$$F_{tot,h} = [1 - 1.5(a/h)]^{1/6} F_{hs,h} \quad \text{Eq. (3.54)}$$

$$F_{tot,h} = [1 - 1.5(4.0/90)]^{1/6} \cdot 0.5 \cdot 1,000 \cdot 9.81 (2 \cdot 4.0 + 90)^2 = 46.5 \cdot 10^6 \text{ N/m},$$

$$\Delta F_h = F_{tot,h} - F_{RW,h} = F_{tot,h} - \rho_w g h^2 / 2 \quad \text{Eq. (3.54) - Eq. (3.52)}$$

$$\Delta F_h = 46.5 \cdot 10^6 - 1,000 \cdot 9.81 \cdot 90^2 / 2 = 6.8 \cdot 10^6 \text{ N/m}.$$

The elevation $z_{K,tot,h}$ of the resultant of $F_{tot,h}$ is located at $(2a + h)/3 = (2 \cdot 4.0 + 90)/3 = 33$ m (Subsection 3.5.2). The additional horizontal force component ΔF_h resulting from impulse wave is $6.8 \cdot 10^6 / (0.5 \cdot 1,000 \cdot 9.81 \cdot 45^2) = 17\%$ relative to the hydrostatic effect.

The equations used in this section are based on laboratory test results with some having a high degree of scatter (Section 4.7). When drawing down the reservoir, therefore, a safety allowance should be allowed for. Decisive is now Step 2, described in Subsection 5.1.3.

5.1.3 Step 2

Basically, the characteristics of an impulse wave can be relatively well predicted from the reservoir geometry shown in Figure 5-1 with the help of generally applicable equations, as the reservoir geometry allows freely, radial wave propagation in 3D according to extreme case (b) (Subsection 3.2.1).

In the following section, the parameters *after* reservoir drawdown are applied. The deviations discussed below relate to the wave amplitudes a_{c1} , a_{t1} , and a_{c2} , or directly to the run-up height R . Compared with Step 1 as shown in Figure 3-1, the following phenomena could lead to deviations:

- Exceeding of the limitations
- Solid body movement instead of granular slide
- Ice cover
- Volumetric displacement due to rockfall
- Reflection
- Shoaling
- Constriction

The *limitations* relating to the wave's non-linearity a/H for points B and C, as well as those for the calculation of the overland flow, are not satisfied. As the effect of this is not known, the uncertainty of the results will increase.

How big will the largest impulse wave be if the slide impacts into the reservoir as a solid body? This might result in a higher impulse wave, compared with the modelled granular slide in Step 1. The solid slide is not expected to stop abruptly on the given bathymetry and the underwater slide propagation is therefore similar to granular slides (Figure 5-3). If Figure 4-11(c) is applied for the amplitude $a_{c2} = 4.0$ m in front of the arch dam after drawdown, an increase of impulse wave amplitudes between 30% and 75% may be expected compared with the calculation in Step 1 (solid line in Figure 4-11c), i.e. $a_{c2} = 5.2 \dots 7.0$ m.

The *ice cover* of 0.25 m thickness will be pierced by the slide. As the ice sheet is lifted by the wave crest it will break up under its own weight, so that resulting decay of the impulse wave will only be insignificant (Section 4.3).

The reservoir surface area is about $2.7 \cdot 10^5 \text{ m}^2$ (Figure 5-1). The reservoir water level will rise as a result of the *volumetric displacement* by the bulk slide mass of $V_s = 220,000 \text{ m}^3$ by about $(220,000 \cdot 0.65)/270,000 \approx 0.5 \text{ m}$, if the bulk slide porosity $n = 35\%$ is accounted for.

Wave reflections also have no significant effect in Figure 5-1, as $a_R \leq a$ (Figure 4-2a), which is also valid for the wave height. In addition, the wave will be reflected perpendicular at point B (angle of incidence equals angle of reflection) and is not directed against the dam.

The wave crest celerity c_{c1} or c_{c2} show whether the impulse wave propagates as deep, intermediate or shallow-water wave. According to Eqs. (3.32) and (3.33), c_{c1} and c_{c2} reach approximately 95% and 70%, respectively, of the solitary wave celerity (Eq. 2.2). Therefore, the impulse wave behaves as an intermediate-water wave ($2 \leq L/h \leq 20$, $c > 0.4(gh)^{0.5}$; Section 2.1), and is partly influenced by the reservoir bed. An increase of the water depth leads to a decrease of the height or amplitude, respectively, of intermediate-water waves. This effect may be estimated for section A-C in Figure 5-4(b) by assuming a constant energy flux for shallow and intermediate-water waves (Section 4.2). The value of $a_{c2} = 4.0 \text{ m}$ was determined as the largest wave crest amplitude, providing $h = 70 \text{ m}$ remains constant as far as the arch dam. These values are marked with index 1. If the still water depth h is greater, some of the wave energy will spread over the additional water depth, and the wave amplitude will be reduced. Index 2 denotes the condition when $h = 70 \text{ m}$ (indicated by a dashed line in Figure 5-4b) changes to $h = 90 \text{ m}$. As the widths $b_1 = b_2$ remain roughly identical, the new wave amplitude a_2 at point C is given by

$$\frac{a_2}{a_1} = \left(\frac{h_1}{h_2} \right)^{1/4} \quad \text{for } b_1 = b_2 \quad \text{after Eq. (4.1)}$$

$$a_2 = a_1 \left(\frac{h_1}{h_2} \right)^{1/4} = 4.0 \left(\frac{70}{90} \right)^{1/4} = 3.8 \text{ m.}$$

Due to the increase of the still water depth from 70 to 90 m, the wave height close to the shore decreases from 4.0 m to 3.8 m, or by 5%. Close to the shore at point B (Figure 5-3a) the opposite occurs as the impulse wave height increases as a consequence of the shallower still water (Figure 4-2b). This effect is already accounted for in the run-up formula, as the shallower still water results from the underwater extension of the shore inclination with the run-up angle of $\beta = 27^\circ$.

Constriction of the dam abutments leads to an increase of the wave height and hence also of the run-up height. If, furthermore, the lateral flank near the abutments is inclined this leads to an additional increase of the run-up height. The narrowing and inclination of the flank, as shown in Figure 4-7, have an effect of about 30%.

In summary an increase of the still water depth h towards the arch dam results in a decrease of a and thus of R ; on the other hand, however, constriction and the lateral

flank inclination at the dam abutments, as well as the slide behaving as a solid body, may lead to a significant increase. The constriction ($\approx +30\%$) and the influence of the solid body ($\approx +30-75\%$) are dominant compared with the effect of the decrease of the still water depth ($\approx -5\%$). According to Eq. (3.36) the run-up height is at least double the wave amplitude. With $a_{c2} = 4.0 \cdot (1.75 \cdot 1.30 \cdot 0.95) = 8.6$ m as the most unfavourable combination of these effects for a solid body slide, $2 \cdot 8.6$ m = 17.2 m > 14 m = f , the drawn down of 10 m might not be sufficient to prevent overtopping. Hence, to prevent any overtopping, the reservoir drawdown has to be increased further. The calculation has, therefore, to be repeated for the greater estimated drawdown value of about 15 m and the corresponding parameters.

5.1.4 Conclusions

The reservoir shape shown in Figure 5-1 is ideal for the computational procedure shown in Figure 3-1. The run-up height at the arch dam, as determined in Step 1, is $R = 8.5$ m, and exceeds the freeboard of $f = 4$ m (Table 5-2). An impulse wave will therefore overtop the dam crest. Following reservoir drawdown of 10 m (Figure 5-4) to give a freeboard of $f = 14$ m, the calculated run-up height according to Step 1 is $R = 8.0$ m.

The use of Step 2, as per Figure 3-1, leads to a run-up height R which is 115% greater than that calculated in Step 1. The reason for this is above all the fact that, as distinct from Step 1, the slide behaves as a solid body, but also the greater run-up height in the dam abutments. In order to prevent dam overtopping, the reservoir level must be lowered a further 5 m, to give a total freeboard of $f = 19$ m. Whether overtopping will be avoided with the new value of $f = 19$ m has to be proven with a new calculation as well as the choice of suitable safety allowance (Section 4.7).

The additional horizontal force component on the dam resulting from impulse wave is of the order of 17% of the force component due to hydrostatic pressure. However, this additional force only acts for a few seconds.

5.2 Example 2

5.2.1 Problem description and governing parameters

Figure 5-5 shows the reservoir geometry for example 2. An icefall threatens to impact into an artificial reservoir at point A. The effects on the embankment dam of the impulse wave generated by the ice mass and the extent to which the reservoir should be drawn down to avoid dam overtopping have to be determined. On impact with the reservoir the icefall will have disintegrated to a granular material. The freeboard is $f = 10$ m. The reservoir sections, which are shown in Figure 5-5 as dashed lines, are presented in Figure 5-7.

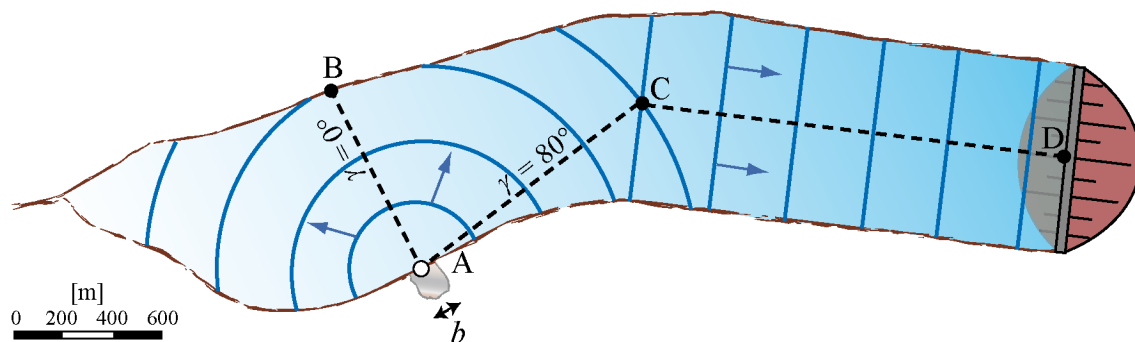


Figure 5-5 Reservoir geometry for example 2 with impacting icefall at point A; the reservoir is impounded by an embankment dam.

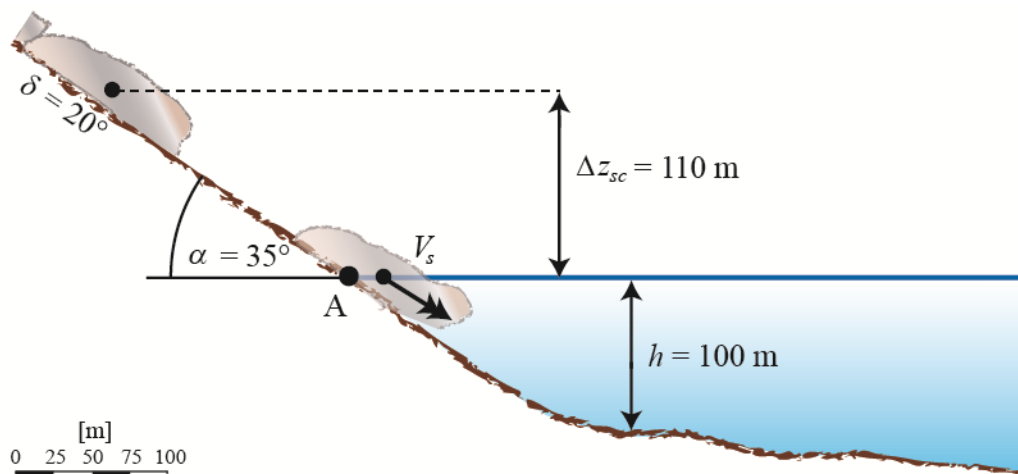


Figure 5-6 Parameters for the calculation of the slide impact velocity V_s .

For the reservoir geometry shown in Figure 5-5 the dam is not visible from the impact zone of the icefall. In the zone of the reservoir farthest from the dam the impulse waves may, however, propagate almost freely and radially (case b in Figure 3-2). Therefore, the wave parameters for point C will be determined using the 3D equations (Sub-

section 3.2.4.3). Between points C and D the reservoir geometry resembles that of a laboratory wave channel (case a in Figure 3-2). Therefore, between these two latter points, the analysis accounts for 2D wave decay, on the assumption that the waves will move parallel to the bank. This assumption is on the safe side (Subsection 5.2.3).

Using Eq. (3.5), the slide impact velocity V_s can be calculated for a drop height of the centre of gravity of the slide of $\Delta z_{sc} = 110$ m, a dynamic bed friction angle of $\delta = 20^\circ$ and a hill slope angle of $\alpha = 35^\circ$, as

$$V_s = \sqrt{2g\Delta z_{sc}(1 - \tan \delta \cot \alpha)} \quad \text{Eq. (3.5)}$$

$$V_s = \sqrt{2 \cdot 9.81 \cdot 110 (1 - \tan 20^\circ \cot 35^\circ)} = 32.2 \text{ m/s.}$$

The slide impact velocity V_s as well as all the other governing parameters such as those for wave generation and for the determination of the effects on the embankment dam and on the reservoir shore, are given in Table 5-9. The parameter b indicates the mean slide width and s the mean slide thickness, both in the impact zone. The bulk slide density ρ_s and the bulk slide volume V_s are also relative to the impact zone (Subsection 3.2.2). The governing still water depth h lies on the slide axis ($\gamma = 0^\circ$; Figure 3-3b).

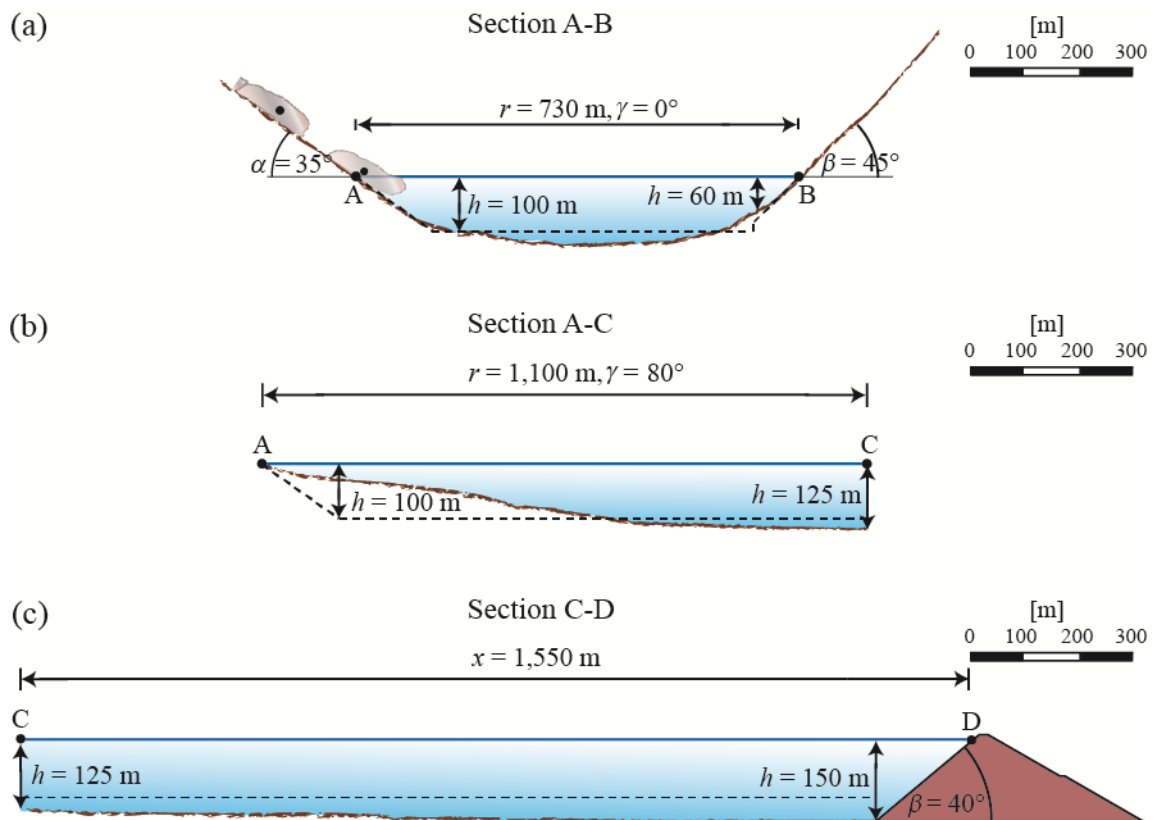


Figure 5-7 Sections for example 2, according to Figure 5-5: (a) section A-B with icefall and still water depth $h = 100$ m on the slide axis, (b) section A-C and (c) section C-D; the dashed lines indicate the idealised geometries for Step 1.

Table 5-9 Governing parameters for impulse wave generation, the effects on the opposite reservoir shore and on the embankment dam.

Term	Symbol	Unit	Value	Term	Symbol	Unit	Value
Still water depth (impact zone)	h	[m]	100	Bulk slide density	ρ_s	[kg/m ³]	500
Slide thickness	s	[m]	40	Bulk slide porosity	n	[%]	45
Slide width	b	[m]	120	Slide impact angle	α	[°]	35
Slide impact velocity	V_s	[m/s]	32	Crest width	b_K	[m]	12
Bulk slide volume	V_s	[m ³]	600,000	Freeboard	f	[m]	10
Section A-B				Section A-C			
Radial distance	r	[m]	730	Still water depth (impact zone)	h	[m]	100
Wave propagation angle	γ	[°]	0	Radial distance	r	[m]	1,100
Still water depth (run-up zone)	h	[m]	60	Wave propagation angle	γ	[°]	80
Run-up angle	β	[°]	45	Section C-D			
				Streamwise distance	x	[m]	1,550
				Still water depth (at dam)	h	[m]	150
				Run-up angle	β	[°]	40

5.2.2 Step 1

Step 1 will now be carried out according to Figure 3-1. Firstly, the wave parameters for point C are calculated using the 3D equations given in Subsection 3.2.4.3. Then their variation between C and D is determined with the 2D decay terms, as given in Subsection 3.2.4.2. This calculation proceeds in the following partial steps:

a) Dimensionless parameters and limitations check on the calculation of the wave generation and propagation

The dimensionless parameters relevant for wave generation are given in Table 5-10.

Table 5-10 Dimensionless parameters and limitations check for the calculation of wave generation and propagation.

Term	Dimensionless parameter	Range	Satisfied?
Slide Froude number	$F = 32/(9.81 \cdot 100)^{0.5} = 1.02$	$0.40 \leq F \leq 3.40$	Yes
Relative slide thickness	$S = 40/100 = 0.40$	$0.15 \leq S \leq 0.60$	Yes
Relative slide density	$D = 500/1,000 = 0.50$	$(0.59 \leq D \leq 1.72)$	No
Relative slide volume	$V = 600,000/(120 \cdot 100^2) = 0.50$	$0.187 \leq V \leq 0.750$	Yes
Relative Slide mass	$M = 500 \cdot 600,000/(1000 \cdot 120 \cdot 100^2) = 0.25$	$0.25 \leq M \leq 1.00$	Yes
Bulk slide porosity	$n = 45\%$	$(30.7 \leq n \leq 43.3)$	No
Relative slide width	$B = 120/100 = 1.20$	$0.83 \leq B \leq 5.00$	Yes
Slide impact angle	$\alpha = 35^\circ$	$30^\circ \leq \alpha \leq 90^\circ$	Yes
Impulse product parameter	$P = 1.02 \cdot 0.40^{0.5} \cdot 0.25^{0.25} \cdot \cos[6/7(35^\circ)]^{0.5} = 0.43$	$0.13 \leq P \leq 2.08$	Yes
Relative radial distance (A-B)	$r/h = 730/100 = 7.3$	$1 \leq r/h \leq 16$	Yes
Relative radial distance (A-C)	$r/h = 1,100/100 = 11$	$1 \leq r/h \leq 16$	Yes
Relative radial distance (A-D)	$r/h = (1,100 + 1,550)/100 = 26.5$	$1 \leq r/h \leq 16$	No
Wave propagation angle (A-B)	$\gamma = 0^\circ$	$-90^\circ \leq \gamma \leq 90^\circ$	Yes
Wave propagation angle (A-C)	$\gamma = 80^\circ$	$-90^\circ \leq \gamma \leq 90^\circ$	Yes

Therefore, all limitations for wave generation are satisfied, with the exception of the bulk slide porosity $n = 45\%$ and the relative slide density $D = 0.50$. The consequences of this will be discussed in Subsection 5.2.3, where Step 2 is described. To verify the wave propagation limitations on the relative distance r/h between points A and D, the distances A-C and C-D were added in Table 5-9. The distance A-D exceeds the limitation for 3D wave propagation. However, it is within the limitation for 2D (Table 3-2).

b) Calculation of wave generation and propagation

Of primary interest for this calculation are the wave amplitudes a_{c1} and a_{c2} . These wave characteristics will be determined at points B and C using the 3D method, as per Subsection 3.2.4.3. The impact radius $r_{0,0^\circ}$ and $r_{0,90^\circ}$ as well as the initial wave amplitudes $a_{0,c1}$, $a_{0,t1}$ and $a_{0,c2}$ are similar for both sections A-B and A-C and are determined as

$$r_{0,0^\circ} = 2.5 \left(P \left(\frac{b}{h} \right) \cos \alpha_{eff} \right)^{0.25} h \quad \text{Eq. (3.22)}$$

$$r_{0,0^\circ} = 2.5 \left(1.02 \left(\frac{120}{100} \right) \cos \left(\frac{6}{7} 35^\circ \right) \right)^{0.25} 100 = 204 \text{ m}$$

$$r_{0,90^\circ} = \left(\frac{b}{2} \right) + 1.5 \left(P \cos \alpha_{eff} \right)^{0.25} h \quad \text{Eq. (3.23)}$$

$$r_{0,90^\circ} = \left(\frac{120}{2} \right) + 1.5 \left(1.02 \cos \left(\frac{6}{7} 35^\circ \right) \right)^{0.25} 100 = 177 \text{ m}$$

$$a_{0,c1} = 0.2 P^{0.5} \left(\frac{b}{h} \right)^{0.75} \left(\cos \alpha_{eff} \right)^{0.25} h \quad \text{Eq. (3.26)}$$

$$a_{0,c1} = 0.2 \cdot 1.02^{0.5} \left(\frac{120}{100} \right)^{0.75} \left(\cos \left(\frac{6}{7} 35^\circ \right) \right)^{0.25} 100 = 14.4 \text{ m}$$

$$a_{0,t1} = 0.35 \left(P \left(\frac{b}{h} \right) \cos \alpha_{eff} \right)^{0.5} h \quad \text{Eq. (3.27)}$$

$$a_{0,t1} = 0.35 \left(1.02 \left(\frac{120}{100} \right) \cos \left(\frac{6}{7} 35^\circ \right) \right)^{0.5} 100 = 23.3 \text{ m}$$

$$a_{0,c2} = 0.14 \left(P \left(\frac{b}{h} \right) \cos \alpha_{eff} \right)^{0.25} h \quad \text{Eq. (3.28)}$$

$$a_{0,c2} = 0.14 \left(1.02 \left(\frac{120}{100} \right) \cos \left(\frac{6}{7} 35^\circ \right) \right)^{0.25} 100 = 11.4 \text{ m}$$

Section A-B

$$r_0(\gamma) = \sqrt{\frac{r_{0,0^\circ}^2 r_{0,90^\circ}^2}{r_{0,0^\circ}^2 \sin^2 \gamma + r_{0,90^\circ}^2 \cos^2 \gamma}} \quad \text{Eq. (3.24)}$$

$$r_0(0^\circ) = \sqrt{\frac{204^2 177^2}{204^2 \sin^2 0^\circ + 177^2 \cos^2 0^\circ}} = r_{0,0^\circ} = 204 \text{ m}$$

$$r^* = r - r_0 \quad \text{Eq. (3.25)}$$

$$r^* = 730 - 204 = 526 \text{ m}$$

$$a_{c1}(r^*, \gamma) = a_{0,c1} \exp \left[-0.4 \left(\frac{a_{0,c1}}{h} \right)^{-0.3} \sqrt{\frac{r^*}{h}} \right] \left[\operatorname{sech} \left(3.2 \frac{\gamma}{90^\circ} \right) \right]^{\cos \alpha_{eff} \exp \left(-0.15 \sqrt{\frac{r^*}{h}} \right)} \quad \text{Eq. (3.29)}$$

$$a_{c1} = 14.4 \exp \left[-0.4 \left(\frac{14.4}{100} \right)^{-0.3} \sqrt{\frac{526}{100}} \right] \left[\operatorname{sech} \left(3.2 \frac{0^\circ}{90^\circ} \right) \right]^{\cos \left(\frac{6}{7} 35^\circ \right) \exp \left(-0.15 \sqrt{\frac{526}{100}} \right)} = 2.8 \text{ m}$$

$$a_{t1}(r^*, \gamma) = a_{0,t1} \exp \left[-0.4 \left(\frac{a_{0,t1}}{h} \right)^{-0.3} \sqrt{\frac{r^*}{h}} \right] \left[\operatorname{sech} \left(3.6 \frac{\gamma}{90^\circ} \right) \right]^{\cos \alpha_{eff} \exp \left(-0.15 \sqrt{\frac{r^*}{h}} \right)} \quad \text{Eq. (3.30)}$$

$$a_{t1} = 23.3 \exp \left[-0.4 \left(\frac{23.3}{100} \right)^{-0.3} \sqrt{\frac{526}{100}} \right] \left[\operatorname{sech} \left(3.6 \frac{0^\circ}{90^\circ} \right) \right]^{\cos \left(\frac{6}{7} 35^\circ \right) \exp \left(-0.15 \sqrt{\frac{526}{100}} \right)} = 5.6 \text{ m}$$

$$a_{c2}(r^*, \gamma) = a_{0,c2} \exp \left[-0.1 \left(\frac{a_{0,c2}}{h} \right)^{-0.3} \sqrt{\frac{r^*}{h}} \right] \left[\operatorname{sech} \left(3 \frac{\gamma}{90^\circ} \right) \right]^{\cos \alpha_{eff} \exp \left(-0.15 \sqrt{\frac{r^*}{h}} \right)} \quad \text{Eq. (3.31)}$$

$$a_{c2} = 11.4 \exp \left[-0.1 \left(\frac{11.4}{100} \right)^{-0.3} \sqrt{\frac{526}{100}} \right] \left[\operatorname{sech} \left(3 \frac{0^\circ}{90^\circ} \right) \right]^{\cos \left(\frac{6}{7} 35^\circ \right) \exp \left(-0.15 \sqrt{\frac{526}{100}} \right)} = 7.4 \text{ m}$$

Section A-C

$$r_0(\gamma) = \sqrt{\frac{r_{0,0^\circ}^2 r_{0,90^\circ}^2}{r_{0,0^\circ}^2 \sin^2 \gamma + r_{0,90^\circ}^2 \cos^2 \gamma}} \quad \text{Eq. (3.24)}$$

$$r_0(80^\circ) = \sqrt{\frac{204^2 177^2}{204^2 \sin^2 (80^\circ) + 177^2 \cos^2 (80^\circ)}} = 178 \text{ m}$$

$$r^* = r - r_0 \quad \text{Eq. (3.25)}$$

$$r^* = 1100 - 178 = 922 \text{ m}$$

$$a_{c1}(r^*, \gamma) = a_{0,c1} \exp \left[-0.4 \left(\frac{a_{0,c1}}{h} \right)^{-0.3} \sqrt{\frac{r^*}{h}} \right] \left[\operatorname{sech} \left(3.2 \frac{\gamma}{90^\circ} \right) \right]^{\cos \alpha_{eff} \exp \left(-0.15 \sqrt{\frac{r^*}{h}} \right)} \quad \text{Eq. (3.29)}$$

$$a_{c1} = 14.4 \exp \left[-0.4 \left(\frac{14.4}{100} \right)^{-0.3} \sqrt{\frac{922}{100}} \right] \left[\operatorname{sech} \left(3.2 \frac{80^\circ}{90^\circ} \right) \right]^{\cos \left(\frac{6}{7} 35^\circ \right) \exp \left(-0.15 \sqrt{\frac{922}{100}} \right)} = 0.5 \text{ m}$$

$$a_{t1}(r^*, \gamma) = a_{0,t1} \exp \left[-0.4 \left(\frac{a_{0,t1}}{h} \right)^{-0.3} \sqrt{\frac{r^*}{h}} \right] \left[\operatorname{sech} \left(3.6 \frac{\gamma}{90^\circ} \right) \right]^{\cos \alpha_{eff} \exp \left(-0.15 \sqrt{\frac{r^*}{h}} \right)} \quad \text{Eq. (3.30)}$$

$$a_{t1} = 23.3 \exp \left[-0.4 \left(\frac{23.3}{100} \right)^{-0.3} \sqrt{\frac{922}{100}} \right] \left[\operatorname{sech} \left(3.6 \frac{80^\circ}{90^\circ} \right) \right]^{\cos \left(\frac{6}{7} 35^\circ \right) \exp \left(-0.15 \sqrt{\frac{922}{100}} \right)} = 0.9 \text{ m}$$

$$a_{c2}(r^*, \gamma) = a_{0,c2} \exp \left[-0.1 \left(\frac{a_{0,c2}}{h} \right)^{-0.3} \sqrt{\frac{r^*}{h}} \right] \left[\operatorname{sech} \left(3 \frac{\gamma}{90^\circ} \right) \right]^{\cos \alpha_{eff} \exp \left(-0.15 \sqrt{\frac{r^*}{h}} \right)} \quad \text{Eq. (3.31)}$$

$$a_{c2} = 11.4 \exp \left[-0.1 \left(\frac{11.4}{100} \right)^{-0.3} \sqrt{\frac{922}{100}} \right] \left[\operatorname{sech} \left(3 \frac{80^\circ}{90^\circ} \right) \right]^{\cos \left(\frac{6}{7} 35^\circ \right) \exp \left(-0.15 \sqrt{\frac{922}{100}} \right)} = 2.2 \text{ m}$$

As $a_{c2} > a_{c1}$, the decay of the wave amplitude $a_{c2} = 2.2$ m from point C to the embankment dam at point D will be determined using the 2D decay terms. According to Eq. (3.19), an impulse wave is attenuated in the wave channel (Figure 3-2a) in proportion to $(x/h)^{-4/15}$ (Figure 3-3a). The wave parameters at the dam are given by:

Section C-D

$$a_{c2}(x) \sim X^{-4/15} \quad \text{after Eq. (3.19)}$$

$$a_{c2} = 2.2(1,550/100)^{-4/15} = 1.1 \text{ m}$$

The wave crest amplitude $a_{c2} = 1.1$ m is therefore governing for the determination of the run-up height R on the slope of the embankment dam.

How long does it take for the first impulse wave to reach the opposite shore of the reservoir or the embankment dam? To determine the travel time of the first wave between the points A and B and between A and D (Figure 5-5), the first wave crest celerity c_{c1} has to be known, which is determined with

$$c_{c1}(r^*, \gamma) = 0.95 \sqrt{g(h + a_{c1})} \quad \text{Eq. (3.32)}$$

Equation (3.32) yields the instantaneous wave crest celerity at a specific location (r^*, γ) . To estimate the travel time, a mean celerity for the overall propagation distance is approximated. With $a_{0,c1} = 14.4$ m and $a_{c1}(730 \text{ m}, 0^\circ) = 2.8$ m, the mean first wave crest amplitude for section A-B is $a_{c1,m} = (14.4 + 2.8)/2 = 8.6$ m. With a still water depth $h = 100$ m (Figure 5-7a), the mean wave crest celerity is

$$c_{c1,m} = 0.95\sqrt{g(h + a_{c1,m})}$$

$$c_{c1,m} = 0.95\sqrt{9.81(100 + 8.6)} = 31 \text{ m/s}$$

The impulse wave covers the distance $r = 730$ m to the shore in roughly $r/c = 730/31 = 24$ s.

For section A-C with $\gamma = 80^\circ$, the wave amplitude a_{c1} at r_0 needs to be computed. For $r^* = 0$, the exponential terms in Eq. (3.29) equal 1 and the equation may be simplified to

$$a_{c1}(r^* = 0, \gamma) = a_{0,c1} \left[\operatorname{sech} \left(3.2 \frac{\gamma}{90^\circ} \right) \right]^{\cos \alpha_{\text{eff}}}$$

$$a_{c1}(0, 80^\circ) = 14.4 \left[\operatorname{sech} \left(3.2 \frac{80^\circ}{90^\circ} \right) \right]^{\cos \left(\frac{6}{7} 35^\circ \right)} = 2.2 \text{ m}$$

With a mean still water depth $h_m = (100 + 150)/2 = 125$ m (Figure 5-7a) and a mean wave amplitude $a_{c1,m} = (2.2 + 0.5)/2 = 1.4$ m between point A and D, the mean wave celerity is

$$c_{c1,m} = 0.95\sqrt{g(h_m + a_{c1,m})}$$

$$c_{c1,m} = 0.95\sqrt{9.81(125 + 1.4)} = 33.5 \text{ m/s}$$

The impulse wave takes about $r/c = (1,100 + 1,550)/33.5 = 79$ s to travel the 2650 m from the impact location (point A) to the dam (point D).

c) Wave run-up including limitations check

With help of the wave parameters calculated in b), the dimensionless parameters for the arch dam as well as the run-up height R (Eq. 3.36) may be calculated. For both sections, the second wave crest amplitudes a_{c2} are larger and are therefore considered for the estimation of R . As distinct from the case when waves run-up smooth and impermeable dams, the neglected governing parameters in Eq. (3.36), i.e. the permeability and roughness of the shore, may be relevant as they attenuate the run-up height R . The value obtained with Eq. (3.36) for point B at the shore thus tends to over-estimate the run-up height R observed in reality. In Tables 5-11 and 5-12 compliance with the limiting parameters is verified and then the run-up height R is computed. To check the non-linearity limitation, the wave height H is approximated with $H = a_{c2} + a_{t1}$.

Point B

The wave crest amplitude $a_{c2} = 1.1$ m is relevant for the determination of the run-up height R on the slope of the embankment dam at point D.

$$R = 2a \exp(0.4\varepsilon) \left(\frac{90^\circ}{\beta} \right)^{0.2} \quad \text{Eq. (3.36)}$$

$$R = 2 \cdot 7.4 \exp\left(0.4 \frac{7.4}{60}\right) \left(\frac{90^\circ}{35^\circ} \right)^{0.2} = 18.8 \text{ m}$$

Table 5-11 Dimensionless parameters and limitations check for the calculation of wave run-up at point B.

Term	Dimensionless parameter	Range	Satisfied?
Relative wave crest amplitude	$\varepsilon = a_{c2}/h = 7.4/60 = 0.12$	$0.007 \leq \varepsilon \leq 0.69$	Yes
Non-linearity	$a_{c2}/H = 7.4/(7.4+5.6) = 0.57$	$0.57 \leq a/H \leq 1.04$	Yes
Run-up angle	$\beta = 35^\circ$	$10^\circ \leq \beta \leq 90^\circ$	Yes
Slope parameter	$S_o = 1.521(\tan 35^\circ / 0.12^{0.5}) = 3.1$	$S_o \geq 0.37$	Yes

Point D

The wave crest amplitude $a_{c2} = 1.1$ m is governing for the determination of the run-up height R on the slope of the embankment dam at point D.

$$R = 2a \exp(0.4\varepsilon) \left(\frac{90^\circ}{\beta} \right)^{0.2} \quad \text{Eq. (3.36)}$$

$$R = 2 \cdot 1.1 \exp\left(0.4 \frac{1.1}{150}\right) \left(\frac{90^\circ}{45^\circ} \right)^{0.2} = 2.6 \text{ m}$$

To check the limitation of non-linearity a/H , the first wave trough amplitude a_{t1} at point D is determined:

$$a_{t1}(x) \sim X^{-4/15} \quad \text{after Eq. (3.19)}$$

$$a_{t1} = 0.9(1,550/100)^{-4/15} = 0.4 \text{ m}$$

Table 5-12 Dimensionless parameters and limitations check for the calculation of wave run-up at point D.

Term	Dimensionless parameter	Range	Satisfied?
Relative wave crest amplitude	$\varepsilon = a_c/h = 1.1/150 = 0.007$	$0.007 \leq \varepsilon \leq 0.69$	Yes
Non-linearity	$a_c/H = 1.1/(1.1+0.4) = 0.73$	$0.57 \leq a/H \leq 1.04$	Yes
Run-up angle	$\beta = 40^\circ$	$10^\circ \leq \beta \leq 90^\circ$	Yes
Slope parameter	$S_o = 1.521(\tan 45^\circ / 0.007^{0.5}) = 15$	$S_o \geq 0.37$	Yes

d) Wave overtopping

As the dam freeboard $f = 10$ m at point D is greater than the wave run-up height $R = 2.5$ m, the situation analysed in Step 1 does not result in overtopping. Evaluation of Step 2 has still to be considered (Subsection 5.2.3).

e) Force effect on the embankment dam

The total horizontal force component at point C with $\varepsilon = a/h = 0.11$ is

$$F_{tot,h} = [1 - 1.5(a/h)]^{1/6} F_{hs,h} \quad \text{Eq. (3.54)}$$

$$F_{tot,h} = [1 - 1.5(1.1/150)]^{1/6} (1/2) 1,000 \cdot 9.81 (2 \cdot 1.1 + 150)^2 = 113 \cdot 10^6 \text{ N/m.}$$

The elevation $z_{K,tot,h}$ of $F_{tot,h}$ is $(2a + h)/3 = (2 \cdot 1.1 + 150)/3 = 50.7$ m.

If $F_{tot,h}$ is reduced by the horizontal force component $F_{RW,h}$ resulting from hydrostatic pressure then the additional horizontal force component resulting only from the impulse wave is obtained as

$$\Delta F_h = F_{tot,h} - F_{RW,h} = F_{tot,h} - \rho_w g h^2 / 2 \quad \text{Eq. (3.54) - Eq. (3.52)}$$

$$\Delta F_h = 113 \cdot 10^6 - 1,000 \cdot 9.81 \cdot 150^2 / 2 = 3.1 \cdot 10^6 \text{ N/m.}$$

The additional horizontal force component ΔF_h resulting only from the impulse wave is relative to the hydrostatic effect $3.1 \cdot 10^6 / [1,000 \cdot 9.81 \cdot 150^2 / 2] = 3\%$. This additional impulse wave force component acts on the embankment dam for only a short time, typically for a few seconds.

The upstream dam face is inclined at an angle of $\beta = 40^\circ$. The forces computed thus far describe the horizontal force components when $\beta = 90^\circ$, but they do not change if $\beta < 90^\circ$. However, an additional total vertical force component $F_{tot,v}$ also acts on the inclined dam face (Subsection 3.5.2). This component can be determined for the effects of the impulse wave including hydrostatic pressure as

$$F_{tot,v} = F_{tot,h} / \tan \beta \quad \text{after Eq. (3.53)}$$

$$F_{tot,v} = 113 \cdot 10^6 / \tan 40^\circ = 135 \cdot 10^6 \text{ N/m.}$$

5.2.3 Step 2

The deviations determined in this subsection, which refer to the wave amplitude a , will be applied unchanged to the run-up height R . The following phenomena may lead to deviations as compared with Step 1 as shown in Figure 3-1:

- Exceeding of the limitations
- Volumetric displacement due to icefall
- Shoaling
- Reflection
- Constriction of the radial wave propagation and at the dam abutments

The following *limitations* are not satisfied: bulk slide porosity $n = 45\%$ ($30.7\% \leq n \leq 43.3\%$), bulk slide density $\rho_s = 500 \text{ kg/m}^3$ ($590 \text{ kg/m}^3 \leq \rho_s \leq 1,720 \text{ kg/m}^3$) and propagation distance A-D $r/h = 26.5$ ($1 \leq r/h \leq 16$). These will increase the uncertainty of the results.

The water level increase, as a result of the *volumetric displacement* by the icefall, for the reservoir surface area of $2.5 \cdot 10^6 \text{ m}^2$ (Figure 5-5) and for a bulk slide volume of $V_s = 600,000 \text{ m}^3$, is $600,000/2.5 \cdot 10^6 = 0.24 \text{ m}$. Considering a value of bulk slide porosity of $n = 45\%$ and the grain density $\rho_g = 900 \text{ kg/m}^3$ (i.e. $< 1,000 \text{ kg/m}^3$) the reservoir surface rise would be even less. For this reason, volumetric displacement may be neglected.

A further effect is *shoaling* (Section 4.2). The impulse waves approaching the dam will be partly influenced by the reservoir bed. The still water depth of $h = 100 \text{ m}$ used in Step 1 is constant up to the embankment dam, as shown by the dashed lines in Figure 5-7(b) and (c). As some of the wave energy is used to bring into motion the 50 m water column below the dashed line in Figure 5-7(c), the wave amplitude a at point D will be smaller than that calculated in Step 1. This effect may be calculated according to Green's law using Eq. (4.1). In doing this, values with the index 1 are denominated as idealised geometry with $h = 100 \text{ m} = \text{constant}$, whilst the index 2 denotes the condition with change from $h = 100 \text{ m}$ to $h = 150 \text{ m}$ (Figure 5-7). As the widths $b_1 = b_2$ are for both cases identical, the new wave crest amplitude a_2 at point D may be determined as

$$\frac{a_2}{a_1} = \left(\frac{h_1}{h_2} \right)^{1/4} \quad \text{for } b_1 = b_2 \quad \text{after Eq. (4.1)}$$

$$a_2 = a_1 \left(\frac{h_1}{h_2} \right)^{1/4} = 1.1 \left(\frac{100}{150} \right)^{1/4} = 1.0 \text{ m.}$$

This corresponds to a reduction from 1.1 m to 1.0 m, or about 10% compared with Step 1.

Next, possible *reflections* are discussed. If a wave encounters an obstruction the angle of incidence is equal to the angle of reflection (Figure 5-8). The reflection of the largest waves on the slide axis is not relevant for the dam, as they remain in the far end of the reservoir. The governing reflection is shown in Figure 5-8. From the calculation in Step 1 (Subsection 5.2.2) the wave movement from point C was assumed parallel to the shore line, in order to minimise the distance and remain on the safe side. In reality, the impulse waves follow a polygonal zig-zag course. The distance will thus be about 2,200 m, i.e. longer than the straight-line distance of $x = 1,550$ m between C and D (Table 5-9). In addition, at every reflection, the waves decrease in height (Section 4.2). From $a_{c2} = 2.2$ m at point C, the second wave crest amplitude decreases to less than 1.1 m at point D.

A final effect is *constriction*. The free, radial wave propagation on section A-C is to a large extent fulfilled. Only in the last portion is it somewhat restricted (Figure 5-5). At the dam abutments, the constriction may lead to an increase of the run-up height by about 20-30%, compared with the values calculated in Step 1 for the centre of the embankment dam (Subsection 4.2.2).

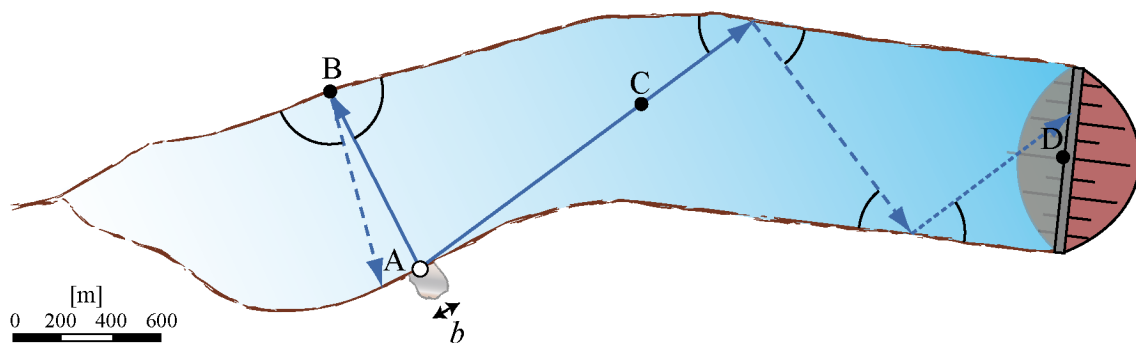


Figure 5-8 Wave reflection at point B has no consequences for the embankment dam. The wave propagating towards point C reaches the embankment dam. Angles of incidence and reflection at the run-up points are in each case the same.

In summary, the phenomena of shoaling leads to a slight decrease ($\approx -10\%$), the longer distance and the two reflections to a clear reduction of the wave height and the constriction to an increase ($\approx +20-30\%$) of the wave and run-up heights. These increases and decreases in Step 2 are more or less balanced. The freeboard of $f = 10$ m is sufficient to ensure that, with a run-up height $R = 2.6$ m, any overtopping is prevented.

5.2.4 Conclusions

In order to assess the effects of an impulse wave in a reservoir of the geometry shown in Figure 5-5, a computation in proximity of the impact zone, as far as point B on the opposite shore as well as to point C, is made by the 3D method. Between Points C and D the reservoir geometry resembles the geometry of a wave channel (Figure 5-5). Changes of the wave parameters between C and D were thus determined with the 2D

decay terms. According to Step 1, this method gives a run-up height of $R = 2.6$ m on the embankment dam. Use of Step 2, shown in Figure 3-1, may change this result slightly, as the deviations from the idealised conditions of Step 1 effect the run-up height R in both positive and negative senses. The available freeboard of $f = 10$ m is sufficient to prevent overtopping. The additional horizontal force component due to impulse wave acting on the dam is only about 3% of the force component resulting from hydrostatic pressure.

5.3 Example 3

The seven steps for estimating wave amplitudes and heights in intermediate water body geometries between 2D and 3D (Subsection 4.2.1) are illustrated with the 2014 Lake Askja case where a subaerial landslide generated impulse wave reached a runup height of 71 m. This case was numerically simulated by Gylfadóttir *et al.* (2017). The estimation of slide parameters is addressed in Chapter 3 such that the parameters from Ruffini *et al.* (2019) are taken over without derivation: $b = 550.0$ m, $s = 35.5$ m, $\alpha = 10.4^\circ$, $V_s = 30.1$ m/s, $m_s = 2 \times 10^{10}$ kg, $\rho_s = 2000$ kg/m³, $\rho_w = 1000$ kg/m³ and $h = 138.0$ m (step 1).

The wave type product $T = S^{1/3}M \cos(6/7\alpha)$ specifies the impulse wave type in 2D (Heller and Hager 2011). The given slide parameters $S = 0.26$, $M = 1.91$ and $F = 0.82$ result in $T = 1.21$, $4/5F^{-7/5} = 1.06$ and $11F^{-5/2} = 18.06$, corresponding to a cnoidal- or solitary-like wave because $1.06 \leq T = 1.21 \leq 18.06$ (Table 4-1). The former is selected as T is closer to the lower than the upper boundary such that $\beta = 1.03$ (step 2). The impulse product parameter P is

$$P = FS^{1/2}M^{1/4} \{\cos[(6/7)\alpha]\}^{1/2} \quad \text{Eq. (3.12)}$$

$$P = 0.82 \cdot 0.26^{1/2} \cdot 1.91^{1/4} \{\cos[(6/7)10.4]\}^{1/2} = 0.49.$$

Equations (3.13) and (3.14) result in (step 3)

$$H_M = (5/9)P^{4/5}h = (5/9)0.49^{4/5}138 = 43.3 \text{ m} \quad \text{Eq. (3.13)}$$

$$x_M = (11/2)P^{1/2}h = (11/2)0.49^{1/2}138 = 531 \text{ m.} \quad \text{Eq. (3.14)}$$

The maximum wave height $H_M = 43.3$ m predicted with the 2D approach is therefore observed at $x_M = 531$ m. The slide width at the coupling location is approximated with the slide width from the impact zone plus an arc section on either side of the slide (Figure 5-9). This approximation satisfies the energy flux conservation between $l_w(r' = 0, \theta)$ and $l_w(r', \theta)$, which coincides with the assumptions made for Green's law. Figure 5-9 illustrates the choice of the reservoir side angle $\theta_1 = 32.4^\circ$ and $\theta_2 = 44.1^\circ$ for the unsymmetrical Lake Askja. Note that r' in Eq. (4.2) is replaced with r in this step because the geometry already starts to diverge at $r = 0$ rather than at $r' = 0$. This results in

$$l_w(r, \theta) = b + 2r\theta_{rad} \quad \text{after Eq. (4.2)}$$

$$l_w(r = x_M, \theta) = 550 + 531(32.4/180 \cdot \pi + 44.1/180 \cdot \pi) = 1259 \text{ m}$$

at the coupling location (step 4).

save side (Subsection 4.2.1). This is in contrast to this example where the numerical value is 11% larger. However, it is unknown how well the numerical value represents the wave height in nature at the location of wave probe g9.

5.4 Example 4

The following example focuses on a comparison of phenomena that influence the triggering and acceleration of a landslide before it enters into the reservoir. Therefore, an idealised landslide reservoir geometry is chosen that allows estimating the impulse wave using the 2D procedure.

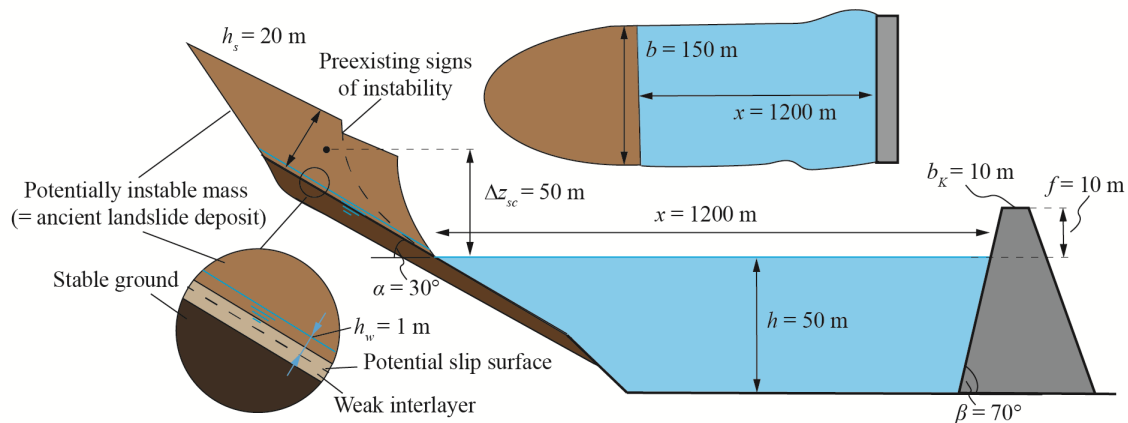


Figure 5-10 Geometry of the potential landslide and the reservoir.

In this example, the far end slope of a reservoir is assumed to be unstable (Figure 5-10). This slope is composed of a coarser soil mass deposited on a weaker interlayer. This kind of situation can be found e.g. where an ancient landslide has been deposited on top of a finer grained slope potentially trapping also the organic surface layer of the pre-existing slope. The weak interlayer consists of a clayey silt with organic and peaty fractions and has to be assumed to act as a preferential slip surface in case of an instability. The water table is slightly above the weak layer inside the landslide deposit. Therefore, the weak interlayer is fully saturated. The potentially instable mass shows signs of movement, such as sagging and tension cracks. Therefore, it may be assumed that the static factor of safety of that mass is close to unity.

Table 5-13 Geometry and geotechnical parameters of the potential instability and the reservoir.

Slope	Symbol	Unit	Value	Reservoir	Symbol	Unit	Value
Slide length	l_s	[m]	200	Width	b	[m]	150
Slide width	b	[m]	150	Distance to dam	x	[m]	1,200
Slide thickness (initial)	h_s	[m]	20	Still water depth (slide)	h	[m]	50
Volume	V	[m ³]	600,000	Still water depth (dam)	h	[m]	50
Inclination / slide impact angle	α	[°]	30	Run-up angle	β	[°]	70
Bulk slide density	ρ_s	[kg/m ³]	1,700	Freeboard	f	[m]	10
Bulk slide porosity	n	[%]	35	Dam crest width	b_K	[m]	10

The reservoir is situated in an area of substantial seismic risk; therefore, there is the danger of the slope failing during an earthquake. Table 5-13 summarises the parameters of the slope and reservoir. The slope is assumed to fail as a slab.

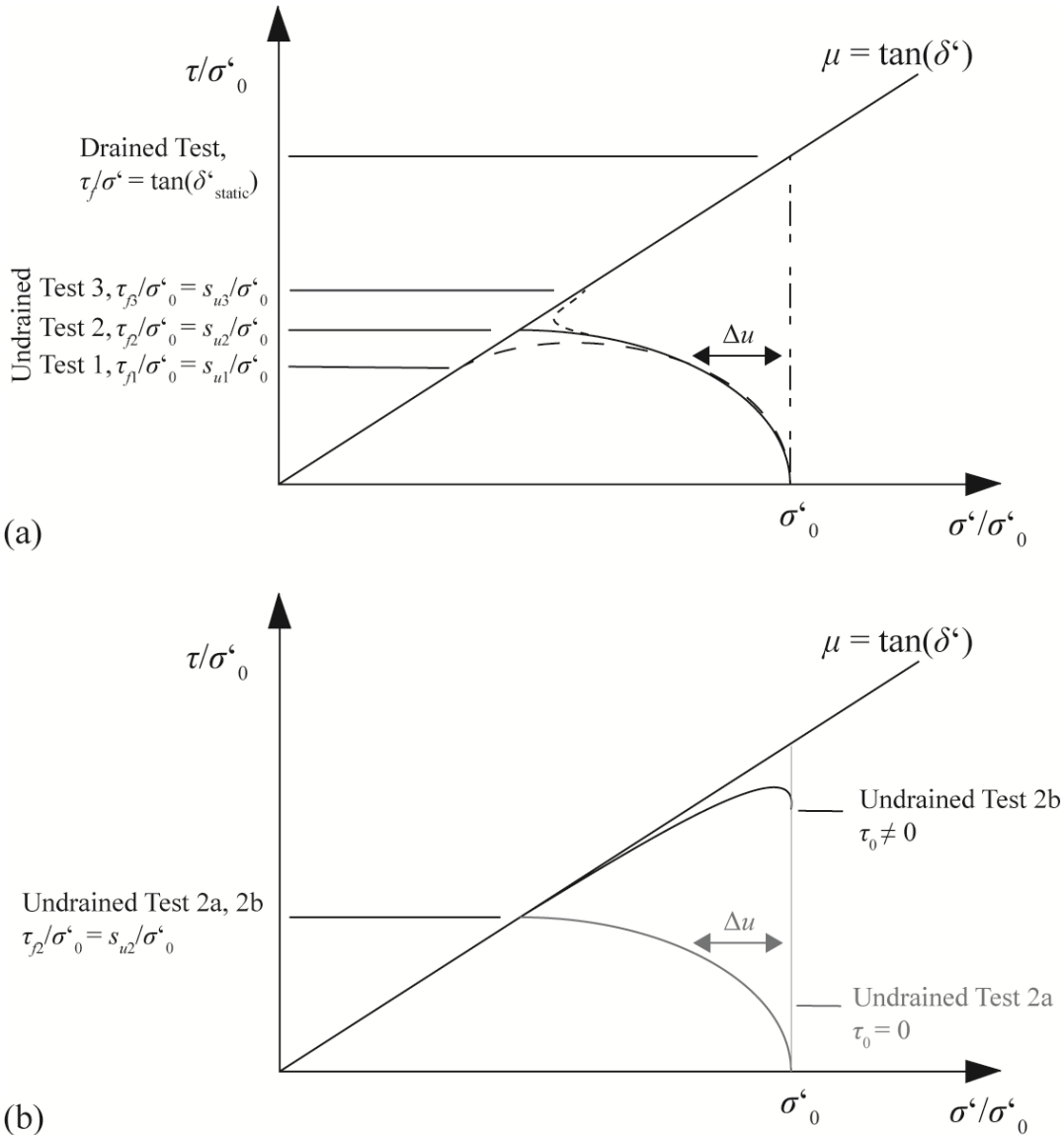


Figure 5-11 (a) Idealised results of drained and undrained stress paths on the presumed plane of failure in simple shear conditions and (b) comparison of idealised undrained stress paths on the presumed plane of failure for simple shear conditions with and without initial static shear stress.

Figure 5-11(a) shows example tests of idealised experimentally derived stress paths (drained and undrained) representative for silty and clayey materials as in the weak layer. Three different possible experimental results for undrained stress paths are shown:

- *Test 1*: Initially there is an increase of mobilised shear strength whilst the material shows contractive behaviour causing excess pore pressures to develop, therefore the stress path curves to the left. After reaching the undrained peak strength, the material softens and reaches failure (constant volume) at a lower shear resistance than the peak.

- *Test 2*: Similar to example Test 1 but the material mobilises shear resistance and develops excess pore pressure until it reaches the failure envelope and no more volume change takes place, i.e. the material deforms at constant stress.
- *Test 3*: The material mobilises shear strength and produces excess pore pressure until it reaches a second phase transformation point where the material behaviour becomes dilative causing the curvature of the stress path to reverse.

Note that the initial stress state for all three example tests of Figure 5-11(a) does not consider a static shear stress which is the case in sloping ground. However, these stress paths are considered to be typical results for many experimental investigations. Figure 5-11(b) shows a potential comparison between *Test 2* in Figure 5-11(a) and the same material taking into account sloping ground i.e. a static shear stress.

It has to be mentioned that these example tests are meant to show phenomenological examples of typical stress paths that can be observed in laboratory tests, but experiments may also produce different paths depending on the material properties. Particularly, the effect of static shear stress is not easy to evaluate and requires further research.

Table 5-14 shows the results of the calculation in terms of impact velocity and wave height. $\mu(\delta')$ is the static or dynamic drained friction in terms of friction ratio or friction angle (in brackets). s_u/σ'_0 and $\Delta u/\sigma'_0$ are the normalised ultimate undrained strength and excess pore pressure respectively as it could be derived from experiments for the three example tests assumed (Figure 5-11a).

Therefore, the excess pore pressure developing in the weak saturated layer is derived via the initial effective normal stress in the weak layer before onset of the seismic event $\sigma'_{0,field}$

$$\sigma'_{0,field} = (h_s \rho_s g - h_{w,0} \rho_w g) \cos \alpha$$

$$\frac{\Delta u_{test}}{\sigma'_{0,test}} = \frac{\Delta u_{field}}{\sigma'_{0,field}} \rightarrow \Delta u_{field}$$

The initial water table is observed about 1 m above the weak layer: $h_{w,0} \approx 1$ m. σ' is the effective normal stress acting on the presumed plane of sliding in the weak layer once excess pore pressure has built

$$\sigma' = \sigma'_{0,field} - \Delta u_{field} = (h_s \rho_s g - (h_{w,0} + h_{w,\Delta u}) \rho_w g) \cos \alpha \quad \text{with } h_{w,\Delta u} = \frac{\Delta u_{field}}{\rho_w g \cos \alpha}$$

τ_s and τ_r are the downslope acting shear stress and the shear resistance along a plane of sliding

$$\tau_s = h_s \rho_s g \sin \alpha$$

$$\tau_r = \sigma' \mu = \sigma' \tan \delta'.$$

FS is the resulting factor of safety of the slide

$$\text{FS} = \frac{\tau_r}{\tau_s}.$$

F_s and F_r are driving and resisting forces

$$F_s = m_s \sin \alpha = \tau_s l_s b$$

$$F_r = (m_s - m_w) g \cos \alpha \tan \delta' = \tau_r l_s b,$$

with $m_s = l_s h_s b \rho_s g$ and $m_w = l_s b (h_{w,0} + h_{w,\Delta u}) \rho_w$.

If the driving forces exceed the resisting ones, the unbalance in force produces the acceleration a_s and subsequently the impact velocity V_s

$$a_s = \frac{F_s - F_r}{m_s}$$

$$V_s = a_s \sqrt{\frac{2 \Delta z_{sc}}{a_s \sin \alpha}}$$

Following Subsection 3.2.4.2, the resulting maximum wave height H_M , maximum wave amplitude a_M , run up height R , and wave amplitude a for the 2D case can be derived (with slide thickness $s = h_s$). Table 5-14 contains the numeric results of the calculation. Note that low undrained strength can lead to significant acceleration also for milder slopes. For example, by assuming a slope with inclination of only 21° and material with undrained strength according to the experimental example tests above, the decrease in slope angle from 30° to 21° causes

- for the strength parameters of *Test 1* a drop in velocity from 25.1 m/s to 17.8 m/s ($\Delta V_s / V_{s,\alpha=30^\circ} = 29\%$),
- for the strength parameters of *Test 2* a drop in velocity from 23.7 m/s to 15.7 m/s ($\Delta V_s / V_{s,\alpha=30^\circ} = 34\%$) and
- for the strength parameters of *Test 3* a drop in velocity from 19.9 m/s to 8.02 m/s ($\Delta V_s / V_{s,\alpha=30^\circ} = 59\%$).

Table 5-14 Input parameters (rows 1-3) and calculation results for different strength assumptions.

		Drained strength (static friction)	Undrained strength (Test 1)	Undrained strength (Test 2)	Undrained strength (Test 3)
Experimental results (strength properties assumed)					
μ (δ°)	[-] ($[\circ]$)	0.675 (34°)	0.675 (34°)	0.675 (34°)	0.675 (34°)
s_u/σ_0'	[-]	-	0.22	0.26	0.36
$\Delta u/\sigma_0'$	[kPa]	-	0.67	0.61	0.47
Results of the analysis					
σ_0'	[kPa]	286	286	286	286
τ_s	[kPa]	170	170	170	170
τ_r	[kPa]	192	62	74	103
FS	[-]	1.19	0.37	0.44	0.61
F_s	[MN]	5.1	5.1	5.1	5.1
F_r	[MN]	5.8	2.5	3.0	4.1
a_s	[m/s ²]	-	3.15	2.81	1.97
V_s	[m/s]	-	25.1	23.7	19.9
H_M (Eq. 3.13)	[m]	-	24.9	23.8	20.7
a_M (Eq. 3.16)	[m]	-	19.9	19.1	16.6
a	[m]		11.5 ($>f=10$ m)	11.0 ($>f=10$ m)	9.6 ($<f=10$ m)
R	[m]	-	26.6	25.3	21.8

Undrained failure is usually triggered by a fast loading event such as an earthquake. A simple approach to investigate the effect of seismic loading in terms of earthquake-induced displacements is the Newark's sliding block approach (Newmark 1965). However, if the residual factor of safety of the sliding mass drops to a value below unity during cyclic loading, due to development of excess pore pressures, Newark's sliding block algorithm cannot readily be applied but the dynamic equilibrium needs to be solved.

Assuming the ultimate undrained strength from example Test 2 (Figure 5-11) and a slope-parallel input motion given in Figure 5-12(a), the velocity and displacement of the sliding mass depending on the development of excess pore pressure can be derived. Figure 5-12(b, c) show the velocity and displacement time history according to Newark's sliding block model. In addition, it shows the effect of different durations of pore pressure build-up expressed as reduction of the safety factor (red lines in Figure 5-12a):

- *Case 1*: immediate drop of resistance i.e. full development of excess pore pressure at onset of strong shaking;
- *Case 2*: linear drop of resistance, i.e. development of excess pore pressure over the duration of strong shaking;
- *Case 3*: partial drop of resistance, i.e. development of excess pore pressure over the duration of strong shaking, however sufficient loss of resistance to cause unbalancing of the slope.

Whilst for an immediate drop in safety factor (*Case 1*) the sliding body impacts into the lake during the seismic event (travel distance: $d = z_{sc}/\sin\alpha = 100$ m), slower genera-

tion of the excess pore pressure such as in Case 2 causes the landslide to stay in motion after the end of the earthquake. Even if the pore pressure generation is not finished before the end of the earthquake, it can be assumed that subsequent fast shearing will sustain the generation of excess pore pressure until the ultimate strength is reached (*Case 3*). Note that the impact velocity is not sensitive to the duration necessary to cause excess pore pressure to develop fully. Consequently, as long as sufficient pore pressure is generated to cause instability of the slope, subsequent fast shearing causes pore pressures to increase further and thus strength to drop to its residual level resulting in similar impact velocities.

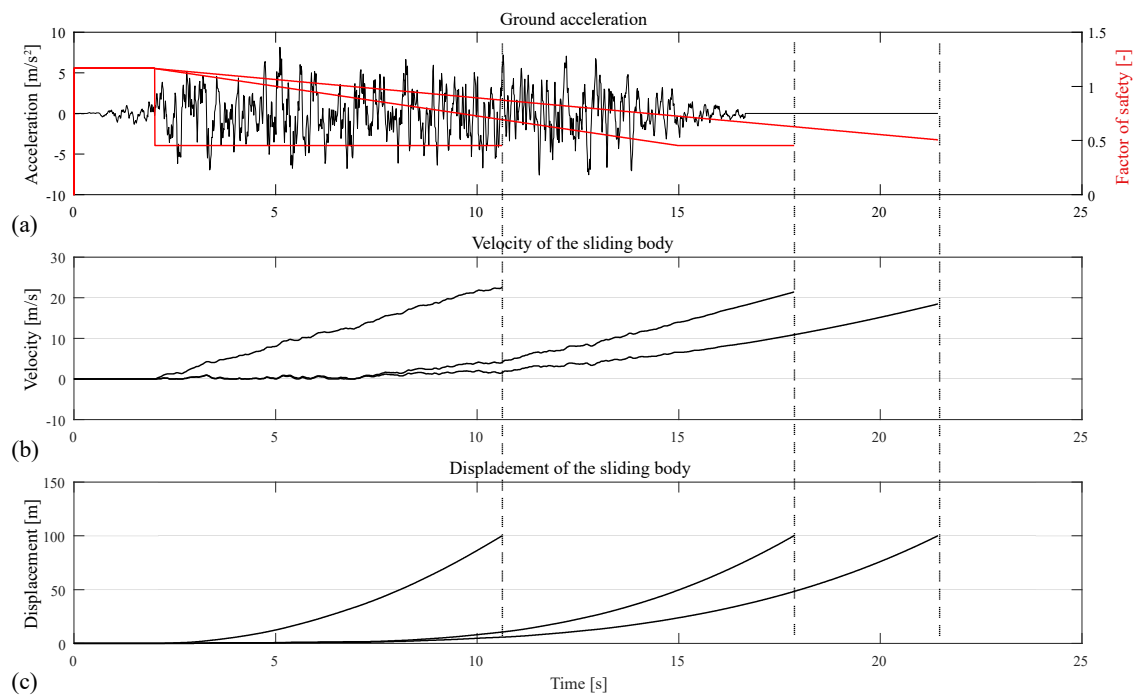


Figure 5-12 (a) Input motion and change in safety factor due to development of excess pore pressure, (b) development of slide velocity and (c) travelled distance of the slide.

5.5 Computational tool

5.5.1 Introduction

In this section the application of the computational tool, which can be downloaded in its latest version from <https://doi.org/10.5281/zenodo.3491999>, is explained. With this tool, the effects of impulse waves on both dams and shores can be evaluated. The spreadsheet facilitates Step 1 of the computational procedure (Chapter 3) but Step 2 must be carried out afterwards, *without* the computational tool, as described in Chapter 4.

The computational tool was created with the proprietary spreadsheet application Microsoft Excel 2016. Nevertheless, it is also executable with the open source spreadsheet application LibreOffice Calc (compatibility tested with version 6.1). The file includes *macros*, i.e. programs containing a pre-defined sequence of instructions, actions or key combinations. However, these macros have no effect on the computational procedure, since they are only applied to conveniently clear all input cells within a sheet at once. Therefore, the computational tool also runs without activated macros.

5.5.2 Structure

The spreadsheet file contains six sheets. A sheet can be selected by clicking on the sheet name in the lower, left-hand corner of the screen. The most important functions of the sheets are now explained. The names of the sheets are:

- a) START
- b) Generation | Propagation (2D)
- c) Generation | Propagation (3D)
- d) Run-up | Overtopping
- e) Overland flow
- f) Wave force

- a) START

This first sheet provides an overview of the subsequent computation sheets. The ‘Project’ text box on the upper left allows for inserting a project title, which is copied to the computation sheets. The definition sketch illustrates the two different wave generation and propagation processes available in the sheets ‘Generation | Propagation (2D)’ and ‘Generation | Propagation (3D)’. At the bottom, the colour coding is shown. Orange text boxes require the insertion of a text string, a parameter value, or the choice from a drop-down menu. Green and red shaded cells refer to the limitations, i.e. experimental parameter ranges, of the applied equations. The limitation cells are shaded green, when the respective parameter is within its limitations, while it is shaded red when there is no value or the limitation range is exceeded.

b) Generation | Propagation (2D)

The second sheet computes wave magnitudes based on governing slide parameters for the extreme case 2D. At the top the project title is copied from the ‘START’ sheet. The orange shaded text boxes allow for inserting the governing parameters for wave generation and propagation. The ‘Clear’ button deletes all parameter entries, if macros are enabled. The main results are provided at the lower left, while the limitations are given on the right.

c) Generation | Propagation (3D)

The third sheet computes wave magnitudes based on governing slide parameters for the extreme case 3D. At the top the project title is copied from the ‘START’ sheet. The orange shaded text boxes allow for inserting the governing parameters for wave generation and propagation. The ‘Clear’ button deletes all parameter entries, if macros are enabled. The main results are provided at the lower left, while the limitations are given on the right.

d) Run-up | Overtopping

The fourth sheet computes wave run-up and overtopping based on shore and dam parameters as well as wave parameters either for 2D or 3D. At the top the project title is copied from the ‘START’ sheet. The 2D or 3D wave parameters are copied from the sheets ‘Generation | Propagation (2D)’ or ‘Generation | Propagation (3D)’ completed before. The input source is selected via a dropdown menu on the right of the orange text box. For 3D wave input parameters, the higher wave crest amplitude is automatically selected. The additional orange shaded text boxes allow for inserting the governing parameters for wave run-up and overtopping. The ‘Clear’ button deletes all parameter entries, if macros are enabled. The main results are provided at the lower left, while the limitations are given on the right. Note, this sheet also includes the equations for overtopping at granular dams from Appendix A. However, these equations are not part of the main computational procedure of Step 1.

e) Overland flow

The fifth sheet computes overland flow characteristics based on shore parameters as well as wave parameters either for 2D or 3D. At the top the project title is copied from the ‘START’ sheet. The 2D or 3D wave parameters are copied from the sheets ‘Generation | Propagation (2D)’ or ‘Generation | Propagation (3D)’ completed before. The input source is selected via a dropdown menu on the right of the orange text box. For 3D wave input parameters, the higher wave crest amplitude is automatically selected. The additional orange shaded text boxes allow for inserting the governing parameters for overland flow. The ‘Clear’ button deletes all parameter

entries, if macros are enabled. The main results are provided at the lower left, while the limitations are given on the right.

f) Wave force

The sixth sheet computes the wave force on a dam structure based on dam parameters as well as wave parameters either for 2D or 3D. At the top the project title is copied from the ‘START’ sheet. The 2D or 3D wave parameters are copied from the sheets ‘Generation | Propagation (2D)’ or ‘Generation | Propagation (3D)’ completed before. The input source is selected via a dropdown menu on the right of the orange text box. For 3D wave input parameters, the higher wave crest amplitude is automatically selected. The additional orange shaded text boxes allow for inserting the governing parameters for the wave force. The ‘Clear’ button deletes all parameter entries, if macros are enabled. The main results are provided at the lower left, while the limitations are given on the right.

5.5.3 Application

The four sheets of the computational tool should be used in the order described below. The required sheet can be selected by clicking on to the corresponding sheet tab on the lower left of the window. Input cells for calculations are highlighted in orange. There is no access to any other cells. The computation takes place in the following four steps. The name of each corresponding sheet is thereby given in brackets.

- (i) Input of project name (‘START’).
- (ii) Decision whether 2D or 3D impulse wave generation and propagation processes have to be followed. Input of governing parameters for 2D (‘Generation | Propagation (2D)’) or 3D (‘Generation | Propagation (3D)’). All input text boxes have to be filled out to compute the wave characteristics at a specific location within the water body (coordinates: x for 2D, r and γ for 3D).
- (iii) Computation of the wave shore- or wave structure-interaction is conducted with the three following sheets for wave run-up and overtopping (‘Run-up | Overtopping’), overland flow on a horizontal hinterland (‘Overland flow’), and wave forces acting on a dam structure (‘Wave force’). For all processes, the wave input parameters are selected from the wave generation and propagation sheets via a drop-down menu, either 2D or 3D. Since wave overtopping only applies to dam structures, the freeboard f and the crest width b_K may be omitted, if only the run-up height R is of interest.
- (vi) Print: all sheets may be printed via the printing function of the spreadsheet application.

Afterwards, an assessment of the effects from Step 2, as shown in Figure 3-1, has to be carried out *without* the computational tool (Chapter 4).

5.5.4 Troubleshooting

Table 5-15 shows possible errors which may arise by using the computational tool with their possible cause and ways to correct them.

Table 5-15 Potential errors arising from the use of the computational tool with their causes and possibilities to correct them.

Error	Cause	Consequences/Correction
Nothing happens when 'Clear' button is clicked.	Macros are disabled.	Open spread sheet file and enable macros.
Cell displays ' $x < x_M$ '	The inserted 2D wave propagation distance x is smaller than the streamwise distance of the maximum wave amplitude from the impact location x_M .	Check if the value for the 2D wave propagation distance x is correctly inserted. Otherwise, x is too close to the impact location for obtaining a result and no computation is possible.
Cell displays ' $r < r_0$ '	The inserted 3D wave propagation distance r is smaller than the impact radius r_0 .	Check if the value for the 3D wave propagation distance r is correctly inserted. Otherwise, r is too close to the impact location for obtaining a result and no computation is possible.
Cell displays ' $\varepsilon < \varepsilon_{min}$ '	The relative wave crest amplitude ε of the approaching wave is smaller than the minimum relative wave crest amplitude ε_{min} to induce overland flow.	The approaching wave amplitude a is too small for obtaining a result.
Cell displays ' $2a < f$ '	The freeboard f is larger than twice the approaching wave amplitude a .	The approaching wave amplitude a is too small for obtaining a result.
Cell displays 'no value'	No input wave parameters may be retrieved.	Check the computation sheets for wave generation and propagation.
Cell displays '#VALUE!' or '#####'	An invalid parameter was inserted into a text box.	Check if all necessary input text boxes feature a numeric value. Errors may arise from alphabetic characters or not supported decimal separators.

6 Conclusions

In this manual the present state of practically oriented research on subaerial landslide-generated impulse waves (Figure 1-1) is described. The most important conclusions may be summarised as follows:

- Landslide-generated impulse waves occur typically in oceans, bays, lakes or reservoirs as a result of landslides, rock falls, shore instabilities, avalanches or glacier calvings. Various distinct theoretical wave types are considered when describing the impulse wave spectrum (Section 2.2).
- A *complete procedure* (Figure 3-1) has been developed for the assessment of the effects of landslide-generated impulse waves on dams; this takes into consideration parameters such as run-up height, overtopping volume and force effect, and is based on the use of generally applicable, semi-empirical equations.
- The analysis of the wave generation, as well as wave propagation, run-up and the overtopping of dams, considers all important governing parameters over a wide range. However, the procedure is limited to slide volumes that are significantly smaller than the volume of the reservoir or lake. For the cases described, the rise of the water surface level resulting from *volumetric displacement* by the slide is negligible compared with the wave height created by the slide impact.
- The *user* of the procedure can estimate, for example, the run-up height on the dam face, both at little cost and in a short time (Section 1.2).
- In *Step 1* of the procedure, generally applicable equations are used under idealised conditions, principally by considering granular slide material as well as a channel-shaped (Figure 3-2a) or a rectangular-shaped (Figure 3-2b) reservoir with a horizontal bed.
- In the *Step 2* of the procedure, the effects of deviations from the idealised conditions assumed in Step 1 are discussed. These relate above all to the reservoir shape and associated effects such as wave reflection, constriction or shoaling (Section 4.2), as well as the mass movement as a solid body rather than as a granular slide (Section 4.3).
- The procedure was successfully applied on hypothetical examples, as described in Chapter 5. A computational tool facilitates Step 1, but Step 2 must be carried out *without* this tool.

- The procedure is based on laboratory test results, many of which exhibit significant scatter and may only be used approximately for complex reservoir geometries. The results have, therefore, to be considered only as *estimates*. Safety allowances must be provided; these depend on the damage potential and the dam type, but cannot be generally formulated (Section 4.7). More precise results, also for cases where the geometry is complex, may be obtained from a prototype-specific model test and/or numerical simulations (Section 1.2).

References

- Abadie, S.M., Harris, J.C., Grilli, S.T., Fabre, R. (2012). Numerical modeling of tsunami waves generated by the flank collapse of the Cumbre Vieja Volcano (La Palma, Canary Islands): tsunami source and near field effects. *Journal of Geophysical Research: Oceans* 117(C5).
- Abadie, S., Morichon, D., Grilli, S., Glockner, S. (2010). Numerical simulation of waves generated by landslides using a multiple-fluid Navier-Stokes model. *Coastal Engineering* 57(9):779-794.
- Ataie-Ashtiani, B., Malek Mohammadi, S. (2007). Near field amplitude of subaerial landslide generated waves in dam reservoirs. *Dam Engineering* 17(4):197-222.
- Ataie-Ashtiani, B., Nik-Khah, A. (2008). Impulsive waves caused by subaerial landslides. *Environmental Fluid Mechanics* 8(3):263-280.
- Bascarini, C. (2010). Computational fluid dynamics modelling of landslide generated water waves. *Landslides* 7(2):117-124.
- Bolin, H., Yueping, Y., Xiaoting, C., Guangning, L., Sichang, W., Zhibing, J. (2014). Experimental modelling of tsunamis generated by subaerial landslides: two case studies of the Three Gorges Reservoir, China. *Environmental Earth Sciences* 71(9):3813-3825.
- Camfield, F.E. (1980). Tsunami Engineering. *Special Report SR-6*, U.S. Army Corps of Engineering, Coastal Engineering Research Center, Virginia.
- Carrier, W.D. (2003). Goodbye, Hazen; Hello, Kozeny-Carman. *Journal of Geotechnical and Geoenvironmental Engineering* 129(11):1054-1056.
- Chen, F., Heller, V., Briganti, R. (2019). Numerical modelling of tsunamis generated by iceberg calving validated with large-scale laboratory experiments. *Advances in Water Resources* (under review).
- Cruden, D.M., Varnes, D.J. (1996). Landslide types and processes. *Landslides*, Special Report 247:36-75. Turner, I., Schuster, A. eds. Transportation Research Board, Washington DC.
- Davies, T.R., McSaveney, M.J. (1999). Runout of dry granular avalanches. *Canadian Geotechnical Journal* 36:313-320.
- Dean, R.G., Dalrymple, R.A. (2004). Water wave mechanics for engineers and scientists. *Advanced Series on Ocean Engineering*, Vol. 2, World Scientific, Singapore.
- Di Risio, M. (2005). Landslide generated impulse waves: generation, propagation and interaction with plane slopes. *PhD Thesis*, Third University of Rome, Rome.
- Di Risio, M., Bellotti, G., Panizzo, A., De Girolamo, P. (2009a). Three-dimensional experiments on landslide generated waves at a sloping coast. *Coastal Engineering* 56(5-6):659-671.
- Di Risio, M., De Girolamo, P., Bellotti, G., Panizzo, A., Aristodemo, F., Molfetta, M.G., Petrillo, A.F. (2009b). Landslide-generated tsunamis runup at a coast of a conical island: new physical model experiments. *Journal of Geophysical Research: Oceans* 114(C01009).

- Di Risio, M., Sammarco, P. (2008). Analytical modeling of landslide-generated impulse waves. *Journal of Waterway, Port, Coastal, and Ocean Engineering* 134(1):53-60.
- Evers, F.M. (2017). Spatial propagation of landslide generated impulse waves. *Dissertation* 24650 and *VAW-Mitteilung* 244 (R. Boes, ed.), ETH Zurich, Zürich.
- Evers, F.M., Boes, R.M. (2019). Impulse wave runup on steep to vertical slopes. *Journal of Marine Science and Engineering* 7(1):8.
- Evers, F.M., Hager, W.H. (2015). Impulse wave generation: comparison of free granular with mesh-packed slides. *Journal of Marine Science and Engineering* 3(1):100-110.
- Evers, F.M., Hager, W.H., Boes, R.M. (2019). Spatial impulse wave generation and propagation. *Journal of Waterway, Port, Coastal, and Ocean Engineering* 145(3):04019011.
- Fritz, H.M. (2002). Initial phase of landslide generated impulse waves. *Dissertation* 14871 and *VAW-Mitteilung* 178 (H.-E. Minor, ed.), ETH Zurich, Zürich.
- Fuchs, H. (2013). Solitary impulse wave run-up and overland flow. *Dissertation* 21174 and *VAW-Mitteilung* 221 (R. Boes, ed.), ETH Zurich, Zürich.
- Fuchs, H., Boes, R. (2010). Berechnung felsrutschinduzierter Impulswellen im Vierwaldstättersee. *Wasser Energie Luft* 102(3):215-221 (in German).
- Fuchs, H., Hager, W.H. (2015). Solitary impulse wave transformation to overland flow. *Journal of Waterway, Port, Coastal, and Ocean Engineering* 141(5):04015004.
- Fuchs, H., Pfister, M., Boes, R., Perzmaier, S., Reindl, R. (2011). Impulswellen infolge Lawineneinstoss in den Speicher Kühtai. *Wasserwirtschaft* 101(1/2):54-60.
- Fuchs, H., Winz, E., Hager, W.H. (2013). Underwater landslide characteristics from 2D laboratory modeling. *Journal of Waterway, Port, Coastal, and Ocean Engineering* 139(6):480-488.
- Fuhrman, D.R., Madsen, P.A. (2009). Tsunami generation, propagation, and run-up with a high-order Boussinesq model. *Coastal Engineering* 56(7):747-758.
- Gabl, R., Seibl, J., Gems, B., Aufleger, M. (2015). 3-D-numerical approach to simulate the overtopping volume caused by an impulse wave comparable to avalanche impact in a reservoir. *Natural Hazards and Earth System Sciences* 15(12):2,617-2,630.
- Gedik, N., Irtem, E., Kabdasli, S. (2005). Laboratory investigation on tsunami run-up. *Ocean Engineering* 32(5-6):513-528.
- Grilli, S.T., Svendsen, I.A., Subramanya, R. (1997). Breaking criterion and characteristics for solitary waves on slopes. *Journal of Waterway, Port, Coastal, and Ocean Engineering* 123(3):102-112.
- Gylfadóttir, S.S., Kim, J., Helgason, J.K., Brynjólfsson, S., Höskuldsson, A., Jóhannesson, T., Harbitz, C.B., Løvholt, F. (2017). The 2014 Lake Askja rockslide induced tsunami: optimization of numerical tsunami model using observed data. *Journal of Geophysical Research: Oceans* 122(5):4110-4122.

- Hampton, M.A., Lee, H.J., Locat, J. (1996). Submarine landslides. *Reviews of Geophysics* 34(1):33-59.
- Harbitz, C.B., Glimsdal, S., Løvholt, F., Kveldevisk, V., Pedersen, G.K., Jensen, A. (2014). Rockslide tsunamis in complex fjords: from an unstable rock slope at Åkerneset to tsunami risk in western Norway. *Coastal Engineering* 88(6):101-122.
- Heller, V. (2007). Landslide generated impulse waves: prediction of near field characteristics. *Dissertation 17531 and VAW-Mitteilung 204* (H.-E. Minor, ed.), ETH Zurich, Zürich.
- Heller, V., Bruggemann, M., Spinneken, J., Rogers, B. (2016). Composite modelling of subaerial landslide-tsunamis in different water body geometries and novel insight into slide and wave kinematics, *Coastal Engineering* 109(3):20-41.
- Heller, V., Chen, F., Brühl, M., Gabl, R., Chen, X., Wolters, G., Fuchs, H. (2019). Large-scale experiments into the tsunamigenic potential of different ice calving mechanisms. *Scientific Reports* 9:861.
- Heller, V., Hager, W.H., Minor, H.-E. (2009). Landslide generated impulse waves in reservoirs: basics and computation. *VAW-Mitteilung 211* (R. Boes, ed.), ETH Zurich, Zürich.
- Heller, V., Hager, W.H. (2010). Impulse product parameter in landslide generated impulse waves. *Journal of Waterway, Port, Coastal, and Ocean Engineering* 136(3):145-155.
- Heller, V., Hager, W.H. (2011). Wave types of landslide generated impulse waves. *Ocean Engineering* 38(4):630-640.
- Heller, V., Hager, W.H., Minor, H.-E. (2008). Scale effects in subaerial landslide generated impulse waves. *Experiments in Fluids* 44(5):691-703.
- Heller, V., Kinnear, R.D. (2010). Discussion of “Experimental investigation of impact generated tsunami; related to a potential rock slide, Western Norway” by G. Sælevik, A. Jensen, G. Pedersen, *Coastal Engineering* 57(8):773-777.
- Heller, V., Moalemi, M., Kinnear R.D., Adams, R.A. (2012). Geometrical effects on landslide-generated tsunamis. *Journal of Waterway, Port, Coastal and Ocean Engineering* 138(4):286-298.
- Heller, V., Spinneken, J. (2013). Improved landslide-tsunami prediction: effects of block model parameters and slide model. *Journal of Geophysical Research: Oceans* 118(3):1489-1507.
- Heller, V., Spinneken, J. (2015). On the effect of the water body geometry on landslide-tsunamis: physical insight from laboratory tests and 2D to 3D wave parameter transformation. *Coastal Engineering* 104(10):113-134.
- Huber, A. (1982). Felsbewegungen und Uferabbrüche an Schweizer Seen, ihre Ursachen und Auswirkungen. *Eclogae geologicae Helvetiae* 75(3):563-578.
- Huber, A., Hager, W.H. (1997). Forecasting impulse waves in reservoirs. Proc. 19th *Congrès des Grands Barrages*, Florence C.31:993-1,005. ICOLD, Paris.
- Huber, L.E., Evers, F.M., Hager, W.H. (2017). Solitary wave overtopping at granular dams. *Journal of Hydraulic Research* 55(6):799-812.

- Hughes, S.A. (1993). Physical models and laboratory techniques in coastal engineering. *Advanced Series on Ocean Engineering* 7. World Scientific, London.
- Hughes, I., Hase, T. (2010). Measurements and their uncertainties: a practical guide to modern error analysis. Oxford University Press, Oxford.
- Hungr, O., Corominas, J., Eberhardt, E. (2005). Estimating landslide motion mechanism, travel distance and velocity. In *Landslide Risk Management* (R. Fell, O. Hungr, R. Couture, E. Eberhardt, eds.) (pp. 104-133). CRC Press, London.
- Hunt, A. (1959). Design of seawalls and breakwaters. *Journal of the Waterways and Harbor Division ASCE* 85(WW3):123-152.
- ICOLD (2002). *Reservoir landslides: investigation and management - Guidelines and case histories*. Bulletin 124, ICOLD, Paris.
- Kessler, M., Heller, V., Turnbull, B. (2018). A laboratory-numerical approach for modelling scale effects in dry granular slides. *Landslides* 15(11):2145-2159.
- Kobel, J., Evers, F.M., Hager, W.H. (2017). Impulse wave overtopping at rigid dam structures. *Journal of Hydraulic Engineering* 143(6):04017002.
- Körner, H.J. (1976). Reichweite und Geschwindigkeit von Bergstürzen und Fliessschneelawinen. *Rock Mechanics* 8(4):225-256.
- Lindström, E.K. (2016). Waves generated by subaerial slides with various porosities. *Coastal Engineering* 116(10):170-179.
- Liu, P.L.-F., Wu, T.-R., Raichlen, F., Synolakis, C.E., Borrero, J.C. (2005). Runup and rundown generated by three-dimensional sliding masses. *Journal of Fluid Mechanics* 536:107-144.
- Lüthi, M.P., Vieli, A. (2016). Multi-method observation and analysis of a tsunami caused by glacier calving. *The Cryosphere* 10(3):995-1002.
- Lynett, P., Liu, L.-F. (2005). A numerical study of the run-up generated by three-dimensional landslides. *Journal of Geophysical Research: Oceans* 110(C03006).
- Ma, G., Shi, F., Kirby, J.T. (2012). Shock-capturing non-hydrostatic model for fully dispersive surface wave processes. *Ocean Modelling* 43:22-35.
- MacFarlane, D.F., Jenks, D.G. (1996). Stabilisation and performance of No. 5 Creek Slide, Clyde Power Project, New Zealand. Proc. 7th Intl. Symp. *Landslides Trondheim* 3:1,739-1,746. Senneset, K. ed. Balkema, Rotterdam.
- Madsen, P.A., Fuhrman, D.R., Schäffer, H.A. (2008). On the solitary wave paradigm for tsunamis. *Journal of Geophysical Research: Oceans* 113(C12012).
- Marzeddu, A., Oliveira, T.C., Gironella, F.X., Sánchez-Arcilla, A. (2017). Variability of wave impact measurements on vertical breakwaters. *Journal of Hydraulic Research* 55(6):772-786.
- McFall, B.C., Fritz, H.M. (2017). Runup of granular landslide-generated tsunamis on planar coasts and conical islands. *Journal of Geophysical Research: Oceans* 122:6901-6922.

- Müller, D. (1995). Auflaufen und Überschwappen von Impulswellen an Talsperren. *VAW-Mitteilung* 137 (Vischer, D., ed.), ETH Zurich, Zürich.
- Müller, D., Schurter, M. (1993). Impulse waves generated by an artificially induced rockfall in a swiss lake. Proc. 25th IAHR Congress Tokyo. IAHR, Madrid.
- Newmark, N.M. (1965). Effects of earthquakes on dams and embankments. *Geotechnique* 15(2):139-160.
- Noda, E. (1970). Water waves generated by landslides. *Journal of Waterways, Harbors and Coastal Engineering Division ASCE* 96(WW4):835-855.
- Oppikofer, T., Hermanns, R.L., Sandoy, G., Böhme, M., Jaboyedoff, M., Horton, P., Roberts, N.J., Fuchs, H. (2016). Quantification of casualties from potential rock-slope failures in Norway. *Landslides and Engineered Slopes - Experience, Theory and Practice*, 1537-1544, Aversa et al., eds.
- Panizzo, A., De Girolamo, P., Petaccia, A. (2005). Forecasting impulse waves generated by subaerial landslides. *Journal of Geophysical Research* 110 C12025:1-23.
- Pudasaini, S.P., Miller, S.A. (2013). The hypermobility of huge landslides and avalanches. *Engineering Geology* 157(5):124-132.
- Ramsden, J.D. (1996). Forces on a vertical wall due to long waves, bores, and dry-bed surges. *Journal of Waterway, Port, Coastal, and Ocean Engineering* 122(3):134-141.
- Roberts, N.J., McKillop, R.J., Lawrence, M.S., Psutka, J.F., Clague, J.J., Brideau, M.A., Ward, B.C. (2013). Impacts of the 2007 landslide-generated tsunami in Chehalis Lake, Canada. In *Landslide science and practice* (pp. 133-140). Springer, Berlin, Heidelberg.
- Ruffini, G., Heller, V., Briganti, R. (2019). Numerical modelling of landslide-tsunami propagation in a wide range of idealised water body geometries. *Coastal Engineering* 153:103518.
- Salm, B., Burkard, A., Gubler, H.U. (1990). Berechnung von Fliesslawinen - Eine Anleitung für Praktiker mit Beispielen. *Mitteilung des Eidgenössischen Instituts für Schnee und Lawinenforschung* 47, SLF, Davos.
- Schnitter, G. (1964). Die Katastrophe von Vaiont in Oberitalien. *Wasser- und Energiewirtschaft* 56(2/3):61-69.
- Schröder, W., Saenger, N. (2002). Wasserbau und Wasserwirtschaft. *Bautabellen für Ingenieure mit Berechnungshinweisen und Beispielen* 13.0-13.146. Schneider, K.-J., ed. Werner, Düsseldorf.
- Schuster, R.L., Wieczorek, G.F. (2002). Landslide triggers and types. Proc. 1st European Conf. *Landslides*, Prague, 59-78. Rybář, J., Stemberk, J., Wagner, P. eds. Balkema, Tokyo.
- Singh, V.P. (1996). *Dam breach modeling technology*. Kluwer Academic Publisher, London.
- Tan, H., Chen, S. (2017). A hybrid DEM-SPH model for deformable landslide and its generated surge waves. *Advances in Water Resources* 108(10):256-276.

- Tan, H., Ruffini, G., Chen, S., Heller, V. (2018). A numerical landslide-tsunami hazard assessment technique applied on hypothetical scenarios at Es Vedrà, offshore Ibiza. *Journal of Marine Science and Engineering* 6(4):1-22.
- Tang, G., Lu, L., Teng, Y., Zhang, Z., Xie, Z. (2018). Impulse waves generated by subaerial landslides of combined block mass and granular material. *Coastal Engineering* 141(11):68-85.
- Teng, M.H., Feng, K., Liao, T.I. (2000). Experimental study on long wave run-up on plane beaches. Proc. 10th Intl. Offshore and Polar Engineering Conference (3):660-664. Seattle, USA.
- Ursell, F. (1952). Edge waves on a sloping beach. *Proceeding of the Royal Society A* 214:79-97.
- USACE - U.S. Army Corps of Engineers (2002). Coastal Engineering Manual, Engineer Manual 1110-2-1100, U.S. Army Corps of Engineers, Washington, D.C. (in 6 volumes).
- Vacondio, R., Mignosa, P., Pagani, S. (2013). 3D SPH numerical simulation of the wave generated by the Vajont rockslide. *Advances in Water Resources* 59(9):146-156.
- Viroulet, S., Cébron, D., Kimmoun, O., Kharif, C. (2013). Shallow water waves generated by subaerial solid landslides. *Geophysical Journal International* 193(2):747-762.
- Walkden, M.J.A. (1999). Model wave impulse loads on caisson breakwaters: aeration, scale and structural response. *PhD Thesis*, University of Plymouth, UK.
- WCHL (1970). Hydraulic model studies - wave action generated by slides into Mica Reservoir - British Columbia. *Report*. Western Canada Hydraulic Laboratories, Vancouver.
- Yavari-Ramshe, S., Ataie-Ashtiani, B. (2016). Numerical modelling of subaerial and submarine landslide-generated tsunami waves-recent advances and future challenges. *Landslides* 13(6):1,325-1,368.
- Zweifel, A. (2004). Impulswellen: Effekte der Rutschdicke und der Wassertiefe. *Dissertation* 15596 and *VAW-Mitteilung* 186 (H.-E. Minor, ed.), ETH Zurich, Zürich.
- Zweifel, A., Zuccalà, D., Gatti, D. (2007). Comparison between computed and experimentally generated impulse waves. *Journal of Hydraulic Engineering* 133(2):208-216.

Notation

Roman symbols

a	[m]	=	wave amplitude
a_{c1}	[m]	=	first wave crest amplitude (3D)
a_{c2}	[m]	=	second wave crest amplitude (3D)
a_{eq}	[m/s ²]	=	earthquake induced acceleration
a_M	[m]	=	maximum wave amplitude
a_{Mb}	[m]	=	maximum wave amplitude as result of a solid body
a_R	[m]	=	wave amplitude of a reflected wave
a_s	[m/s ²]	=	slide acceleration
$a_{s,NK}$	[m/s ²]	=	acceleration of the slide along the slope before the point of slope change
a_{t1}	[m]	=	first wave trough amplitude (3D)
a_w	[m]	=	effective wave crest amplitude
$a_{0,c1}$	[m]	=	initial first wave crest amplitude (3D)
$a_{0,c2}$	[m]	=	initial second wave crest amplitude (3D)
$a_{0,t1}$	[m]	=	initial first wave trough amplitude (3D)
a_1	[m]	=	wave amplitude at cross-section 1 of Figure 4-2(b)
a_2	[m]	=	wave amplitude at cross-section 2 of Figure 4-2(b)
A	[-]	=	relative wave amplitude; $A = a/h$
A_M	[-]	=	relative maximum wave amplitude; $A_M = a_M/h$
A_s	[m ²]	=	area of the slip surface i.e. contact area between slide and stable ground
b	[m]	=	slide or reservoir width in the prototype; channel width in the model
b_K	[m]	=	crest width
b_1	[m]	=	reservoir width at cross-section 1 of Figure 4-2(b)
b_2	[m]	=	reservoir width at cross-section 2 of Figure 4-2(b)
B	[-]	=	relative slide width; $B = b/h$
c	[m/s]	=	wave celerity
c_{c1}	[m/s]	=	first wave crest celerity
c_{c1}	[m/s]	=	second wave crest celerity
d	[-]	=	differential
d_b	[m]	=	block diameter
d_g	[m], [mm]	=	grain diameter

Notation

d_0	[m]	=	maximum (overtopping) flow depth
D	[-]	=	relative slide density; $D = \rho_s / \rho_w$
e	[-]	=	logarithmic constant; $e \approx 2.72$
f	[m]	=	freeboard
F	[-]	=	slide Froude number; $F = V_s / (gh)^{1/2}$
$F_{hs,h}$	[N/m]	=	horizontal component of hydrostatic force per unit length dam crest resulting from a still water level displaced upwards by $2a$, according to Ramsden (1996)
F_r	[MN]	=	driving forces
F_s	[MN]	=	resisting forces
$F_{tot,h}$	[N/m]	=	total horizontal force component per unit length dam crest resulting from an impulse wave and hydrostatic pressure
$F_{tot,v}$	[N/m]	=	total vertical force component per unit length dam crest resulting from an impulse wave and hydrostatic pressure
$F_{tot,h,red}$	[N/m]	=	reduced total horizontal force component per unit length dam crest resulting from an impulse wave and hydrostatic pressure
$F_{tot,v,red}$	[N/m]	=	reduced total vertical force component per unit length dam crest resulting from an impulse wave and hydrostatic pressure
$F_{RW,h}$	[N/m]	=	horizontal force component per unit length dam crest resulting only from hydrostatic pressure
$F_{RW,v}$	[N/m]	=	vertical force component per unit length dam crest resulting only from hydrostatic pressure
g	[m/s ²]	=	gravitational acceleration; $g = 9.81 \text{ m/s}^2$
G_s	[N]	=	total weight of the slide
G'_s	[N]	=	effective slide weight as function of pore pressure u
h	[m]	=	still water depth
h_s	[m]	=	initial thickness of the slide mass
h_w	[m]	=	initial water table thickness
h_1	[m]	=	still water depth at cross-section 1 of Figure 4-2(b)
h_2	[m]	=	still water depth at cross-section 2 of Figure 4-2(b)
H	[m]	=	wave height
H_M	[m]	=	maximum wave height
H_1	[m]	=	wave height at cross-section 1 of Figure 4-2(b)
H_2	[m]	=	wave height at cross-section 2 of Figure 4-2(b)
k	[m/s]	=	permeability
l	[m]	=	coordinate along dam crest

l_s	[m]	=	slide length
l_F	[m]	=	width of reservoir flank
l_K	[m]	=	crest length
l_s	[m]	=	slide length
l_w	[m]	=	wave front length
L	[m]	=	wave length
L_M	[m]	=	wave length of H_M
L_1	[m]	=	first wave length (3D)
L_1	[m]	=	wave length at cross-section 1 of Figure 4-2(b)
L_2	[m]	=	wave length at cross-section 2 of Figure 4-2(b)
m_g	[kg]	=	slide grain mass identical to slide mass; $m_g = m_s$
m_s	[kg]	=	slide mass identical to slide grain mass; $m_s = m_g$
M	[-]	=	relative slide mass; $M = D \cdot V = m_s / (\rho_w b h^2) = \rho_s V_s / (\rho_w b h^2)$
M_s	[-]	=	impact angle-corrected relative slide mass
n	[%]	=	bulk slide porosity
p	[N/m ²]	=	pressure on dam
p_K	[N/m ²]	=	pressure at dam crest
P	[-]	=	impulse product parameter; $P = FS^{1/2} M^{1/4} \{\cos[(6/7)\alpha]\}^{1/2}$
q_0	[m ² /s]	=	maximum specific overland flow discharge
q_m	[m ² /s]	=	average discharge per unit dam crest length
r	[m]	=	radial distance from the impact location in the wave basin
r'	[m]	=	radial distance from the coupling location
r^*	[m]	=	surrogate radial distance from the impact location
r_0	[m]	=	impact radius
$r_{0,0^\circ}$	[m]	=	impact radius for $\gamma = 0^\circ$
$r_{0,90^\circ}$	[m]	=	impact radius for $\gamma = 90^\circ$
R	[m]	=	run-up height
R_{eM}	[m]	=	maximum edge wave run-up height
R_m	[m]	=	run-up height at the dam centre
s	[m]	=	slide thickness
s_{end}	[m]	=	maximum thickness of slide deposits
s_u	[kPa]	=	undrained shear strength of the slip surface
S	[-]	=	relative slide thickness; $S = s/h$
S_o	[-]	=	slope parameter by Grilli <i>et al.</i> (1997)
t	[s]	=	time from slide impact; time
t'	[s]	=	time from when the wave reaches the coupling location
t_s	[s]	=	time of underwater slide motion

Notation

t_o	[s]	=	wave overtopping duration
T	[s]	=	wave period
T_M	[s]	=	wave period of H_M
T_1	[s]	=	first wave period (3D)
u	[kPa]	=	pore water pressure
$v_{f,max}$	[m/s]	=	maximum flow front velocity at $x_{ov}/w = 5$
$\tilde{v}_{x,max}$	[m/s]	=	maximum depth-averaged horizontal flow velocity at x_{tr}
V	[-]	=	relative slide volume; $V = \mathcal{V}_s/(bh^2)$
V_s	[m/s]	=	slide impact velocity
V_{sNK}	[m/s]	=	slide velocity at point of slope change (Figure 3-4b)
\mathcal{V}	[m ³ /m]	=	overtopping volume per unit length dam crest
\mathcal{V}_g	[m ³]	=	slide grain volume
\mathcal{V}_s	[m ³]	=	bulk slide volume
\mathcal{V}_0	[m ³ /m]	=	overtopping volume per unit length dam crest for $f = 0$
w	[m]	=	dam/shore height
x	[m]	=	streamwise coordinate in longitudinal channel direction and distance in 2D
x'_{end}	[m]	=	front position of slide deposits
x_f^*	[-]	=	relative flow front position
x_f	[m]	=	overland flow front position measured from the transition point x_{tr}
x_M	[m]	=	streamwise distance of the maximum wave amplitude from the impact location
x_{ov}	[m]	=	streamwise overland flow coordinate measured from the transition point x_{tr}
X	[-]	=	relative streamwise distance; $X = x/h$
X_M	[-]	=	relative streamwise distance of a_M (or H_M) from the impact location; $X_M = x_M/h$
y	[-]	=	rational number in the hyperbolic function
z	[m]	=	vertical coordinate
$Z_{K,tot,h}$	[m]	=	elevation of the resultant of $F_{tot,h}$
$Z_{K,tot,h,red}$	[m]	=	elevation of the resultant of $F_{tot,h,red}$
$Z_{\Delta K,h}$	[m]	=	elevation of the resultant of ΔF_h

Greek symbols

α	[°]	=	slide impact angle equal to hill slope angle
α_{eff}	[°]	=	effective slide impact angle; $\alpha_{eff} = (6/7)\alpha$
α_N	[°]	=	hill slope angle for a hill slope section (Figure 3.5)
β	[°]	=	run-up angle equal to dam face slope; pre-factor of Eqs. (4.3) and (4.4)
γ	[°]	=	wave propagation angle from the impact location
γ'	[°]	=	wave propagation angle from the coupling location
ε	[-]	=	relative wave crest amplitude; $\varepsilon = a/h$
ε_{eff}	[-]	=	effective relative wave amplitude
ε_{min}	[-]	=	minimum relative wave amplitude to induce overland flow
δ	[°]	=	dynamic bed friction angle
δ_N	[°]	=	dynamic bed friction angle for a hill slope section
Δ_{sc}	[m]	=	travel distance of the centre of gravity before entering the lake
ΔF_h	[N/m]	=	additional horizontal force component per unit length dam crest resulting from impulse wave
ΔF_v	[N/m]	=	additional vertical force component per unit length dam crest resulting from impulse wave
Δu	[-]	=	excess pore pressure
$\Delta x'$	[-]	=	scatter of x'
Δz_{sc}	[m]	=	drop height of the centre of gravity of the slide
Δz_{scN}	[m]	=	drop height of the centre of gravity of the slide between any two slide positions
η	[m]	=	water surface displacement
μ	[-]	=	static or dynamic drained friction ratio
ω	[°]	=	angle between the direction of the earthquake induced acceleration and the slope
π	[-]	=	circular constant; $\pi = 3.14$
ρ_g	[kg/m ³]	=	grain density
ρ_s	[kg/m ³]	=	bulk slide density
ρ_w	[kg/m ³]	=	water density
σ'	[kPa]	=	effective normal stress
θ	[°]	=	water body side angle
θ_{rad}	[rad]	=	water body side angle in radians
τ_s	[kPa]	=	downslope acting shear stress

Notation

τ_r	[kPa]	=	downslope acting shear resistance
φ	[°]	=	static or dynamic drained friction angle

Subscripts

b	=	dam crest width; block
c	=	centre of gravity; centroid
d	=	dynamic
F	=	flank
g	=	grain
h	=	horizontal
hs	=	hydrostatic
K	=	crest (German Krone)
m	=	middle; averaged
M, max	=	maximum
n	=	whole number
NK	=	slope change (German Neigungsknick)
red	=	reduced
R	=	reflection
RW	=	still water (German Ruhewasser)
s	=	static; slide
st	=	stable
tot	=	total
tr	=	transition point from shore slope to horizontal overland flow portion
v	=	vertical
w	=	water
1	=	cross-section 1 in Figure 4-2(b)
2	=	cross-section 2 in Figure 4-2(b)

Abbreviations

comp.	=	component
$\cosh(y)$	=	hyperbolic cosine; $\cosh(y) = (e^y + e^{-y})/2$
$\coth(y)$	=	hyperbolic cotangent; $\coth(y) = (e^y + e^{-y})/(e^y - e^{-y})$
hor./Hor.	=	horizontal/Horizontal
p.u.l.	=	per unit length
$\operatorname{sech}(y)$	=	hyperbolic secant

SPH	=	Smoothed Particle Hydrodynamics
$\tanh(y)$	=	hyperbolic tangent
VAW	=	Laboratory of Hydraulics, Hydrology and Glaciology (German Versuchsanstalt für Wasserbau, Hydrologie und Glaziologie)
Ver.	=	vertical
2D	=	two-dimensional (in a wave channel or in a lake having the form of a wave channel)
3D	=	three-dimensional (in a wave basin or in a lake having the form of a wave basin)

Glossary

The following definitions apply to terms used in this manual.

Bore	A non-linear wave type, characterised by a dominant peak with a steep front and gradually-falling back slope (Figure 2-6). Certain impulse waves or broken waves near the shore approximate to this type of wave.
Breaking	Unstable condition of a wave when air is entrained into the crest or the crest collapses forwards. This happens with deep-water waves when the wave steepness H/L , with shallow-water waves when the relative wave height H/h or with intermediate-water waves when both these parameters exceed a given limiting value.
Capillary water wave	A surface wave principally influenced by capillary forces; it has a wave length $L < 1.7$ cm.
Cnoidal wave	A theoretical, non-linear wave type; it includes both linear as well as solitary waves as limiting cases (Figure 2-4). Certain impulse waves approximate to this wave type.
Coupling location	Location between near and far fields to determine the wave parameters in intermediate geometries between 2D and 3D.
Dam break wave	This is the gravity wave which results from the failure of a dam. In model tests such a wave may be simulated by the sudden removal of an impounding wall.
Deep-water wave	A wave which does not mobilise the water column down to the full depth to the bed and is therefore not influenced by this. After the linear wave theory a wave is classified as a deep-water wave if $L/h < 2$. The opposite is a shallow-water wave.
Diffraction	A wave moving towards and past an obstacle gives up some of its energy laterally into the area of the wave shadow (Figure 4-1a).
Edge wave	A wave propagating along the shoreline perpendicular to the slide direction (Figure 4-8).

Far field	Typically, this is several wave lengths from the slide impact zone beyond where the generated impulse wave undergoes no further significant change of shape (except due to friction and frequency dispersion). A constant relationship has established itself between kinetic and potential wave energy. The opposite is the near field.
Freeboard	The distance, measured vertically, between the current still water level of a reservoir and the crest level of the dam.
Frequency dispersion	An impulse wave train typically consists of several waves of different frequencies (periods, lengths). The larger the frequency (period, length) the faster a wave propagates according to Eq. (2.1). As a consequence, the waves within an impulse wave train separate or disperse such that the shape of the impulse wave train changes with distance from the slide impact location.
Froude similitude	The relationship of inertia to gravity forces (Froude number) in the model corresponds to that in the prototype. However, the relation of inertia to surface tension force (Weber number), to friction force (Reynolds number) and to compressibility force (Cauchy number) cannot be satisfied at the same time. This leads to scale effects when the model scale is not 1:1, but these are often negligible.
Generally applicable equation	A generally applicable equation is one that can be applied for any slide or reservoir parameters, provided that the dimensionless limitations are satisfied. Such an equation is developed from the evaluation of the results of tests carried out on the basis of systematic and independent variation of all important governing parameters.
Geometrical similarity	The similar shape of prototype and model, which differ only in their size; this is a basic requirement for the extrapolation of model test results to the prototype.
Granulate properties	Properties related to the granular material of the slide mass; they are indicated with the subscript g (V_g, ρ_g).
Gravity water wave	A water wave that is influenced principally by gravity force.

Impulse product parameter	The parameter $P = FS^{1/2}M^{1/4}\{\cos[(6/7)\alpha]\}^{1/2}$, which contains only governing parameters, with which Heller (2007) and Heller and Hager (2010) describe the prediction of most wave parameters such as the maximum amplitude, height and period, the wave volume as well as the wave amplitude and height decay. The parameter refers to the streamwise slide momentum flux component.
Impulse waves	Individual or groups of waves generated by mass movements into water bodies.
Intermediate-water wave	A wave whose movement is slightly affected by the bed. According to the linear wave theory its relative length is between that of a deep and shallow-water wave ($20 \leq L/h \leq 2$).
Kinetic wave energy	Energy stored in the water particle movement.
Linear wave	Theoretical wave type in the form of a sine curve for which, in addition, $H/h < 0.03$ and $H/L < 0.006$ (Figure 2-1).
Mass movement	A pronounced mass location change at the ground surface; The mass may consist of material such as rock, earth, ice or snow propagating e.g. as slide or fall (Section 4.4).
Model effect	Deviation of results between a hydraulic model and the corresponding prototype due to a non-identical geometry.
Navier-Stokes equations	Differential equations describing the three velocity components, the density and the pressure at any point in a fluid (water). Analytic solutions only exist for simplified cases but, with the required effort, the equations can be completely solved by numerical means (Direct Numerical Simulation).
Near field	Typically extending up to several wave lengths from the slide impact zone, this zone is where large changes in the form of the generated impulse wave take place. The potential wave energy is normally greater than the kinetic energy. A constant relationship of potential to kinetic wave energy has not established itself. The opposite is far field.

Non-periodic wave	An individual wave.
Oscillatory wave	The water particles follow elliptical paths and, over time, stay in the same position. There is transport of energy but not of fluid mass.
Periodic wave	A wave in a group of waves.
Plunging breaker	Form of wave breaking when the crest collapses forward and, for a short time, with the wave front forms an “air tube”, as is often seen on photographs of surfing.
Potential theory	Mathematically idealised description of a fluid as frictionless and irrotational. The streamlines in the fluid are so aligned that they possess a potential field. Many phenomena in hydraulics are analysed using the potential theory, for example water waves, ground water flow or pipeline flow.
Potential wave energy	Energy expended in the displacement of water from its mean position.
Reflection	After striking the shore, a wave moves back with the same (total reflection) or reduced wave height.
Refraction	A wave experiences a change of direction in shallow-water due to the shoaling effect and finally moves mostly frontally towards the shore.
Run-up height	The vertical distance between the still water level and the highest point reached by the wave during run-up.
Scale effect	Deviation of the relative results in hydraulic model testing from those in the prototype as a result of those force ratios (Weber number, Reynolds number, Cauchy number) which cannot be correctly represented in the model.
Shallow-water wave	A wave which mobilises the entire water depth, down to the bed and therefore is influenced by the bed due to the phenomenon of shoaling. According to linear wave theory, $L/h > 20$ for such waves. The opposite is the deep-water wave.
Shoaling	Wave transformation in the vicinity of the shore due to the decrease of the still water depth.

Sine wave	See linear wave.
Slide properties	Properties which relate to the slide mass including the porosity; they are indicated by the subscript s (V_s, ρ_s).
Solitary wave	Theoretical, non-linear wave type consisting only of a wave crest but no wave trough (Figure 2-5). This wave type is used as approximation for certain impulse waves.
Stokes wave	Theoretical, non-linear wave type which is somewhat steeper than a sine wave but has a rather flatter and longer trough (Figure 2-3). This wave type approximates to certain impulse waves.
Total reflection	A wave is reflected by a vertical shore and moves back without any loss of height.
Translatory wave	The water particles move in the direction of movement of the wave and both energy and fluid mass are transported.
Tsunami	From the Japanese “tsu” for harbour and “nami” for wave. Caused by a sudden movement of a large volume of water, as a result of earthquakes (seismic sea waves) but also subaerial or underwater slides, meteorite impacts, volcanic explosions, releases of natural gas etc.
Wave breaking	See breaking.
Wave crest	That part of a wave above the original still water level.
Wave peak	The highest point of a wave.
Wave trough	That part of the wave which is below the original still water level.
Wave type product	The product $S^{1/3}M \cos[(6/7)\alpha]$, composed only of governing parameters, which Heller (2007) and Heller and Hager (2011) use to distinguish the four observed wave types from each other.
2D tests	Two-dimensional: tests carried out in a prismatic wave channel, with the wave parameters measured only in the centre of the channel. The impulse waves propagate longitudinally and may therefore be considered 2D.

3D tests

Three-dimensional: tests carried out in a rectangular wave basin in which the wave parameter measurements can be conducted over the whole water surface area. The impulse waves propagate freely, radiating from the slide impact location, and may therefore be considered 3D.

A Wave overtopping at granular dams

While wave overtopping at rigid structures including vertical walls ($\beta = 90^\circ$) is considered in Subsection 3.3.4, this appendix focuses on the wave overtopping process at granular dams, which is subject to erosion by water overflow. This approach is not included in the computational procedure of Step 1, as the up-scaling of the erosion process from laboratory to prototype dimensions involves high uncertainties. The equations presented below therefore provide only a rough estimation. Nonetheless, the equations of this approach are included in the computational tool (Section 5.5).

The equations for the prediction of the overtopping process at granular dams are taken from Huber *et al.* (2017). The general definition of the predicted values is similar to wave overtopping at rigid dams addressed in Section 3.3.4. However, the eroded crest depth is calculated as an additional target value (Figure A-1).

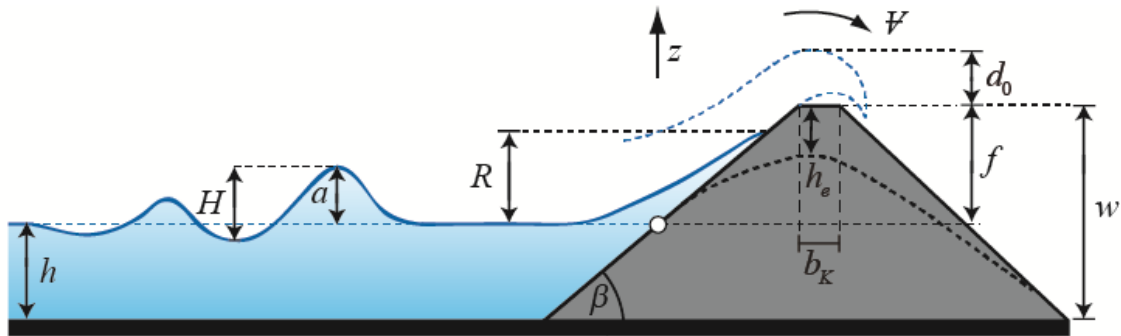


Figure A-1 Sketch defining the parameters for the wave run-up and dam overtopping at a granular dam.

The overtopping volume \mathcal{V} per unit dam crest length is calculated with

$$\mathcal{V} = 1.53\varepsilon \left(\frac{h}{w} \right)^{2.5} \left(\frac{0.1}{\tan \beta} + \frac{b_K}{w} \right)^{-1/9} h^2. \quad (\text{A.1})$$

a [m]	=	Wave crest amplitude (in front of the dam) (Figure A-1)
b_K [m]	=	Dam crest width (Figure A-1)
h [m]	=	Still water depth (in front of the dam)
\mathcal{V} [m ³ /m]	=	Overtopping volume per unit dam crest length
w [m]	=	Dam height (Figure A-1)
β [°]	=	Run-up angle equal to upstream dam face slope (Figure A-1)
ε [-]	=	Relative wave crest amplitude; $\varepsilon = a/h$

The maximum wave overtopping flow depth is determined with

$$d_0 = 1.25\varepsilon \left(\frac{h}{w}\right)^{1.7} \left(\frac{\beta}{90^\circ}\right)^{0.25} w. \quad (\text{A.2})$$

a [m]	=	Wave crest amplitude (in front of the dam) (Figure A-1)
d_0 [m]	=	Maximum wave overtopping flow depth (Figure A-1)
h [m]	=	Still water depth (in front of the dam)
w [m]	=	Dam height (Figure A-1)
β [°]	=	Run-up angle equal to upstream dam face slope (Figure A-1)
ε [-]	=	Relative wave crest amplitude; $\varepsilon = a/h$

The wave overtopping duration is given by

$$t_o = \frac{1}{0.11} \left(\frac{h}{w}\right)^{5/3} \left(\frac{0.1}{\tan \beta} + \frac{b_K}{w}\right)^{0.2} (w/g)^{0.5}. \quad (\text{A.3})$$

a [m]	=	Wave crest amplitude (in front of the dam) (Figure A-1)
b_K [m]	=	Dam crest width (Figure A-1)
g [m/s ²]	=	Gravitational acceleration; $g = 9.81 \text{ m/s}^2$
h [m]	=	Still water depth (in front of the dam)
t_o [s]	=	Wave overtopping duration
w [m]	=	Dam height (Figure A-1)
β [°]	=	Run-up angle equal to upstream dam face slope (Figure A-1)
ε [-]	=	Relative wave crest amplitude; $\varepsilon = a/h$

The average discharge per unit dam crest length q_m is determined from

$$q_m = \mathcal{V}/t_o. \quad (\text{A.4})$$

q_m [m ² /s]	=	Average unit discharge
t_o [s]	=	Duration of overtopping (Eq. A.3)
\mathcal{V} [m ³ /m]	=	Overtopping volume (Eq. A.1)

Similar to overtopping at rigid dams, the maximum discharge may be estimated by $q_{0M} \approx 2q_{0m}$ if the freeboard is small compared to the still water depth, i.e. $f \ll h$.

The eroded crest depth h_e is defined as the vertical distance between the maximum crest elevation before and after wave overtopping (Figure A-1). It is given by

$$h_e = 0.36 \tanh(2.8\varepsilon) \left(\frac{h}{w}\right)^3 \exp\left(-4.9\left(\frac{0.1}{\tan \beta} + \frac{b_K}{w}\right)\right) w. \quad (\text{A.5})$$

a [m]	=	Wave crest amplitude (in front of the dam) (Figure A-1)
b_K [m]	=	Dam crest width (Figure A-1)
h [m]	=	Still water depth (in front of the dam)
h_e [m]	=	Eroded crest depth (Figure A-1)
w [m]	=	Dam height (Figure A-1)
β [°]	=	Run-up angle equal to upstream dam face slope (Figure A-1)
ε [-]	=	Relative wave crest amplitude; $\varepsilon = a/h$

Equations (A.1) to (A.5) were derived from experiments with solitary waves ($a/H = 1$), which are characterised by a large horizontal mass transport (Section 2.2). Therefore, this wave type represents an extreme case. Moreover, the experiments on which the equations are based were conducted with homogeneous model embankment dams composed of non-cohesive sediment grains with diameters between 1.23 and 2.68 mm. Consequently, the experimental setup corresponds to a dam structure without any safety reserves. Dams at prototype scale typically feature impervious cores as well as surface protection including riprap. Particularly, the calculated values of the eroded crest depth h_e (Eq. A.5) should be regarded as a worst-case scenario. Limitations on the use of Eqs. (A.1) to (A.5) are shown in Table A-1.

Table A-1 Limitations to calculate wave overtopping at granular dams.

Term	Range	Term	Range
Relative wave crest amplitude	$0.25 \leq \varepsilon \leq 0.75$	Run-up angle	$18.4^\circ \leq \beta \leq 33.3^\circ$
Wave-freeboard ratio	$0.8 \leq a/f \leq 11.4$	Non-linearity	$a/H = 1.00$
Relative still water depth	$0.70 \leq h/w \leq 0.95$	Relative crest width	$0 \leq b_K/w \leq 0.5$

B Extended bibliography

B.1 Impulse wave generation and propagation

Battaglia, D., Strozzi, T., Bezzi, A. (2015). Landslide hazard: Risk zonation and impact wave analysis for the Bumbuma Dam-Sierra Leone. <i>Geology for Society and Territory-Volume 2</i> :1129-1134, G. Lollino et al. (eds.), Springer, Basel.
Bregoli, F., Bateman, A., Medina, V. (2017). Tsunamis generated by fast granular landslides: 3D experiments and empirical predictors. <i>Journal of Hydraulic Research</i> 55(6):743-758.
Brühl, M., Becker, M. (2018). Analysis of subaerial landslide data using nonlinear Fourier transform based on Korteweg-deVries equation (KdV-NLFT). <i>Journal of Earthquake and Tsunami</i> 12(02):1840002.
Bullard, G.K., Mulligan, R.P., Carreira, A., Take, W.A. (2019). Experimental analysis of tsunamis generated by the impact of landslides with high mobility. <i>Coastal Engineering</i> 152:103538.
Cannata, M., Marzocchi, R., Molinari, M.E. (2012). Modeling of landslide-generated tsunamis with GRASS. <i>Transactions in GIS</i> 16:191-214.
Clous, L., Abadie, S. (2019). Simulation of energy transfers in waves generated by granular slides. <i>Landslides</i> 16(9):1663-1679.
Di Risio, M., Bellotti, G., Panizzo, A., De Girolamo, P. (2009). Three-dimensional experiments on landslide generated waves at a sloping coast. <i>Coastal Engineering</i> 56(5-6):659-671.
Di Risio, M., De Girolamo, P., Beltrami, G.M. (2011). Forecasting landslide generated tsunamis: a review. In <i>The tsunami threat-research and technology</i> . IntechOpen.
Ersoy, H., Karahan, M., Gelisli, K., Akgun, A., Anilan, T., Sunnetci, M.O., Yahsi, B.K. (2019). Modeling of the landslide-induced impulse waves in the Artvin Dam reservoir by empirical approach and 3D numerical simulation. <i>Engineering Geology</i> 249(1):112-128.
Frey, H., Huggel, C., Chisolm, R.E., Baer, P., McArdeell, B., Cochachin, A., Portocarrero, C. (2018). Multi-source glacial lake outburst flood hazard assessment and mapping for Huaraz, Cordillera Blanca, Peru. <i>Frontiers in Earth Science</i> 6:201.
Fuchs, H., Pfister, M., Boes, R., Perzlmaier, S., Reindl, R. (2011). Impulswellen infolge Lawineneinstoss in den Speicher Kühltai. <i>Wasserwirtschaft</i> 101(1-2):54-60 (in German).
Fuchs, H., Heller, V., Hager, W.H. (2010). Impulse wave run-over: experimental benchmark study for numerical modelling. <i>Experiments in Fluids</i> 49(5):985-1004.
Heller, V., Hager, W.H. (2014). A universal parameter to predict subaerial landslide tsunamis? <i>Journal of Marine Science and Engineering</i> 2(2):400-412.
Lalli, F., Postacchini, M., Brocchini, M., (2020). Long waves approaching the coast: Green's law generalization. <i>Journal of Ocean Engineering and Marine Energy</i> (published online).
Lindstrøm, E.K., Pedersen, G.K., Jensen, A., Glimsdal, S. (2014). Experiments on slide generated waves in a 1: 500 scale fjord model. <i>Coastal Engineering</i> 92:12-23.
McFall, B.C., Fritz, H.M. (2016). Physical modelling of tsunamis generated by three-dimensional deformable granular landslides on planar and conical island slopes. <i>Proceedings of the Royal Society A: Mathematical, Physical and Engineering Sciences</i> 472(2188):20160052.
McFall, B. C., Mohammed, F., Fritz, H.M., Liu, Y. (2018). Laboratory experiments on three-dimensional deformable granular landslides on planar and conical slopes. <i>Landslides</i> 15(9):1713-1730.
Meng, Z. (2018). Experimental study on impulse waves generated by a viscoplastic material at laboratory scale. <i>Landslides</i> 15(6):1173-1182.
Meng, Z., Ancey, C. (2019). The effects of slide cohesion on impulse-wave formation. <i>Experiments in Fluids</i> 60(10):151.
Miller, G.S., Take, A.W., Mulligan, R.P., McDougall, S. (2017). Tsunamis generated by long and thin granular landslides in a large flume. <i>Journal of Geophysical Research: Oceans</i> 122(1):653-668.

Mohammed, F., Fritz, H.M. (2012). Physical modeling of tsunamis generated by three-dimensional deformable granular landslides. <i>Journal of Geophysical Research: Oceans</i> 117(C11).
Mulligan, R.P., Take, W.A., Bullard, G.K. (2019). Non-hydrostatic modeling of waves generated by landslides with different mobility. <i>Journal of Marine Science and Engineering</i> 7(8):266.
Mulligan, R.P., Take, W.A. (2017). On the transfer of momentum from a granular landslide to a water wave. <i>Coastal Engineering</i> 125:16-22.
Romano, A., Bellotti, G., Di Risio, M. (2013). Wavenumber–frequency analysis of the landslide-generated tsunamis at a conical island. <i>Coastal Engineering</i> 81:32-43.
Romano, A., Di Risio, M., Bellotti, G., Molfetta, M. G., Damiani, L., De Girolamo, P. (2016). Tsunamis generated by landslides at the coast of conical islands: experimental benchmark dataset for mathematical model validation. <i>Landslides</i> 13(6):1379-1393.
Ruffini, G., Heller, V., Briganti, R. (2020). Numerical characterisation and efficient prediction of landslide-tsunami propagation over a wide range of idealised bathymetries. <i>Coastal Engineering</i> (in preparation).
Sælevik, G., Jensen, A., Pedersen, G. (2009). Experimental investigation of impact generated tsunami; related to a potential rock slide, Western Norway. <i>Coastal Engineering</i> 56(9):897-906.
Synolakis, C.E., Skjelbreia, J.E. (1993). Evolution of maximum amplitude of solitary waves on plane beaches. <i>Journal of Waterway, Port, Coastal, and Ocean Engineering</i> 119(3):323-342.
Take, W.A., Mulligan, R.P., Stevenson, E.P., Miller, G.S. (2018). Physical modelling of landslides into reservoirs: effect of capillarity on rheology of granular landslide at impact. In <i>Landslides and Engineered Slopes. Experience, Theory and Practice</i> (pp. 1889-1896). CRC Press.
Tessema, N.N., Sigtryggsdóttir, F.G., Lia, L., Jabir, A.K. (2019). Case study of dam overtopping from waves generated by landslides impinging perpendicular to a reservoir's longitudinal axis. <i>Journal of Marine Science and Engineering</i> 7(7):221.
Wang, Y., Liu, J., Li, D., Yan, S. (2017). Optimization model for maximum tsunami amplitude generated by riverfront landslides based on laboratory investigations. <i>Ocean Engineering</i> 142:433-440.
Xue, H., Ma, Q., Diao, M., Jiang, L. (2019). Propagation characteristics of subaerial landslide-generated impulse waves. <i>Environmental Fluid Mechanics</i> 19(1):203-230.
Yavari-Ramshe, S., Ataie-Ashtiani, B. (2019). On the effects of landslide deformability and initial submergence on landslide-generated waves. <i>Landslides</i> 16(1):37-53.
Zhang, Y., Li, D., Yin, K., Xiao, L., Fu, X., Glade, T., Leo, C. (2020). Numerical analysis of landslide-generated impulse waves affected by the reservoir geometry. <i>Engineering Geology</i> 266(3):105390.
Zitti, G., Ancey, C., Postacchini, M., Brocchini, M. (2016). Impulse waves generated by snow avalanches: momentum and energy transfer to a water body. <i>Journal of Geophysical Research: Earth Surface</i> 121(12):2399-2423.

B.2 Wave-shore and wave-structure interaction

Dong, G., Wang, G., Ma, X., Ma, Y. (2010). Harbor resonance induced by subaerial landslide-generated impact waves. <i>Ocean Engineering</i> 37(10):927-934.
Ghodoosipour, B., Stolle, J., Nistor, I., Mohammadian, A., Goseberg, N. (2019). Experimental study on extreme hydrodynamic loading on pipelines. Part 1: Flow hydrodynamics. <i>Journal of Marine Science and Engineering</i> 7(8):251.
Ghodoosipour, B., Stolle, J., Nistor, I., Mohammadian, A., Goseberg, N. (2019). Experimental study on extreme hydrodynamic loading on pipelines part 2: Induced force analysis. <i>Journal of Marine Science and Engineering</i> 7(8):262.
Hafsteinsson, H.J., Evers, F.M., Hager, W.H. (2017). Solitary wave run-up: wave breaking and bore propagation. <i>Journal of Hydraulic Research</i> 55(6):787-798.

Istrati, D., Buckle, I., Lomonaco, P., Yim, S. (2018). Deciphering the tsunami wave impact and associated connection forces in open-girder coastal bridges. <i>Journal of Marine Science and Engineering</i> 6(4):148.
Linton, D., Gupta, R., Cox, D., van de Lindt, J., Oshnack, M.E., Clauson, M. (2013). Evaluation of tsunami loads on wood-frame walls at full scale. <i>Journal of Structural Engineering</i> 139(8):1318-1325.
Thusyanathan, N.I., Madabhushi, S.P.G. (2008). Tsunami wave loading on coastal houses: a model approach. <i>Proceedings of ICE</i> 161(2):77-86.
Wüthrich, D., Pfister, M., Nistor, I., Schleiss, A.J. (2018). Experimental study of tsunami-like waves generated with a vertical release technique on dry and wet beds. <i>Journal of Waterway, Port, Coastal, and Ocean Engineering</i> 144(4):04018006.
Wüthrich, D., Pfister, M., Nistor, I., Schleiss, A.J. (2018). Experimental study on the hydrodynamic impact of tsunami-like waves against impervious free-standing buildings. <i>Coastal Engineering Journal</i> 60(2):180-199.
Wüthrich, D., Pfister, M., Nistor, I., Schleiss, A. J. (2018). Experimental study on forces exerted on buildings with openings due to extreme hydrodynamic events. <i>Coastal Engineering</i> 140:72-86.
Zelt, J.A., Raichlen, F. (1991). Overland flow from solitary waves. <i>Journal of Waterway, Port, Coastal, and Ocean Engineering</i> 117(3):247-263.

Addendum: Shallow slide impact angles $15^\circ \leq \alpha \leq 30^\circ$

Frederic M. Evers, Felix Bross

The *impulse wave manual* (Evers *et al.* 2019¹, abbr. *IWM*) allows for the estimation of the most important wave properties related to landslide-generated impulse wave events in reservoirs, e.g. wave amplitudes and run-up heights. The computational procedure presented in the *IWM* is based on generally applicable equations developed from lab model tests. Consequently, the equations' applicability ranges are limited by their underlying experimental parameter ranges (*IWM* Section 3.2.4.1). In case the equations' input parameters exceed these limitations, the results of the computational procedure are subject to additional uncertainties (*IWM* Section 4.7). Especially the lower limitation of the slide impact angle with $\alpha \geq 30^\circ$ (*IWM* Tables 3-2 and 3-3) has been identified as too steep for the assessment of hazard scenarios at prototype scale. To extend the *IWM*'s applicability range, 109 additional hydraulic experiments were conducted in a wave channel, i.e. for the extreme case of confined 2D wave propagation (*IWM* Section 3.2.1), with shallow slide impact angles $\alpha = 15^\circ, 22.5^\circ$ and 30° .

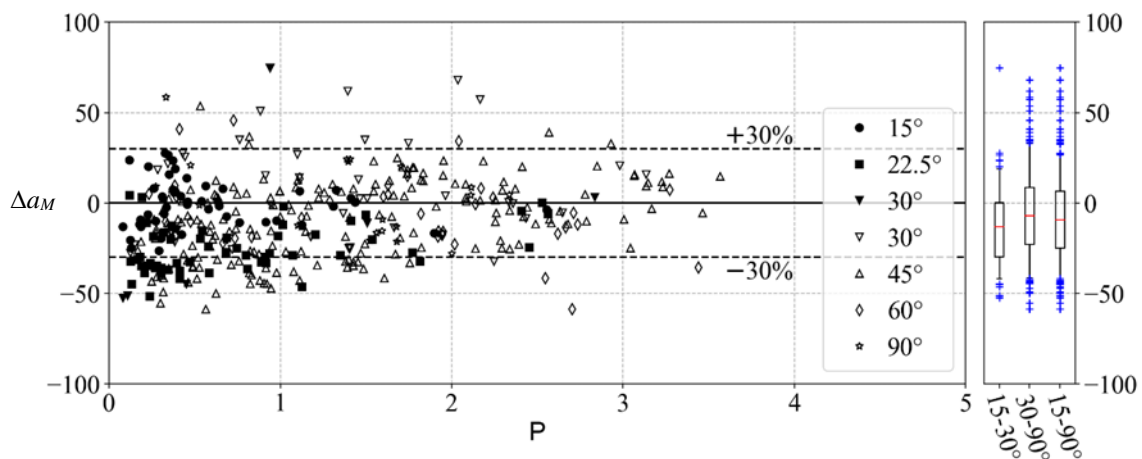


Figure 1 Percentage deviation of the measured from the predicted maximum wave amplitudes Δa_M versus the impulse product parameter P ; $15^\circ \leq \alpha \leq 30^\circ$ (filled markers), $30^\circ \leq \alpha \leq 90^\circ$ (hollow markers); box plot antennas at 5th and 95th percentiles.

Figure 1 shows the percentage deviation of the measured from the predicted maximum wave amplitudes $a_M = (4/5)H_M$ (*IWM* Eqs. 3.13 and 3.16), defined as $\Delta a_M = (a_{M,measured} / a_{M,predicted}) - 1$ [%], versus the impulse product parameter P (*IWM* Eq. 3.12). In addition to the experiments with $15^\circ \leq \alpha \leq 30^\circ$, also 278 selected experiments with $30^\circ \leq \alpha \leq 90^\circ$ from the original data set of the *IWM*'s 2D equations (*IWM* Section 3.2.4.2) are included in Fig. 1 for comparison. The deviations shown in the box plot for $15^\circ \leq \alpha \leq 30^\circ$ are within a similar range as for $30^\circ \leq \alpha \leq 90^\circ$. Figure 2 shows the percentage deviation $\Delta a(x)$ of the measured wave amplitudes from the predicted values

¹ Evers, F.M., Heller, V., Fuchs, H., Hager, W.H., Boes, R.M. (2019). Landslide-generated Impulse Waves in Reservoirs – Basics and Computation. *VAW-Mitteilung* 254 (R. Boes, ed.), ETH Zurich, Zürich. <https://doi.org/10.3929/ethz-b-000413216>

$a(x) = (4/5)H(x)$ (*IWM* Eqs. 3.16 and 3.19) along the relative streamwise distance $X = x/h$ (with the still water depth h). Again, the deviations for $15^\circ \leq \alpha \leq 30^\circ$ are within a similar range as for $30^\circ \leq \alpha \leq 90^\circ$. Since no distinct deviations were observed for shallow slide impact angles $15^\circ \leq \alpha \leq 30^\circ$ compared to $30^\circ \leq \alpha \leq 90^\circ$ (Figures 1 and 2), the limitations for the computation of 2D impulse wave generation and propagation can be extended to $15^\circ \leq \alpha \leq 90^\circ$. Table 1 includes the extended parameter range for α as well as F , M , and P and replaces *IWM* Table 3-2.

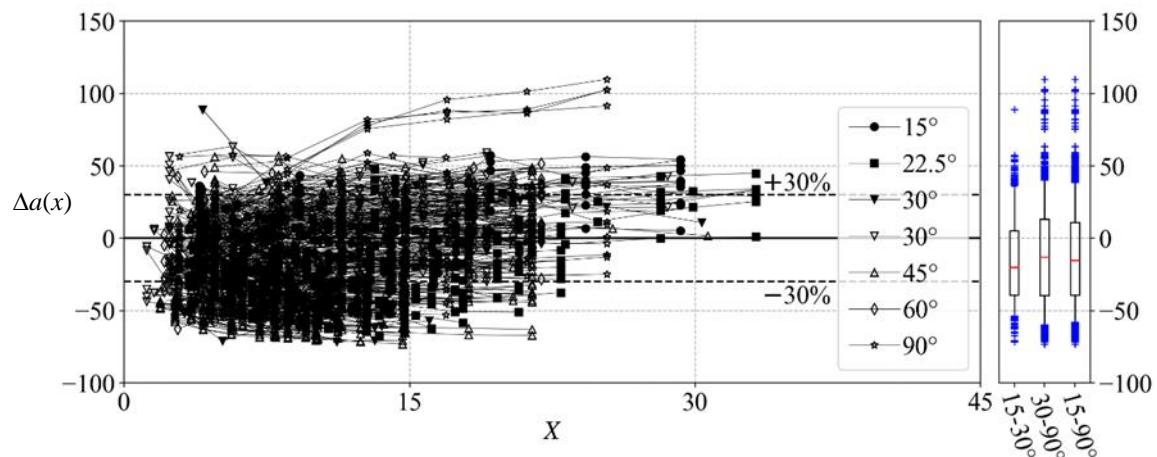


Figure 2 Percentage deviation of the measured from the predicted wave amplitudes $\Delta a(x)$ along the relative streamwise distance X ; $15^\circ \leq \alpha \leq 30^\circ$ (filled markers), $30^\circ \leq \alpha \leq 90^\circ$ (hollow markers); box plot antennas at 5th and 95th percentiles.

Table 1 Extended limitations to compute 2D impulse wave generation and propagation.

Term	Range	Definition
Slide Froude number	$0.47 \leq F \leq 6.83$	$F = V_s/(gh)^{1/2}$
Relative slide thickness	$0.05 \leq S \leq 1.64$	$S = s/h$
Relative slide mass	$0.05 \leq M \leq 10.02$	$M = \rho_s V_s / (\rho_w b h^2)$
Relative slide density	$0.59 \leq D \leq 1.72$	$D = \rho_s / \rho_w$
Relative granulate density	$0.96 \leq \rho_g / \rho_w \leq 2.75$	ρ_g / ρ_w
Relative slide volume	$0.05 \leq V \leq 5.94$	$V = V_s / (b h^2)$
Bulk slide porosity	$30.7\% \leq n \leq 43.3\%$	n
Slide impact angle	$15^\circ \leq \alpha \leq 90^\circ$	α
Relative slide width	$0.74 \leq B \leq 3.33$	$B = b/h$
Relative streamwise distance	$2.7 \leq X \leq 59.2$	$X = x/h$
Impulse product parameter	$0.08 \leq P \leq 8.13$	$P = FS^{1/2}M^{1/4} \{ \cos[(6/7)\alpha] \}^{1/2}$

For the extreme case of 3D impulse wave generation and propagation, no additional hydraulic experiments were conducted with shallow impact angles $\alpha < 30^\circ$. However, similar to the extension to a wider parameter range of the slide density to include snow avalanches based on P (*IWM* Section 3.2.4.3), the *IWM*'s Eqs. (3.22) to (3.35) for 3D impulse wave generation and propagation can also be applied with slide impact angles $15^\circ \leq \alpha \leq 90^\circ$ for a preliminary hazard assessment if $0.13 \leq P \leq 2.08$ (*IWM* Table 3-3). The computational tool has been updated (v1.1) to incorporate the extended ranges for α and is available for download².

² <https://doi.org/10.5281/zenodo.4715565>